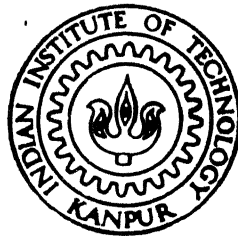


9110972

# LASER ABLATED PLUMES FOR THIN CARBON FILM DEPOSITION

by

RAJESH KUMAR DWIVEDI



DEPARTMENT OF PHYSICS

**INDIAN INSTITUTE OF TECHNOLOGY KANPUR**

MARCH, 1997

# **LASER ABLATED PLUMES FOR THIN CARBON FILM DEPOSITION**

*A Thesis Submitted  
in Partial Fulfilment of the Requirements  
for the Degree of*  
**DOCTOR OF PHILOSOPHY**

*by*  
**Rajesh Kumar Dwivedi**

to the  
**DEPARTMENT OF PHYSICS  
INDIAN INSTITUTE OF TECHNOLOGY**

**March, 1997**

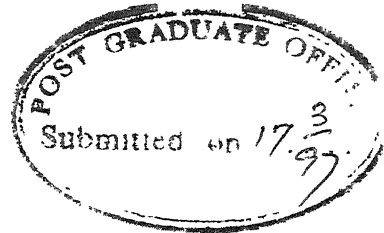
1-7 JUL 1998  
CENTRAL LIBRARY  
I I T, KANPUR  

---

Acc. No. A 125663

PHY-1997-D-DWI-LAS

Entered in system  $\frac{\text{Nishu}}{10-7-98}$



## CERTIFICATE

It is to certify that the work contained in the thesis entitled "*Laser Ablated Plumes for Thin Carbon Film Deposition*" by *Rajesh Kumar Dwivedi* has been carried out under my supervision and the same has not been submitted elsewhere for a degree.

Kanpur

March 17, 1997

*RK Thareja*  
(Raj K. Thareja) 17/3/97

Professor and Head  
Department of Physics  
I. I. T. Kanpur



A125663



## SYNOPSIS

Name of Student : **Rajesh Kumar Dwivedi**

Roll # : **9110972**

Degree for which submitted : **Ph. D.**

Department : **Physics**

Thesis Title : **LASER ABLATED PLUMES FOR THIN CARBON FILM DEPOSITION**

Name of the thesis supervisor : **Professor Raj K. Thareja**

The thesis describes an extensive experimental and theoretical investigation of laser ablated carbon plumes for thin film deposition using Nd:YAG laser wavelengths in an ambient atmosphere and the characterization of the deposited films. The optical emission diagnostics of laser ablated carbon plasma ionic/atomic and molecular species was carried out at low and high laser irradiance in presence of helium and argon gas pressures. The carbon films were deposited under various ambient conditions. The deposited films were characterized and a correlation on the characteristics of deposited films with the plasma plume parameters is presented.

To study the laser ablated carbon plumes, the laser radiation was focused onto a spectroscopic grade pure graphite target mounted in a vacuum chamber which could be evacuated to pressures better than  $10^{-4}$  Torr. The experiments were carried out at various laser wavelengths ( $\lambda=1.064, 0.532, 0.355$  and  $0.266 \mu\text{m}$ ) and helium and argon gas pressures ( $10^{-2}$  - 100 Torr). The plasma radiation was imaged onto the monochromator (HRS-2, Jobin Yvon) so as to have one to one correspondence with the plasma and its image onto the slit of monochromator and output was detected with a photo multiplier tube (Hamamatsu, IP28) and recorded on a strip chart recorder or displayed on a storage oscilloscope (Iwatsu, TS-8123). Ion probe diagnostics of the plasma was carried out using a Langmuir probe. The probe was inserted into one of the port of the vacuum chamber. For thin films deposition the laser radiation was focused using a cylindrical lens. The films were deposited on silicon and glass substrate under various helium and argon gas pressures. The laser ablated carbon "soot" was collected from the chamber at various helium gas pressures to ascertain the presence of fullerenes  $\text{C}_{60}$ .

A hydrodynamic model for pulsed laser deposition of carbon in an ambient atmosphere is presented. The laser ablated plasma is treated as an ideal gas at high pressure

and temperature which initially is confined in small dimension and suddenly allowed to expand in vacuum. The initial stage of plasma expansion in presence of an ambient gas is assumed same as in vacuum and after a mean free path corresponding to the ambient gas, a drag force term which depends on the ambient pressure is introduced. Using hydrodynamic model various plasma parameters viz. plasma temperature, density and velocity are estimated. The plasma dimensions increase with increase in time in all directions with the expansion being larger along the target normal. The expansion velocity in vacuum is seen to first increase with time and ultimately attains constant value at later times. The plasma temperature decreases with increase in time. In the presence of an ambient gas the velocity of the plasma first increases, then becomes constant and finally decreases beyond a certain distance. The distance at which the velocity of the plasma decreases depends on the ambient pressure. The estimated thickness of the film decreases with increase in distance from the target surface normal. |

|The optical emission from the laser ablated carbon plume was recorded at several distances (z) from the target surface at various laser irradiances of 1.064, 0.532, 0.355 and 0.266  $\mu\text{m}$  laser wavelengths. At high laser irradiance ( $\sim 10^9 - 10^{12} \text{ W/cm}^2$ ), various atomic/ionic species from C IV to C I are observed in the optical emission. The intensity of the emitted lines increases in presence of an ambient gas. The electron temperature of the plasma was calculated at various distances from the target surface using emission lines intensity ratio, assuming the plasma to be in local thermodynamic equilibrium (LTE). The electron temperature of the C II transitions  $3p^2P^0 - 4s^2S$  at 392.0 nm decreased with increase in distance from the target surface. In presence of argon gas at 1 Torr the electron temperature was larger than that in vacuum. The Stark broadened profile of C II transition  $3p^2P^0 - 4s^2S$  at 392.0 nm was used to estimate electron density and was found to lie in the range  $10^{16} - 10^{18} \text{ cm}^{-3}$ . The electron density variation with distance from the target surface showed  $z^{-0.24}$  and  $z^{-0.87}$  dependence in vacuum and 1 Torr argon gas respectively. The velocity of the plasma front was estimated from the recorded temporal profiles of C II transition  $3p^2P^0 - 4s^2S$  at 392.0 nm. The plasma expansion velocity was found to be about  $1.2 \times 10^5$  and  $1.95 \times 10^4 \text{ cm/sec}$  in vacuum and 1 Torr argon gas respectively. At low laser irradiance ( $\sim 10^8 - 10^9 \text{ W/cm}^2$ ), molecular carbon ( $\text{C}_2$ ) was found to dominate. An extensive study of  $\text{C}_2$  emission was undertaken to correlate its yield with the deposited

films characteristics. We observed  $C_2$  emission in the  $\Delta v = -2, -1, 0, 1, 2$  sequence of Swan ( $d^3\pi_g - a^3\pi_u$ ) bands and the  $\Delta v = 0$  and 1 sequences of the Deslandres-d' Azambuja ( $C^1\pi_g - A^1\pi_g$ ) bands.  $C_2$  emission studies were performed at various laser irradiances, laser wavelengths (1.064, 0.532, 0.355 and 0.266  $\mu m$ ) and ambient gas pressures in the range of  $10^{-2}$  - 100 Torr. Enhancement of emitted bands was observed in presence of helium and argon gas atmosphere. However, the enhancement was found more in presence of argon than in helium. The  $C_2$  band head intensity is found to be optimum at an intermediate energy for all laser wavelengths. Vibrational temperature of  $C_2$  species was estimated using measured emission intensities of the Swan band heads of the sequence ( $\Delta v = -1$ ) at various laser energies, wavelengths and helium and argon gas pressures. Vibrational temperature decreases with increase in helium gas pressure. In presence of argon gas, the vibrational temperature is found to be maximum at 1 Torr of argon gas pressure and decreased with change of pressure on either side. Vibrational temperature increases with increase in laser wavelength. Vibrational temperature was found to be maximum at some intermediate energy which decreases with decrease in laser wavelengths. The temporal profile of  $C_2$  d-a  $\Delta v = 0$  Swan band at 516.5 nm shows double peak behavior in presence of helium gas pressures beyond a distance of 2 mm from the target surface. The evolution of second slow peak is attributed to shock waves generated in the plasma in presence of helium gas.

/Ion probe diagnostics of laser ablated carbon plumes was also carried out. The space and angle resolved studies of the carbon plasma plume were performed using 0.355  $\mu m$  laser wavelength at various argon pressures ranging from  $10^{-2}$  - 100 Torr./The electron temperature and density were calculated using  $I_p - V_p$  characteristics of the probe at several distances from the target surface, laser irradiances, angle with respect to target surface normal and argon gas pressures. The electron temperature in vacuum decreases with increase in distance from the target surface. At 1 Torr of argon gas pressure the electron temperature was found higher which decreased at larger distances from the target. The electron temperature is maximum along the target surface normal and decreases with increase in angle from the target surface normal. The ion density in vacuum is found to be maximum at  $45^\circ$  from the target surface normal. However, at pressures beyond 1 Torr the ion density of the plasma is maximum along the target surface normal. A cosine function

was fitted to the measured ion densities at various angles. The exponent of the cosine function decreases with increase in distance. The exponent decreased in presence of argon gas pressures and was maximum at 1 Torr as compared to other argon gas pressures. The larger exponent at 1 Torr indicates the forward directed behavior of the plume at that pressure. The ion density increases with increase in laser irradiance and becomes constant at higher irradiance. The velocity of the ions decreases in presence of an ambient gas. It is maximum along the target normal and decreases with increase in angle.

Thin carbon films were deposited on silicon and glass substrates at 10 mm away and parallel to the target surface at  $3.8 \times 10^8 \text{ W/cm}^2$  irradiance of 0.532 and 0.355  $\mu\text{m}$  laser wavelength at various helium and argon gas pressures ( $10^{-2}$  - 100 Torr). The deposited films were characterized using scanning electron microscopy (SEM), x-ray diffraction (XRD), transmission electron microscopy (TEM), selected area electron diffraction (SAED), micro-Raman spectroscopy and resistivity measurements. SEM images of the deposited films in presence of helium gas shows the increasing dominance of micro-crystalline clusters with increase in helium gas pressures. XRD pattern of the carbon film deposited on silicon at 100 Torr helium gas pressure showed peaks at  $10.3^\circ$ ,  $11^\circ$ ,  $17.9^\circ$  and  $21^\circ$  confirming the presence of (100), (002), (110) and (112) crystalline planes of  $\text{C}_{60}$ . The presence of carbon clusters (fullerenes) in laser ablated carbon "soot" in a helium atmosphere ( $10^{-2}$  - 100 Torr) was confirmed by UV-Visible and infra-red spectroscopy. The film deposited in the presence of an argon gas shows the nucleation density to be maximum at 1 Torr and decreases with change of argon gas pressure on either side. XRD pattern of the film deposited shows peaks at  $43.5^\circ$ ,  $76^\circ$ ,  $91.5^\circ$  and  $120^\circ$  indicating the presence of (111), (220), (311) and (400) crystalline planes of cubic diamond. TEM and SAED pattern of the deposited film at 1 Torr shows the ring pattern corresponding to poly-crystalline face centered cubic material. The estimated  $d_{\text{lattice}}$  - spacing, 2.057 and 1.241  $\text{\AA}$ , of the rings matches well with the (111) and (220) planes of cubic diamond respectively. Micro-Raman spectrum of the deposited films at various argon gas pressures shows the presence of two well defined characteristic peaks in the spectrum at  $1580 \text{ cm}^{-1}$  (G-line) and  $1350 \text{ cm}^{-1}$  (D-line). The D-line-to-G-line intensity ratio  $I(\text{D})/I(\text{G})$  decreases with increase in pressure upto 1 Torr but increases with further increase in argon gas pressure. The G-line shifts to  $1550 \text{ cm}^{-1}$  for the film deposited at 1 Torr of argon gas pressure. The resistivity of the deposited

films was measured at various temperatures from  $-190^{\circ}\text{C}$  to  $200^{\circ}\text{C}$ . The resistivity of the deposited film was also maximum at 1 Torr.

/ The characteristics of the deposited films are correlated with various parameters of the plasma plume. It is observed that temperature of the plume is one of the vital parameter that affects the characteristics of the deposited films. At an optimum irradiance of  $3.8 \times 10^8 \text{ W/cm}^2$  the films characteristics are best explained. At this irradiance the molecular  $\text{C}_2$  is a dominant constituent of the plasma plume. In the presence of helium gas the vibrational temperature decreases with increasing pressure indicating that the presence of helium helps in cooling and clustering of the species in plasma giving rise to the increasing dominance of  $\text{C}_{60}$  with increasing pressure. The intensity of  $\text{C}_2$  bands also increases with increase in pressure. However, the increase is more in presence of argon than in helium. The intensity, yield of  $\text{C}_2$  is at a maximum at 1 Torr of argon gas. The vibrational temperature corresponding to 1 Torr is also observed to be maximum. The larger vibrational temperature at 1 Torr is attributed to the fragmentation and ionization of higher clusters in the plume giving rise to the stable  $\text{C}_2$  clusters; with subsequent increase in yield of  $\text{C}_2$ . The increase in  $\text{C}_2$  yield seems to be responsible for the formation of diamond at 1 Torr argon pressure. Ion probe measurements show that the temperature of the plasma at 1 Torr argon gas pressure is nearly constant between 6 and 10 mm distance from the target surface and then decreases with further increases in distance. A practically constant temperature implies the emitted species of nearly constant energy. The location of the substrate in this distance range with respect to target may produce optimum quality films. Further, the electron temperature is larger at 1 Torr of argon gas pressure and also along the target surface normal. The enhanced diamond like character of the deposited films at 1 Torr is attributed to the higher energy of the vaporised plume species. The larger temperature of the plasma increases the probability of transition from graphite to diamond giving DLC. The relatively larger value of the exponent of the cosine function fitted to the measured ion density at various angular positions at 1 Torr argon gas gives the forward directed nature of the deposition process. To sum up, our film deposited at 1 Torr argon gas pressure can well be correlated with the laser ablated plume characteristics.

## ACKNOWLEDGMENTS

Praise be to God Almighty for His persistent grace.

I wish to express my deep sense of gratitude to my thesis supervisor Professor Raj K. Thareja for introducing me to the subject. His able guidance, invaluable suggestions and keen interest through out the course of work helped me a lot in completing this work. My interaction with him academic and otherwise, has always been fruitful and pleasant.

I sincerely thank Professor Y. R. Waghmare and Dr. V. N. Kulkarni for their suggestions from time to time.

A word of thanks also to Dr. (Ms.) Sukarma Thareja for her encouragement during various phases of my work. I express my openhearted thanks to Ashutosh Misra and Satya Prakash Singh for their direct or indirect help in finalising my thesis.

I wish to thank Dr.'s B. Ganguli, Ranjit Singh, P. S. R. Prasad, Amit Sircar and Abhilasha for their valuable help and suggestions in the initial stages of my work. I wish to thank Anoop, Amit, Ashutosh, Anirban, SP and Sushmita for their cooperation. I wish all of them success in their research activities.

I would like to use this opportunity to express my sincere appreciation to Dr. J. Patterson, Principal and Dr. A. N. Dixit, Former Head, Department of Physics, Christ Church College, Kanpur for their constant inspiration. I am also thankful to all my colleagues at Christ Church College, Kanpur especially, Dr. K. N. Sharma, Dr. P. P. Verma, Dr. V. K. Srivastava and Dr. Mukul Misra for their encouragement and support.

It is indeed my great pleasure to express my sincere thanks to my friend Dinesh Deva, for his useful suggestions and cooperation in sorting out many problems.

I would like to thank all the staff members of CELT & Physics office, CELT & Physics workshop, ACMS labs for providing me timely help.

I am also thankful to University Grants Commission (UGC), New Delhi for providing me financial assistance under teacher fellowship programme during last year of my research work.

I am indebted to my wife Sushma, daughter Esha and son Raghav for their patience and understanding. Last but not least, I thank my parents and in laws, for their affectionate understanding and able assistance at difficult moments.

*Rajesh Kumar Dwivedi*

*Dedicated*

*To*

*My Wife Sushma, Daughter Esha and Son Raghav*

## LIST OF PUBLICATIONS

1. Abhilasha, R. K. Dwivedi and R. K. Thareja, "Wavelength Dependence of the Photoablation of Carbon at Low Irradiance", J. Appl. Phys. **75**, 8237 (1994).
2. R. K. Dwivedi and R. K. Thareja, "Optical Emission Diagnostics of C<sub>60</sub> Containing Laser Ablated Plumes for Carbon Film Deposition", Phys. Rev. B **51**, 7160 (1995).
3. R. K. Dwivedi and R. K. Thareja, "Laser Ablated Carbon Plasmas: Emission Spectroscopy and Thin Film Growth", Surf. Coat. Technol. **73**, 170 (1995).
4. R. K. Thareja, Abhilasha and R. K. Dwivedi, "Optical Emission Spectroscopy of Laser Produced Carbon Plasma at Moderate and Low Irradiance in an Ambient Atmosphere", Laser and Particle Beams **13**, 481 (1995).
5. R. K. Thareja and R. K. Dwivedi, "Carbon Thin Films Through Laser Ablation", Phys. Lett. A **222**, 199 (1996).
6. R. K. Thareja, R. K. Dwivedi and Abhilasha, "Role of Ambient Gas on Laser - Ablated Plumes for Thin Carbon Film Deposition", Phys. Rev. B **55**, 2600 (1997).
7. R. K. Dwivedi, S. P. Singh and R. K. Thareja, "Ion Probe Diagnostics of Laser Ablated Plumes for Thin Carbon Films Deposition", J. Appl. Phys., Submitted (1997).



# TABLE OF CONTENTS

	<b>Page</b>
<b>List of Figures</b>	<b>xii</b>
<b>List of Tables</b>	<b>xvi</b>
<b>List of Symbols</b>	<b>xvii</b>
<b>Chapter I</b>	<b>INTRODUCTION</b>
	<b>1</b>
<b>Chapter II</b>	<b>EXPERIMENTAL TECHNIQUES</b>
	<b>13</b>
<b>Chapter III</b>	<b>PHOTOABLATED CARBON PLUMES</b>
	<b>34</b>
<b>Chapter IV</b>	<b>DIAGNOSTICS OF LASER ABLATED PLUMES</b>
	<b>51</b>
	<b>FOR THIN CARBON FILM DEPOSITION</b>
<b>Chapter V</b>	<b>CHARACTERIZATION OF LASER ABLATED</b>
	<b>THIN CARBON FILMS</b>
	<b>99</b>
<b>Chapter VI</b>	<b>CONCLUSIONS</b>
	<b>115</b>
<b>REFERENCES</b>	<b>119</b>

## LIST OF FIGURES

	Page
Fig. 1. Partial potential energy diagram for C <sub>2</sub> Swan bands.	6
Fig. 2. Laser wavelength and irradiance used to produce diamond like carbon films by several investigators. The dashed imaginary line indicates the region of DLC formation.	11
Fig. 3. Typical temporal profile of the Nd:YAG laser (a) 1.06 $\mu\text{m}$ , 8 ns (FWHM) (b) 0.532 $\mu\text{m}$ , 1.8 ns (FWHM).	14
Fig. 4. Prism Harmonic Separator (PHS).	15
Fig. 5. Schematic of the experimental arrangement for the LAD plume optical emission diagnostics.	19
Fig. 6. Schematic of the experimental arrangement for ion probe diagnostics of the plasma plume.	24
Fig. 7. Sketch of the (a) ion probe assembly (b) power supply (c) ion probe circuit.	25
Fig. 8. Typical $I_p - V_p$ characteristics of an ion probe.	26
Fig. 9. Schematic of the experimental arrangement for thin carbon film deposition.	30
Fig. 10. Experimental setup for resistivity measurement of the films.	33
Fig. 11. Schematic diagram showing the different phases present during laser ablation of a target (A) uneffected target (B) evaporated target material (C) dense plasma absorbing laser radiation and (D) expanding plasma outer edge transparent to the laser beam.	40
Fig. 12. Dependence of the plasma dimensions on time in vacuum.	44
Fig. 13. Variation of the velocity of carbon plasma front with time in vacuum.	45
Fig. 14. Variation of plasma temperature as a function of time.	46
Fig. 15. Dependence of the velocity of the plasma on time in presence of argon gas.	49
Fig. 16. Variation of the film thickness with distance from the center of the film.	50
Fig. 17. Emission spectrum of the laser ablated carbon plume at 100 mJ of 0.355 $\mu\text{m}$ laser radiation recorded at a distance of 2 mm from the target surface	53

in vacuum in the wavelength range 320-450 nm.

- Fig. 18. Dependence of the intensity of C II transition at 392.0 nm and C III transition at 388.6 nm on distance from the target surface in vacuum and 1 Torr argon gas pressure using 100 mJ of 0.355  $\mu$ m laser wavelength. 55
- Fig. 19. Variation of the time delay in the peak intensity maxima of C II transition ( $3p^2P^0 - 4s^2S$ ) at 392.0 nm with distance from the target surface at 100 mJ of 0.355  $\mu$ m laser radiation in vacuum and 1 Torr argon. 57
- Fig. 20. Typical plot of  $\ln [(I_s'' \lambda'' g' A' / I_s' \lambda' g'' A'')] versus E' - E''$  for C II species at 2 mm distance from the target surface in vacuum. 58
- Fig. 21. Variation of electron temperature with distance from the target surface using 100 mJ laser energy of 0.355  $\mu$ m radiation in vacuum and 1 Torr argon. 59
- Fig. 22. Typical Stark broadened profile of C II transition  $3p^2P^0 - 4s^2S$  at 392.0 nm in vacuum at a distance of 10 mm using 100 mJ of 0.355  $\mu$ m laser wavelength. 60
- Fig. 23. Variation of electron density of C II transition  $3p^2P^0 - 4s^2S$  at 392.0 nm as a function of distance from the target in vacuum and 1 Torr argon. 61
- Fig. 24. Emission spectrum of the carbon plasma in vacuum at  $3.6 \times 10^8$  W/cm<sup>2</sup> of 1.06  $\mu$ m laser radiation ;
- (a) Spectrum range 415 - 520 nm 62
- (b) Spectrum range 520 - 620 nm. 63
- Fig. 25. C<sub>2</sub> d-a Swan band sequence  $\Delta v = -1$  at  $10^{-3}$  Torr of argon gas pressure at (a) 22 mJ, (b) 33 mJ, (c) 44 mJ and (d) 66 mJ of laser energy. 65
- Fig. 26. C<sub>2</sub> d-a Swan band sequence  $\Delta v = -1$  at  $10^{-1}$  Torr of argon gas pressure at (a) 22 mJ, (b) 33 mJ, (c) 44 mJ and (d) 66 mJ of laser energy. 66
- Fig. 27. Intensity of C<sub>2</sub> Swan band heads (0-1) at 563.5 nm and (1-2) at 558.5 nm at various laser energies of 0.532 and 0.355  $\mu$ m laser wavelength at  $10^{-1}$  Torr argon gas pressure. 67
- Fig. 28. C<sub>2</sub> d-a Swan band sequence  $\Delta v = -1$  at argon gas pressures of (a)  $10^{-1}$  (b) 1 and (c) 100 Torr using 1.06  $\mu$ m laser wavelength. 69

Fig. 29.	Variation in intensity of Swan band head (0-1) at 563.5 nm as a function of argon gas pressure for 1.06, 0.532 and 0.355 $\mu\text{m}$ laser wavelength.	70
Fig. 30.	$\text{C}_2$ d-a Swan band sequence at 10 Torr of (a) argon and (b) helium gas for 355 nm at 45 mJ of laser energy.	71
Fig. 31.	Intensity of $\text{C}_2$ Swan band heads, (0-1) at 563.5 nm and (1-2) at 558.5 nm for 0.355 $\mu\text{m}$ laser wavelength at various helium and argon gas pressures.	72
Fig. 32.	Relative population of the upper vibrational level of the $\text{C}_2$ Swan band sequence $\Delta v = -1$ versus vibrational quantum number for 1 Torr argon gas pressure at 45 mJ energy of 0.355 $\mu\text{m}$ laser wavelength.	74
Fig. 33.	Variation of vibrational temperature with energy for 0.532 and 0.355 $\mu\text{m}$ laser wavelengths at $10^{-1}$ Torr argon gas pressure.	75
Fig. 34.	Variation of vibrational temperature at various pressures of helium gas for 1.06 $\mu\text{m}$ at 60 mJ, 0.532 $\mu\text{m}$ at 40 mJ, 0.355 $\mu\text{m}$ and 0.266 $\mu\text{m}$ at 30 mJ laser energy.	76
Fig. 35.	Vibrational temperature as a function of Ar gas pressures for 1.06 $\mu\text{m}$ at 32 mJ, 0.532 $\mu\text{m}$ and 0.355 $\mu\text{m}$ at 45 mJ laser energy.	78
Fig. 36.	Temporal profiles of $\text{C}_2$ band head at 516.5 nm at $10^{-2}$ Torr helium gas pressure for 60 mJ energy of 1.06 $\mu\text{m}$ laser wavelength.	79
Fig. 37.	Time delay for the appearance of second peak of $\text{C}_2$ d-a $\Delta v = 0$ Swan band with helium gas pressure.	80
Fig. 38.	Dependence of time delay with distance from the target surface.	82
Fig. 39.	Typical ion probe signal at (a) +20 V (b) -20 V for the probe target distance of 10 mm along the target surface normal at 1 Torr argon.	83
Fig. 40.	Plot of square of ion current and probe voltage in vacuum at a distance of 10 and 16 mm along the target normal.	85
Fig. 41.	Dependence of ion density on distance along the target normal for	
	(a) first peak	86
	(b) second peak.	87
Fig. 42.	Variation of the electron temperature with distance along the target surface normal.	88

Fig. 43.	Dependence of electron temperature with argon gas pressure at various angular positions with respect to target surface normal.	89
Fig. 44.	Variation of ion density as a function of argon gas pressure.	90
Fig. 45.	Dependence of ion density on the laser irradiance at 10 mm distance along the target surface normal at 1 Torr argon gas pressure.	92
Fig. 46.	Dependence of ion density on angle at various argon gas pressures.	93
Fig. 47.	Ion density angular profiles at 6, 10 and 14 mm along the target surface normal at 1 Torr of argon gas pressure.	94
Fig. 48.	Variation of the power of the fitted cosine-function with argon gas pressure.	95
Fig. 49.	Delay as a function of angle from the TSN. The dashed line is a guide to eye.	97
Fig. 50.	SEM micrographs of laser ablated carbon films at (a) $10^{-1}$ , (b) 1 and (c) 10 Torr (d) single microcrystal at 1 Torr of Ar gas pressures.	101
Fig. 51.	(a) TEM micrograph and (b) SAED pattern of the film deposited at 1 Torr argon using $3.8 \times 10^8 \text{ W/cm}^2$ irradiance of $0.355 \text{ }\mu\text{m}$ laser wavelength.	103
Fig. 52.	X-ray diffraction pattern of the carbon film deposited at 1 Torr argon gas pressure at $3.8 \times 10^8 \text{ W/cm}^2$ irradiance of $0.355 \text{ }\mu\text{m}$ laser wavelength. Peaks at $43.5^\circ$ , $76^\circ$ , $91.5^\circ$ and $120^\circ$ show the presence of (111), (220), (311) and (400) crystalline planes of cubic diamond.	104
Fig. 53.	Optical absorption spectrum in the range 200 - 500 nm.	105
Fig. 54.	Infrared spectra of carbon clusters extracted from benzene solvable soot collected at (a) $10^{-2}$ , (b) 1 and (c) 100 Torr helium pressure.	107
Fig. 55.	Micro Raman spectra for carbon films at various argon gas pressures.	108
Fig. 56.	Intensity ratio $I(D)/I(G)$ vs argon gas pressure for carbon films. The dotted line is only a guide to the eye.	110
Fig. 57.	Temperature dependence of the resistivity of films deposited at various argon gas pressures.	111

## LIST OF TABLES

	Page
1. Various techniques used for LAD plume diagnostics.	17
2. Different methods used for thin films characterization.	29

## LIST OF SYMBOLS

$\gamma$	Adiabatic exponent
$P_o$	Ambient gas pressure
$V_P$	Applied probe voltage
$A_P$	Area of the ion probe
$I_{em}^{v/v//}$	Band head intensity
$k_B$	Boltzmann constant
$D_v$	Correction factor
$n_c$	Critical density
$\rho_s$	Density of the solid target
$z$	Distance along the target surface normal
$e$	Electron charge
$n_e$	Electron density
$W$	Electron impact parameter
$I_{eo}$	Electron saturation current
$T_e$	Electron temperature
$E''$	Excitation energy of the lower level
$E'$	Excitation energy of the upper level
$p$	Exponent of the fitted cosine function
$\varepsilon$	Fraction of the laser energy absorbed
$F_{\checkmark}^{\checkmark//}$	Franck Condon factor
$\nu$	Frequency
$I_L$	Intensity of laser radiation
$V_o$	Initial volume of the plume
$A$	Ion broadening parameter
$\bar{Z}$	Ion charge
$n_i$	Ion density

$I_{+0}$	Ion saturation current
$T_0$	Isothermal temperature of the plasma
$E_p$	Laser pulse energy
$\tau_L$	Laser pulse duration
$L_s$	Latent heat of sublimation
$v^{//}$	Lower vibrational level
$N_D$	Number of particles in Debye sphere
$\alpha$	Optical absorption coefficient
$h$	Planck's constant
$n$	Plasma density
$\omega_p$	Plasma frequency
$L_p$	Plume length
$\xi$	Radii of the spherical shock front
$R$	Reflectivity
$N_{v'}$	Relative population in vibrational level $v'$
$\rho$	Resistivity
$\beta$	Slowing coefficient
$g^{//}$	Statistical weight of the lower level
$g'$	Statistical weight of the upper level
$d_{\text{lattice}}$	Spacing between the lattice planes
$C_p$	Specific heat at constant pressure
$C_v$	Specific heat at constant volume
$r$	Sum of the radii of the colliding species
$\Delta T$	Temperature rise
$G(v')$	Term value of the upper vibrational level
$L_{\text{th}}$	Thermal diffusion length
$D$	Thermal diffusivity
$\Delta x_t$	Thickness of the evaporated material
$I_p$	Total probe current



$A''$	Transition probability of the lower level
$A'$	Transition probability of the upper level
$v'$	Upper vibrational level
$c$	Velocity of light
$v$	Velocity of the plasma front
$T_{\text{vib}}$	Vibrational temperature
$\Delta H$	Volume latent heat
$\lambda$	Wavelength

# CHAPTER I

## INTRODUCTION

Last several years have seen a phenomenal growth of a large number of thin film deposition processes. Various thin film deposition techniques which have been reported include evaporation,<sup>1,2</sup> sputtering,<sup>3,4</sup> ion beam deposition,<sup>5-7</sup> e-beam deposition,<sup>8</sup> plasma enhanced chemical vapor deposition,<sup>9,10</sup> laser induced chemical vapor deposition,<sup>11</sup> molecular beam epitaxy<sup>12</sup> and laser ablation deposition<sup>13</sup> etc. Of all these available deposition techniques, laser ablation deposition (LAD) technique is rapidly proving to be an effective method for the preparation of a variety of thin films due to its several potential advantages over other conventional deposition techniques. Since its introduction in 1965 by Smith and Turner,<sup>14</sup> it has been used to deposit a variety of materials including metals, semiconductors, superconductors and insulators etc.<sup>13</sup> The success of LAD in fabricating high quality high  $T_c$  superconducting thin films has tremendously enhanced the interest in the research and development in this area. Laser ablation deposition offers the following several advantages over the other conventional physical vapor deposition techniques:

1. It can be used to deposit the thin films of almost any material, irrespective of its optical properties,<sup>15</sup> because under high power laser radiation most of the materials turn optically opaque by an optical breakdown.
2. Compositional fidelity is often achieved between the target material and the deposited film which makes it attractive for fabricating stoichiometric multicomponent films.<sup>16,17</sup>
3. It offers very high instantaneous growth rate. Growth rate of pulsed laser deposited CuNi films as high as 800 nm/sec have been reported which is substantially higher than the growth rate of 10 nm/sec obtained during sputter deposition.<sup>18</sup>
4. Deposition can be carried out even at relatively lower temperatures due to very high kinetic energies of the plasma species.<sup>19</sup>
5. The process is relatively simple, inexpensive and free of contamination.
6. Possible to obtain high density films with good adhesion due to the presence of energetic species during the deposition process.

There are, however, certain drawbacks associated with LAD.<sup>20,21</sup> Foremost of these are the formation of particulates,<sup>20</sup> inhomogeneities of deposition rates resulting from Cos<sup>p</sup>

profile of the ablation plume, relatively small area deposition etc. These problems arise not only from the material specific properties but from the incomplete understanding of the control parameters. Although the results available on LAD seems to be exciting and the application of LAD is ahead of its comprehension, thus for many results have been obtained by trial and error approach. The laser ablation deposition process is very complex in nature. In practice the formation of good quality films is rather difficult as it requires the optimization of various processing variables such as laser irradiance, laser wavelength, laser pulse width, ambient pressure, target-substrate separation and substrate temperature simultaneously. It is therefore, necessary to understand the mechanism of laser-surface interaction both experimentally and theoretically in order to produce the high quality films using pulsed laser deposition.

In laser ablation deposition process, an intense laser beam vaporizes a solid target surface and a thin film is deposited onto a suitably placed substrate. The laser heating of the target surface plays a major role in the particle generation. The peak power density on the target reaches very high so that the process involved in laser ablation is quite different from that in ordinary vacuum evaporation where the thermal equilibrium is maintained. The non-equilibrium nature makes laser ablation technique a unique for thin film deposition. In general, LAD consists of various consecutive processes separated in space and time such as energy coupling to the target material, removal of the material from the target surface, transfer of the target material as vapor and/or plasma to the substrate via gas phase and the subsequent growth of thin film. Each of these processes plays a dominant role in defining the quality of the deposited films, the major role being of laser produced plasma.<sup>22</sup>

Laser-solid interaction depends strongly on laser and interaction parameters (laser wavelength, laser irradiance, pulse waveform, irradiated spot size, angle of incidence etc.), material characteristics (composition, optical and thermal properties etc.) and environmental conditions (pressure, acceleration etc.).<sup>15,23-25</sup> Depending on laser power and pulse duration the laser created plumes consist of atoms, ions in the highly excited states or clusters. The characteristic features of the laser ablated plumes such as temperature, density, velocity, pressure and forward directed nature mainly depend on laser irradiance<sup>25</sup> and surrounding ambient conditions. Laser induced plasma at low laser irradiance  $\sim 10^8 - 10^9 \text{ W/cm}^2$  is mostly used for pulsed laser deposition of thin films e.g. diamond like carbon,<sup>26,27</sup> high  $T_c$  superconductors,<sup>28,29</sup> metallic films,<sup>30-32</sup> polymeric films,<sup>33,34</sup> microelectronics and

optoelectronics,<sup>35</sup> for production of clusters e.g. carbon,<sup>36</sup> sodium,<sup>37</sup> aluminum<sup>38</sup> and copper,<sup>39</sup> nanostructures<sup>40</sup> and for surface temperature measurements.<sup>41</sup> The recent applications of laser ablated plasma at high laser irradiances  $10^9 - 10^{12} \text{ W/cm}^2$  include as a source of x-rays,<sup>42</sup> VUV continuum<sup>43</sup> and highly charged ions,<sup>44-46</sup> for the generation of laser oscillations,<sup>47,48</sup> hydrodynamic studies of plasma,<sup>49,50</sup> modeling of various processes in space physics<sup>51</sup> and studying laser-plasma interaction in presence of an ambient gas.<sup>52-60</sup>

The laser produced plasmas from different targets have been extensively studied.<sup>61</sup> The temporal and space resolved studies of various ionic species of carbon generated from a polythene film using a pulsed ruby laser have been reported by Boland et al.<sup>45</sup> Mann and Rohr<sup>62</sup> have investigated the angular variation of the kinetic energy of various ionic species of carbon. Angle resolved velocity distribution of neutral copper atoms created by UV laser ablation of polycrystalline copper foils have been reported as a function of laser fluence.<sup>63</sup> Recently a planar laser induced fluorescence has been developed by Zerkley and Sappey<sup>64</sup> to determine the ground state atomic density in laser produced plasmas in ambient atmosphere. Intensities of both emission<sup>65,66</sup> and absorption lines<sup>67,68</sup> have been extensively used to quantitatively monitor the spatial variation of ions and neutrals within the plume. The line shapes of the emission lines are very sensitive to local plasma conditions such as temperature, pressure and electron density and hence are being used to study the plasma parameters.<sup>68,69</sup> Use of Stark broadened profiles of selected transitions to estimate electron density has been reported.<sup>67,69-72</sup> The role of several interaction processes such as collisional interaction, recombination, charge exchange and micro-instabilities etc. in line emission enhancement and understanding the hydrodynamics of the expanding plasma have been studied extensively.<sup>73-77</sup> Fast photography and ICCD imaging technique has been applied to investigate the dynamics of the laser ablated species in ambient gas.<sup>77-81</sup> Ion probes are extremely useful diagnostics for the flowing laser plasmas such as those used in LAD.<sup>77,82-85</sup> Ion probes, being flux sensitive, record only the flux of ions reaching the probe and are therefore very useful in the presence of background gas. Experimentally measured values of various parameters are essential input for comprehensive computer modeling of pulsed laser deposition plasmas.<sup>86</sup> There are reports on the study of the interactions of a hot expanding laser plasma with a low density background gas.<sup>78,87,88</sup> The influence of magnetic field on the laser generated plumes is also being studied.<sup>88-92</sup> The significant changes in the laser ablated plume have been investigated at various magnetic field strength.<sup>91,92</sup>

Despite the variety of applications of laser created plasmas, the exact nature of the plasma process is not very well understood. The direction of the laser ablated plume and its angular spread depends on various laser parameters, target parameters and ambient atmosphere.<sup>93</sup> Studies<sup>94,95</sup> have shown that the angular distribution of the laser generated plume is strongly forward peaked and is always oriented along the target surface normal for normal angles of laser incidence. However, there are reports on the tilting of the plume towards the direction of the incident beam for non normal angles of laser incidence.<sup>96</sup> The effect of laser pulse width, laser wavelength and laser fluence on the angular distribution of the depositing plasma species onto a substrate has also been reported.<sup>97</sup> The knowledge of the spatial and angular distribution of the plasma species can provide a better understanding of the LAD process.<sup>98</sup>

The increasing number of studies on laser ablation at low/moderate ( $10^8$  - $10^9$  W/cm<sup>2</sup>) regime and its application to laser ablation deposition in thin film production has led to considerable progress in understanding the laser ablation of carbon. In particular, carbon based materials have attracted a great interest from the scientific community because of the variety of electronic and structural properties exhibited by its allotropic forms. Moreover, thin carbon films show interesting characteristic from the technological point of view and efforts are concentrated on the understanding of the mechanism of structural changes in carbon thin films depending on preparation conditions. The growth of hydrogen free diamond like carbon (DLC) from laser ablation has attracted much interest due to the fact that these films possess properties close to or similar to diamond. These properties include transparency in the infrared (IR), high micro hardness, high electrical resistivity, high wear resistance, low friction coefficient as well as excellent chemical inertness. A variety of applications of DLC films are anticipated in microelectronics, optics and tribology industry. In general, DLC films are characterized by two structures hydrogen-free amorphous carbon (a-C) or hydrogenated amorphous carbon (a-C:H) with domination of tetrahedral bonding. In amorphous DLC, there are some graphite-like  $sp^2$  bonds together with diamond-like  $sp^3$  bonds.<sup>99</sup> The ratio  $sp^3$  / $sp^2$  determines film properties which can vary over a broad range depending on preparation conditions. Presently DLC films are being deposited using variety of laser ablated materials such as polycarbonates, PMMA and frozen acetylene targets.<sup>82,100,101</sup> Various diagnostic techniques for characterizing DLC films have been reviewed by several investigators.<sup>102,103</sup> Generally, the morphologies of the DLC films have

been determined using optical microscopy, electron microscopy methods including scanning electron microscopy (SEM), transmission electron microscopy (TEM) and probe scanning microscopic technique of scanning tunneling microscopy (STM). Recently the atomic force microscopy (AFM) imaging<sup>104</sup> has been used to study the surface morphology of the laser deposited DLC films. The observation of diamond crystallites in the thin films prepared by laser ablation of fullerenes has been studied using micro-Raman, x-ray diffraction and electron energy loss spectroscopy (EELS).<sup>105</sup>

The studies on laser produced carbon plumes at low irradiance ( $\sim 10^8$  -  $10^9$  W/cm<sup>2</sup>) have shown dominance of molecular C<sub>2</sub> species in the plume. However, the irradiance greater than  $10^9$  W/cm<sup>2</sup> yields atoms, ions and higher clusters. Most of the reports<sup>106-110</sup> in the literature on the formation of high quality diamond like films are available only above a critical threshold irradiances  $\sim 10^8$  W/cm<sup>2</sup> and in the range  $10^8$  -  $10^9$  W/cm<sup>2</sup> where molecular C<sub>2</sub> is a most dominant specy.<sup>111-114</sup> It has been widely claimed that the C<sub>2</sub> specy plays a major role in the formation of diamond.<sup>115,116</sup> The laser ablation of diamond films has also shown that C<sub>2</sub> is the dominant desorbed species.<sup>116,117</sup> C<sub>2</sub> molecule possesses seven known triplet and six known electronic states giving rise to nine band systems which lie across the vacuum ultraviolet, visible and infrared spectral regions.<sup>118</sup> The Swan system is the strongest and most easily excited system lying between 420 and 770 nm.<sup>119</sup> In a recent systematization of the energy level scheme and nomenclature for the C<sub>2</sub> molecule, Herzberg et al<sup>118</sup> assigned the notation ( $d^3\pi_g$  -  $d^3\pi_u$ ) for the Swan system. Figure 1 shows the energy level diagram of C<sub>2</sub> Swan bands. Chen et al<sup>114</sup> have studied the optical emission of C<sub>2</sub> bands in Ar+H<sub>2</sub> ambient mixture while depositing the films. Laser induced fluorescence (LIF) and Langmuir probe characterization of the laser vaporized carbon plasmas for deposition of DLC have shown that the yield of C<sub>2</sub> and the kinetic energy of the species being deposited essentially defines the diamond like character in the film.<sup>120</sup> Therefore, the estimate of the temperature and yield of dominating species C<sub>2</sub> may help in understanding the deposited films. Several investigators have estimated the rotational and vibrational temperatures using C<sub>2</sub> Swan band emission.<sup>121,122</sup> The studies on C<sub>2</sub> and CN emission from laser ablated polymers have also been performed.<sup>123</sup> Molecular copper emission from laser ablated plasma at low irradiance is also reported.<sup>124</sup> Carbon molecules are particularly very interesting due to their unique and fascinating structural and spectroscopic properties and their importance in astrophysical processes.

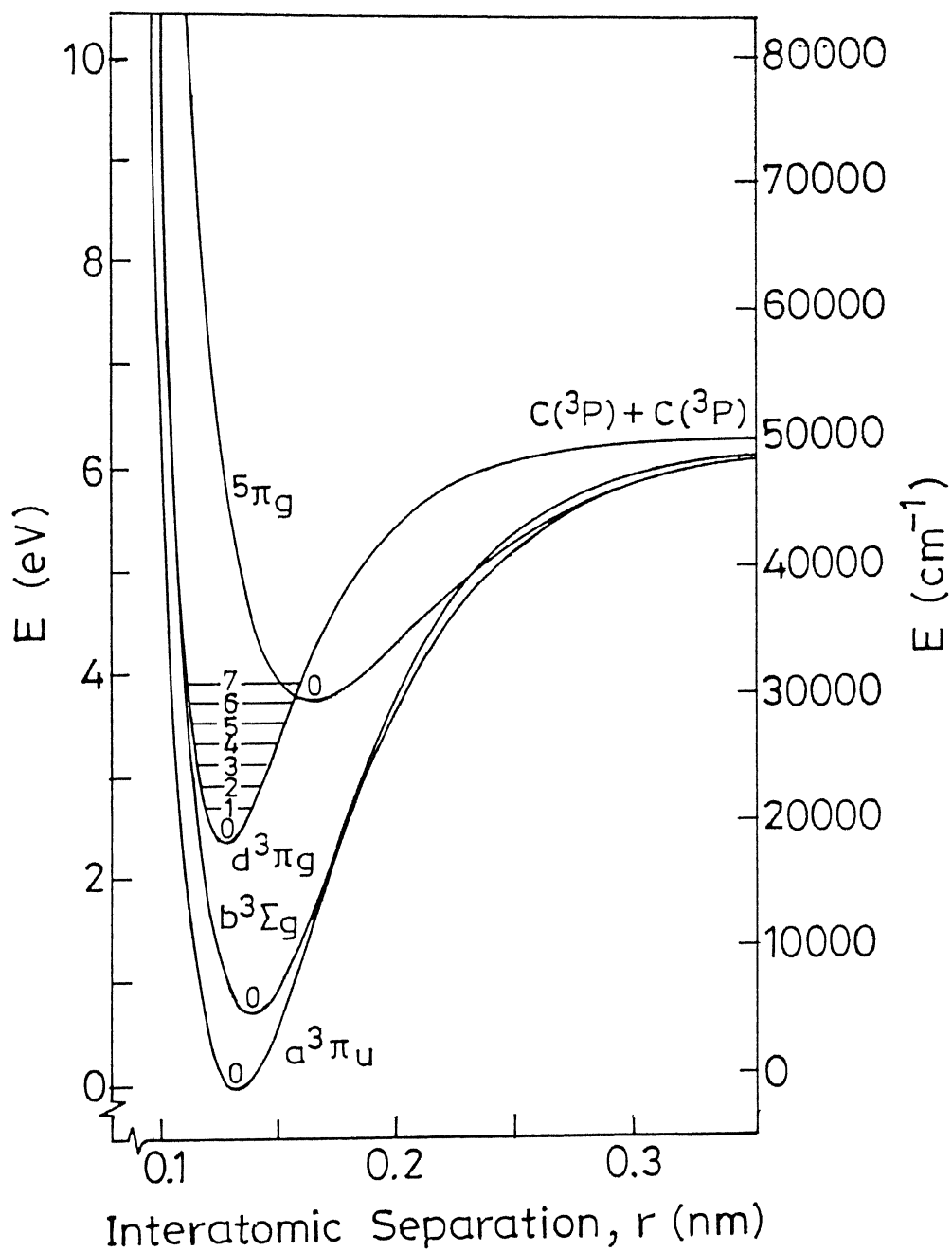


Fig. 1. Partial potential energy diagram for  $C_2$  Swan bands.

The study of carbon clusters (fullerenes) has attracted attention since Kroto et al<sup>125</sup> discovered them in 1985 and Kratschmer et al<sup>126</sup> succeeded in synthesizing it in 1990. The discovery of conductivity in alkali metal doped C<sub>60</sub> (and C<sub>70</sub>) and superconductivity in C<sub>60</sub> doped with K (T<sub>c</sub> = 18 K), Rb (T<sub>c</sub> = 28 K), and their alloys has added further excitement in C<sub>60</sub> thin films.<sup>127</sup> The fabrication of C<sub>60</sub> thin films attracts attention not only because of their basic properties but also for their possible application to electronic devices such as solar cells.<sup>128</sup> Creasy and Brenna<sup>129</sup> have observed fullerene ions from laser ablation of DLC films demonstrating that C<sub>60</sub> ions can be formed in a variety of systems. Prasad et al<sup>130</sup> reported the presence of C<sub>60</sub>, C<sub>70</sub> and C<sub>84</sub> fullerenes in the carbon soot from laser ablated carbon in vacuum. C<sub>60</sub> thin films on various substrates using laser ablation of carbon in argon and helium atmosphere has also been reported.<sup>131,132</sup> Pure fullerenes are presently being studied as precursors for nucleation of diamond thin films.<sup>133</sup> The formation of C<sub>60</sub> from sintered SiC solid using pulsed KrF excimer (248 nm) laser ablation has been demonstrated.<sup>134</sup> The relative abundance of these and smaller clusters in a laser produced plasma depends on various experimental parameters such as laser wavelength, laser intensity and background gas etc. However, the dynamics of formation of carbon clusters in particular C<sub>60</sub> and C<sub>70</sub> is still not well understood. Carbon clusters play important role in the chemistry of cometary and stellar atmospheres.<sup>135</sup> Various investigators<sup>136,137</sup> have observed the physical and chemical properties of the even numbered carbon clusters. Their unique properties lead to the hypothesis that these clusters possess closed spherical structures.<sup>125</sup> C<sub>60</sub>, the third major form of pure carbon is shown to have most symmetrical structure as a truncated icosahedral with 12 pentagons and 20 hexagons. A comprehensive review of higher carbon clusters has been given by Diederich et al.<sup>138</sup> The structural and chemical properties of pure C<sub>60</sub> and C<sub>70</sub> has been determined using nuclear magnetic resonance and x-ray diffraction methods.<sup>126</sup> Raman scattering and energy-dispersive x-ray spectroscopy has also been used to study the transformation induced in C<sub>60</sub> single crystals and thin films by laser irradiation under different chemical environments.<sup>139</sup> Recently the mechanical and elastic properties of C<sub>60</sub> and C<sub>70</sub> films have been determined using broad band surface acoustic wave spectroscopy.<sup>140</sup> To understand the formation of stable fullerenes, a ring-stacking model has been proposed by Wakabayashi and Achiba.<sup>141</sup> They assumed that a carbon cage is formed by sequential stacking with appropriate numbers and combinations of only even-numbered carbon rings without any loss of carbon atoms. They showed that C<sub>2</sub> is a necessary and dominant



molecule for the formation and closed caging of fullerenes. Recently Gruen et al<sup>115</sup> reported obtaining  $C_2^+$  and  $C_2$  species by fragmentation of  $C_{60}$  in a microwave discharge in a 1 Torr argon atmosphere. Weiske et al<sup>142,143</sup> have reported the fragmentation of  $C_{60}^+$  and  $C_{70}^+$  to  $C_n$  ( $n=2, 4, 6, 8$ ) on collision with  $H_2$ ,  $D_2$  and Ar. The knowledge of the nature of the fragmentation process of fullerenes is helpful in understanding the deposited films.

The films with complex composition using laser ablation deposition are being grown in an ambient atmosphere. Laser ablated carbon plasma in the presence of an ambient gas has been used for the deposition of  $C_{60}$  on various substrates.<sup>131</sup> The deposition of high purity TiN films on a cold silicon substrate from a multipulse excimer laser irradiated titanium target at a low pressure ambient  $N_2$  gas has been reported.<sup>19</sup> Pulsed laser deposition of  $YBa_2Cu_3O_{7-x}$  in a diluted  $O_2$  /Ar atmosphere has been shown to produce superior particulate free films.<sup>144</sup> A strong correlation between the ambient pressure and target-substrate distance has been derived for the optimum deposition of superconducting thin films.<sup>145</sup> Recently the surface roughness of the laser deposited  $SrTiO_3$  films has been shown to increase with increase in ambient pressure.<sup>146</sup> It is shown that the presence of the background helium gas enhances the formation of carbon clusters. Epitaxial semiconductor alloys and superlattices with continuously variable composition have been fabricated by LAD in a low pressure background gas.<sup>147</sup> The physics and chemistry of the gas phase greatly influences the transfer of the target material and the film deposition by interaction with the gaseous particles. Recently the preparation of diamond-like carbon films from a polymethyl methacrylate (PMMA) target in presence of hydrogen gas has also been reported.<sup>100</sup> The incorporation of  $N_2$  during thin carbon films deposition is found to degrade its DLC character with an improvement in interface adhesion and intrinsic stress.<sup>109</sup>

The laser wavelength used for laser ablation deposition is a critical parameter for laser ablation as it defines the effectiveness of the absorption of laser power onto the target. The effect of laser wavelength on the plume angular distribution has been investigated showing broader angular distribution with IR wavelengths than those obtained with wavelengths in visible and UV.<sup>97</sup> It has been claimed by various groups<sup>148,149</sup> that the use of shorter wavelength leads to the growth of stoichiometric films with better superconducting properties for the  $YBaCuO$  compounds. The reduction in particulate size and density has been reported using UV laser wavelengths.<sup>148</sup> The correlation of laser wavelength on the microstructure of the deposited carbon films has also been reported by Murray and Peeler.<sup>150</sup>

They have shown that the nature and the kinetic energy of the carbon plasma species are highly dependent on laser wavelength. Various researchers<sup>104,107,109,110,151-154</sup> have used different lasers such as ArF (193 nm), KrF (248 nm), XeCl (308 nm), Ruby (694 nm), Ti:Sapphire (780 nm), Nd:YAG (1.064, 0.532, 0.355  $\mu\text{m}$ ) and cw CO<sub>2</sub> (10.6  $\mu\text{m}$ ) etc. for depositing thin diamond like carbon films at various laser irradiances. It is presumed that an effective combination of laser wavelength and the irradiance results in an effective coupling of incident photon energy to the target material and enhances the plasma kinetic energies leading to higher volume fraction of sp<sup>3</sup> bonded carbon atoms.

The other parameter that plays an important role is the choice of the substrate. An atomically flat and chemically compatible substrate is essential for growing high quality ultrathin films. The effect of substrate bias field has been examined during pulsed laser deposition of germanium and carbon films.<sup>83,155,156</sup> Sato et al<sup>155</sup> applied a negative bias to the substrate to accelerate ions and thereby improve the diamond-like character of the films. Wagal et al<sup>156</sup> used a Faraday cage with a biased entrance grid to extract and accelerate ions from the plasma plumes and deposit optically uniform DLC films. Krishnaswamy et al<sup>151</sup> developed a hybrid technique for depositing uniform and homogeneous DLC films by placing a ring electrode between the graphite target and the substrate which is capacitively coupled with the target. Pappas et al<sup>107</sup> have also demonstrated the deposition of DLC films on biased substrates with a high percentage of sp<sup>3</sup> bonds estimated by electron energy loss spectroscopy (EELS). The influence of substrate temperature on film structure has also been investigated. Sato et al<sup>155</sup> have shown a temperature of 50<sup>0</sup> C to be optimal for DLC formation. Recently a transition temperature of 150<sup>0</sup> C from graphite to diamond has been reported by Leppavuori et al.<sup>27</sup> More detailed studies by Cuomo et al<sup>157</sup> have shown that the films deposited have DLC structure at room or lower temperatures while film deposited at elevated temperatures are graphitic in structure. There are also other process parameters such as pulse duration, pulse repetition rate, beam angle with respect to the target surface normal, target rotation speed etc. Usually, these are either fixed for particular type of laser or optimized to minimize "cone" formation, however.<sup>158</sup>

In general, the properties of the carbon films prepared by laser ablation deposition range from soft and graphitic to hard and diamond-like depending on laser power, wavelength and background gas. Several types of laser with the laser intensities ranging from 10<sup>8</sup> - 10<sup>11</sup> W/cm<sup>2</sup> have been used in the deposition of diamond like carbon

films.<sup>27,107,110,150,151,155,157,159-173</sup> Recently the deposition of DLC films using high power Ti:Sapphire laser has also been reported.<sup>154</sup> Figure 2 shows a comparison of different DLC films deposition studies available in the literature. The figure shows that there is a wavelength/irradiance range for the laser ablation deposition parameters favorable for the formation of DLC. The dashed line corresponds to the achievement of a certain energy of the ablated carbon species. In spite of the rough character of the given estimate it shows that there are certain ratios of fluence to laser wavelength beyond which DLC formation is observed. As is obvious from the figure, smaller fluences are required for short wavelength laser to reach in the region of DLC formation.

## **Present Work**

We have deposited carbon films using laser ablation of graphite in presence of helium and argon gas at various pressures and attempted to correlate their formation with the characteristics of that of laser produced carbon plasma. The results on the theoretical modeling of the laser ablation deposition process in the presence of an ambient gas are also discussed. The results on the diagnostics of laser ablated carbon plume for thin film deposition along with the deposited films characterized using several techniques are also presented.

Chapter II presents the experimental techniques developed in the present work. In chapter III, we report on the modeling of the laser ablation deposition process in an ambient atmosphere. Various plasma parameters such as temperature, density and velocity of the plasma species are estimated in order to correlate and understand the deposited films.

Chapter IV describes the results on the diagnostics of the laser ablated carbon plasma used for thin carbon films deposition in presence of helium and argon gas. The carbon plasma was characterized using optical emission and ion probe diagnostics. The optical emission from the plume was found to be dominated by various atomic/ionic species at moderate laser irradiance ( $10^9 - 10^{12}$  W/cm<sup>2</sup>). Assuming local thermodynamical equilibrium (LTE), the electron temperature for C II species was estimated using intensity ratio of the emission lines. Stark broadened profiles of C II transition at  $3p^2P^0 - 4s^2S$  at 392.0 nm were used to calculate the electron density. The temporal profiles of C II specy were used to estimate the velocity of the plasma front. At low laser irradiance ( $10^8 - 10^9$  W/cm<sup>2</sup>), the

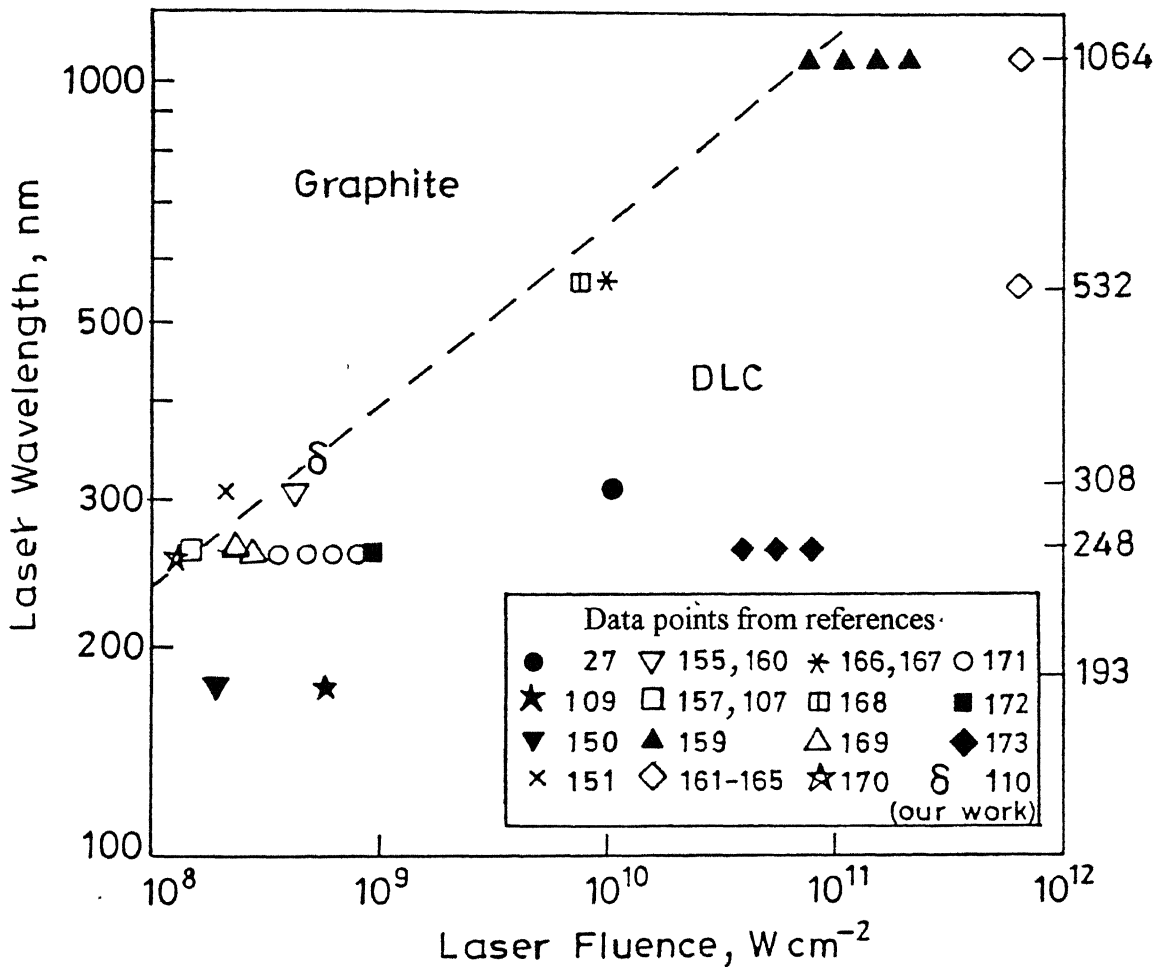


Fig. 2. Laser wavelength and irradiance used to produce diamond like carbon films by several investigators. The dashed imaginary line indicates the region of DLC formation.

molecular  $C_2$  dominated the plasma emission. The presence of an ambient gas increased the intensity of the emitted spectra. The vibrational temperature calculated using  $C_2$  Swan band heads intensity was found to be in the range 6000-12000 K. The vibrational temperature increased with decrease in laser wavelength. The vibrational temperature decreased with increase in helium gas pressure, however, in presence of argon gas it peaked at 1 Torr of argon gas. The temporal profile of  $C_2$  in presence of helium gas showed double peak behavior beyond a certain distance from the target surface. The slow peak follows the drag model and is attributed to the formation of shock waves. The space and angle resolved studies of the plume were performed using ion probes. The temperature, density and velocity of the plasma was estimated at various angular positions with respect to target surface normal, distance from the target surface and ambient gas pressure. The ion densities obtained at various angular positions were fitted to the cosine function and the exponent was found to be highly dependent on ambient gas pressure. The temperature and the velocity was found to be maximum along the target surface normal and decreased with increase in angle.

In chapter V, the results on the characterization of the deposited thin films in ambient atmosphere using scanning electron microscopy, x-ray diffraction, transmission electron microscopy, micro-Raman spectroscopy and resistivity measurements are presented. The films deposited in presence of helium revealed the increasing dominance of  $C_{60}$  with increase in helium gas pressure. The film deposited in presence of argon gas gave diamond like carbon at 1 Torr of argon gas pressure.

Chapter VI summarizes the results of the present work.

## CHAPTER II

### EXPERIMENTAL TECHNIQUES

An overview of various techniques used for thin film deposition, source of the laser ablated plasma and its role in LAD thin film deposition is described in chapter I. We have carried out an extensive study of laser ablated carbon plasma used for thin film deposition with the aim to correlate the growth of thin films with that of plasma characteristics.<sup>54,85,113,174,175</sup> Thin carbon films deposited on glass and silicon substrates at various ambient gas pressures were characterized using various diagnostic techniques.<sup>110,132</sup> Various experimental techniques used/developed for this work are described in the present chapter.

We have used Nd:YAG (Spectra Physics, Model DCR-4G) laser and its harmonics for laser ablation. It delivers energy upto 1 J in 2.5 and 8 ns (FWHM) pulse at fundamental with a repetition rate of 10 pulses per second. The pulse width of the harmonics scales as  $1.06 \mu\text{m}$  pulse width divided by  $\sqrt{2}$ . The laser beam has a Gaussian limited mode structure, the beam divergence being less than 0.5 mrad. The energy of the laser was monitored using a laser power meter (Ophir Model 30A) by placing the meter in the path of the main beam. Laser energy was varied by changing the voltage on the laser oscillator and amplifier. Burn patterns taken at different energies show no significant variation in the mode pattern. The pulse duration was measured using a fast photo diode (Antel, Model AS-2, rise time < 35 ps). The output from the detector was displayed on the storage oscilloscope (Iwatsu, TS-8123) with a  $50 \Omega$  terminator which was triggered externally with a Q-switched synchronous pulse from Nd:YAG laser. The output signal was fed to a personal computer for further data processing. A typical temporal profile of 8 ns (FWHM) pulse at  $1.06 \mu\text{m}$  and 1.8 ns (FWHM) at  $0.532 \mu\text{m}$  corresponding to 2.5 ns (FWHM) at fundamental as shown in figure 3 (a) and (b) respectively. In figure 3 (b), the two peaks around the main pulse are equally spaced beats. The separation between the beats is the cavity round trip transit time. Various harmonics were generated using  $\text{KD}^* \text{P}$  crystals. The prism harmonic separator (PHS) is used for separating second, third and fourth harmonics from the fundamental. The layout of the prism harmonic separator is shown in figure 4. To separate out the harmonics from the fundamental, the Pellin-Broca prism (P-1) was adjusted so that the incident beam passes

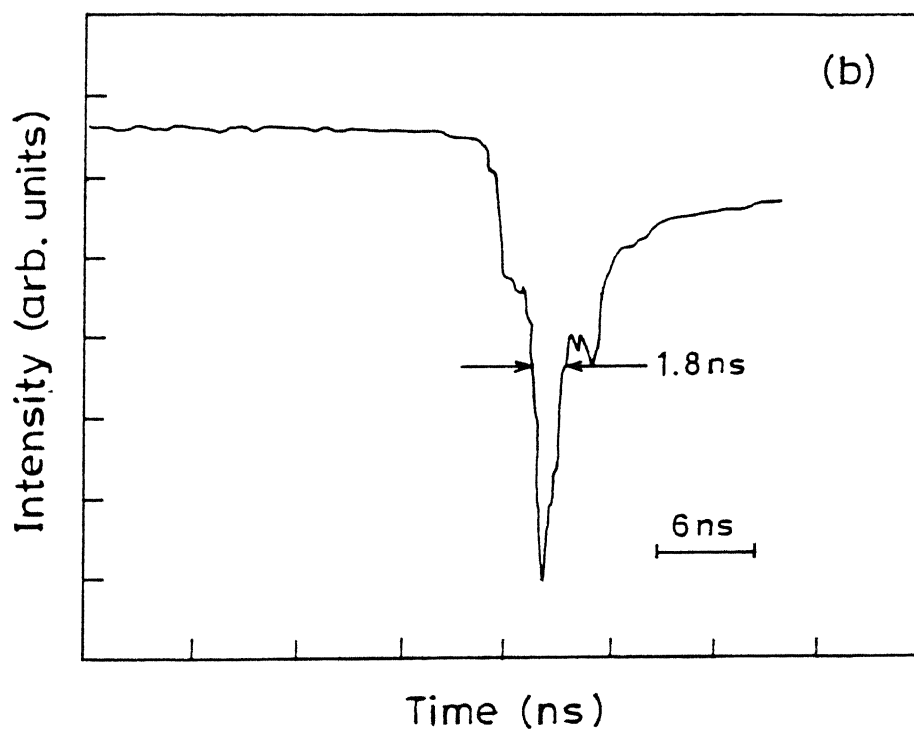
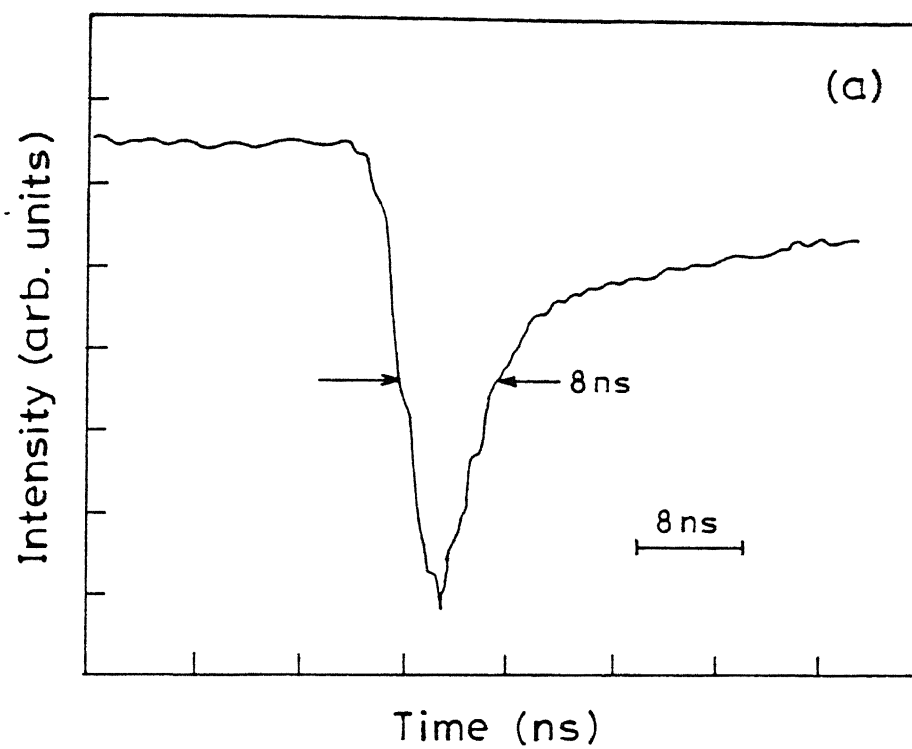
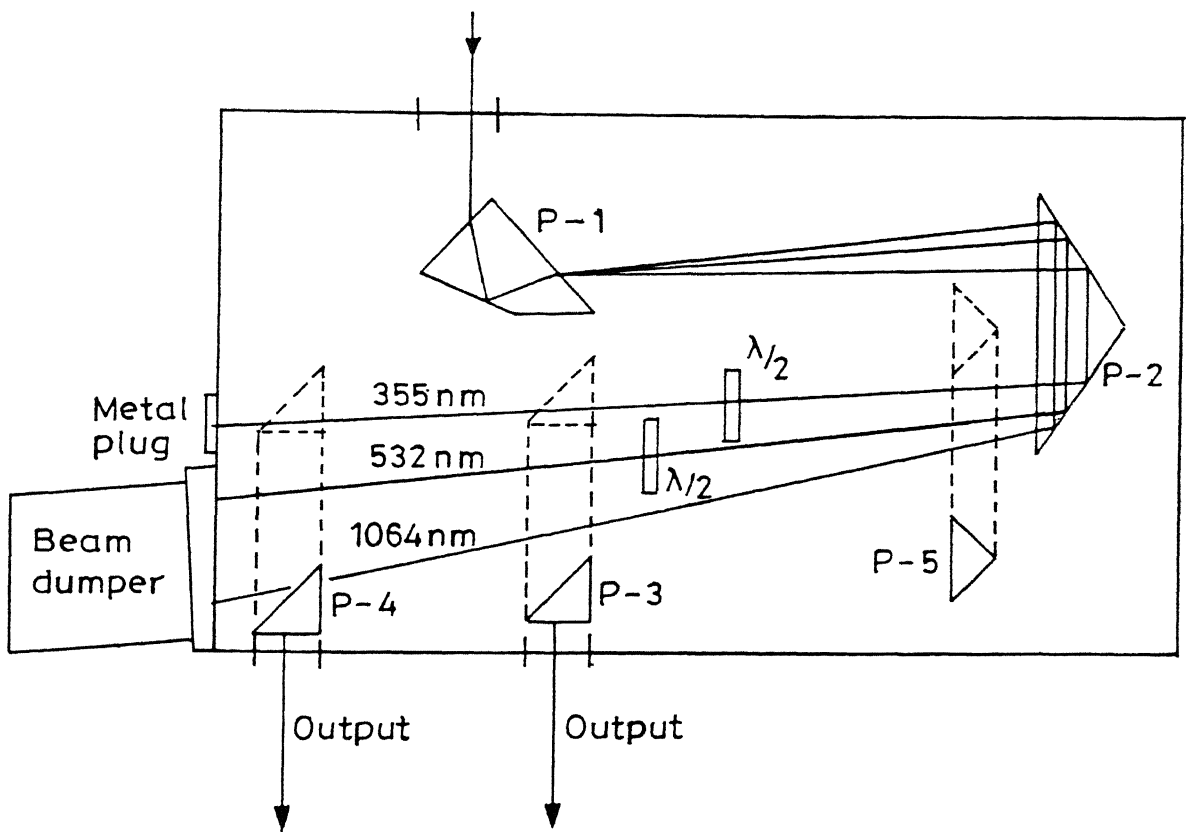


Fig. 3. Typical temporal profile of the Nd:YAG laser (a) 1.06  $\mu\text{m}$ , 8 ns (FWHM) (b) 0.532  $\mu\text{m}$ , 1.8 ns (FWHM).



P-1, P-2, P-3, P-4, and P-5 are Prisms;  $\lambda/2$  is Half-wave plate.

Fig. 4. Prism Harmonic Separator (PHS).



through the centre of it and directs 1.06 and 0.532  $\mu\text{m}$  beams through the roof prism (P-2) into the beam dumper. It was ensured that the 0.532  $\mu\text{m}$  beam also passes through the centre of the half wave plate. The prisms P-4 and P-3 were inserted in the path of 1.06 and 0.532  $\mu\text{m}$  to get the separated outputs from the output windows. In order to separate third harmonic from the fundamental (1.06  $\mu\text{m}$ ) and second harmonic (0.532  $\mu\text{m}$ ), the prism P-1 was adjusted until 0.355  $\mu\text{m}$  beam passes through the centre of the half wave plate and strikes the metal plug next to the beam dumper. Output was taken by moving prism P-3 into the path of 0.355  $\mu\text{m}$  beam so that it passes through the centre of the output window. The fourth harmonic (0.266  $\mu\text{m}$ ) was separated from the other three harmonics after replacing the prisms P-1 and P-3 by quartz prisms. The quartz prism P-5 acts as roof prism P-2 in directing the fourth harmonic onto the output prism P-3 which was adjusted to get the beam at the centre of output window. While looking for harmonics care was taken to direct the unused fundamental and second harmonic beam into the beam dumper.

## **CHARACTERIZATION OF LASER ABLATED CARBON PLUMES**

Laser ablation deposition process involves the formation of laser-induced plasma and the subsequent deposition of plasma species on a substrate. The optimization of the plasma parameters during thin film growth may act as an in-situ diagnostic to obtain the films of desired properties. Hence the study of the plasma plume during the thin film growth is essential for better understanding of the deposited films. Table 1 shows various diagnostic techniques used for studying plasma parameters such as electron temperature, electron density, ion density and velocity of plasma species. We have used the optical emission and ion probe diagnostics to characterize the laser created plasma for our work.

### **I. OPTICAL EMISSION DIAGNOSTICS**

Optical emission spectroscopy has been widely used as a diagnostic during the deposition of thin films by laser ablation. Spectral analysis of plasma emission in the process of laser deposition of thin films gives the information about plasma composition, the energy content of ablation product and the dynamics of plume species which can lead to understanding of the laser ablation phenomena. Investigation of the optical emission of the

**Table 1**

**Various techniques used for LAD plume diagnostics**

Optical Emission Spectroscopy<sup>65, 66, 176-182</sup>

Ion Probe Measurements<sup>83, 84 120, 183-187</sup>

Laser-induced Fluorescence<sup>64, 188-191</sup>

Time of Flight Mass Spectrometry<sup>21, 63, 134, 192-194</sup>

Absorption Spectroscopy<sup>68, 72, 195-199</sup>

Photography and Imaging<sup>79, 200, 201</sup>

plasma plume also gives information about the spatial and temporal evolution of the species produced, such as excited atoms, ions and molecules during laser target interaction. Hence the study of the optical emission from the plume along with the film deposition helps in optimizing the film quality and uniformity.

The interaction chamber and the experimental configuration used for the optical emission diagnostics of laser ablated plume for thin carbon film deposition is shown in figure 5. The laser beam was focused onto the spectroscopic grade pure graphite target rod attached to the target holder in the chamber. The target rod was continuously rotated and translated with the help of an external stepper motor so as to allow each laser pulse to interact with the fresh target surface. The interaction chamber is made up of mild steel with eight output ports. One of the output ports is used for laser entrance and the two perpendicular ports were used for recording the optical emission from the ablated plume. The interaction chamber was evacuated to a pressure better than  $10^{-3}$  Torr using a rotary/diffusion pump. The gas was fed into the chamber from the gas cylinder through a needle valve connected to the interaction chamber. Experiment was carried out in presence of helium and argon gas at various pressures ranging from  $10^{-3}$  - 100 Torr. The chamber was purged several times before filling any gas into it for performing the experiment. The pressure in the chamber was monitored using a thermocouple gauge, oil manometer and a pressure gauge (0-760 Torr). The plasma radiation emitted from the target was imaged onto the entrance slit of monochromator (Jobin Yvon, HRS-2) with a lens of focal length of 16 cm so as to have one to one correspondence with the plasma and its image onto the slit of monochromator. The monochromator was continuously tuned using a microprocessor controlled scan system.<sup>202</sup> The output from the monochromator was detected with a photo multiplier tube (Hamamatsu, IP28) and recorded on a strip chart recorder or displayed on the screen of the storage oscilloscope (Iwatsu, TS-8123) interfaced with PC. The recorded optical emission data is used to evaluate the electron temperature using the emission lines intensity ratio, electron density using Stark broadened profiles of a transition and the vibrational temperature using the intensity of Swan band heads.

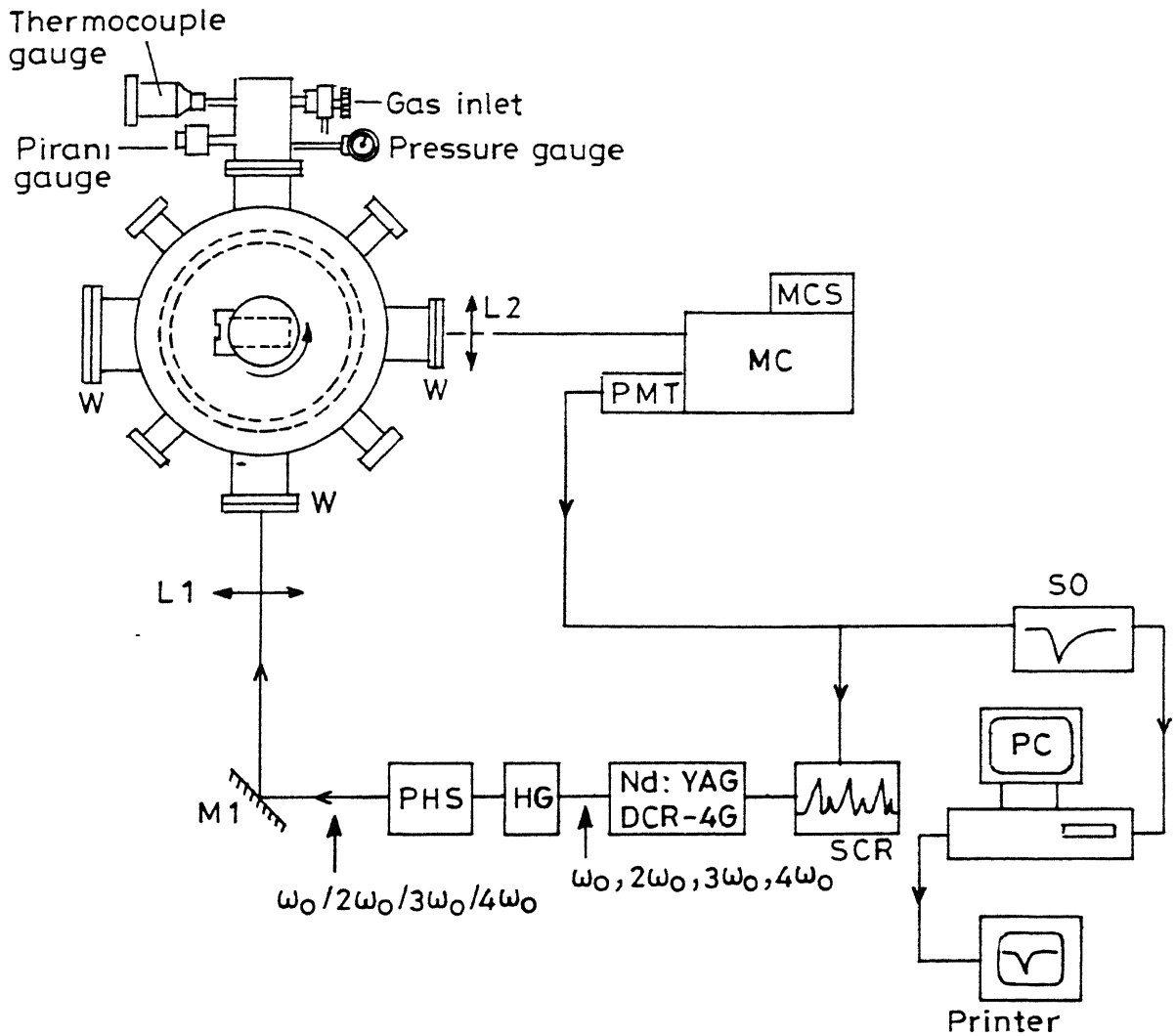


Fig. 5. Schematic of the experimental arrangement for the LAD plume optical emission diagnostics.

## Electron Temperature

Various methods of calculating electron temperature using spectroscopic observations are described in the literature.<sup>203,204</sup> We have used the relative intensities of the spectral lines from a given ionization state for estimating electron temperature. Assuming plasma in local thermodynamic equilibrium (LTE), the electron temperature can be estimated using,<sup>203,205</sup>

$$k_B T_e = \left[ \frac{E' - E''}{\ln \left( \frac{I_s'' \lambda'' g' A'}{I_s' \lambda' g'' A''} \right)} \right] \quad (1)$$

where  $E''$  and  $E'$  are the excitation energies of the lower and upper levels, respectively.  $I_s''$  and  $I_s'$  are the intensities,  $g''$  and  $g'$  are the statistical weights,  $A''$  and  $A'$  are the transition probabilities and  $\lambda''$  and  $\lambda'$  are the wavelengths of various transitions.  $k_B$  and  $T_e$  represents the Boltzmann constant and electron temperature, respectively. The slope of the curve  $E' - E''$  against  $[\ln (I_s'' \lambda'' g' A' / I_s' \lambda' g'' A'')]$  gives electron temperature. The parameters used for estimating electron temperature are available in the literature.<sup>206</sup> The measured electron temperature using intensity of C II species in our work lies between 1 - 9 eV.

## Electron Density

The Stark broadened profile of a transition for which the Stark-broadening parameters are available in the literature, can provide electron densities of the plasma.<sup>58,67,71</sup> Stark-broadening arises due to the coulomb interaction of the emitted species with both the electrons and ions expanding in the plume. The line profiles were recorded keeping the monochromator resolution to maximum. Observed lines were fitted to Lorentzian profile with true half width being given by,<sup>69,202</sup>

$$\Delta\lambda_{\text{true}} = \Delta\lambda_{\text{observed}} - \Delta\lambda_{\text{instrument}} \quad (2)$$

where  $\Delta\lambda$  of a line (FWHM) is given by

$$\Delta\lambda = 2W \left( \frac{n_e}{10^{16}} \right) + 3.5A \left( \frac{n_e}{10^{16}} \right)^{1/4} \times (1 - 1.2N_D^{-1/3}) W \left( \frac{n_e}{10^{16}} \right) \quad (3)$$

First term in the Eq. (3) gives contribution from electron broadening and second term is the ion broadening correction;  $W$  is the electron impact parameter which can be interpolated at different temperatures and  $A$  is the ion broadening parameter, both  $W$  and  $A$  are weak functions of temperature,  $n_e$  is electron density and  $N_D$  is number of particles in Debye sphere given by

$$N_D = 1.72 \times 10^9 \frac{[T(\text{eV})]^{3/2}}{[n_e(\text{cm}^{-3})]^{1/2}} \quad (\text{cm}^{-3}) \quad (4)$$

Eq. (3) is valid only if  $N_D \geq 1$  and  $0.05 < A (n_e / 10^{16})^{1/4} < 0.5$ . Using our measured temperature of 6.25 eV and density  $\sim 4.27 \times 10^{17} / \text{cm}^3$ , we get the number of electrons in the Debye sphere equal to 41 and the parameter  $A(n_e / 10^{16})^{1/4}$  equal to 0.09. Thus the use of Eq. (3) for density measurement is justified. The ionic contribution to the broadening is observed to be much smaller and can be neglected in typical LAD plasmas.<sup>69,207</sup> Considering only the electron impact broadening, Eq. (3) further simplifies to

$$\Delta\lambda = 2 W \left( \frac{N_e}{10^{16}} \right) \quad (A^0) \quad (5)$$

We have used Eq. (5) for estimating electron density of C II transition ( $3p^2P^0 - 4s^2S$ ) at 392.0 nm in the plasma. Electron density using 0.355  $\mu\text{m}$  laser wavelength is found to be  $10^{16} - 10^{18} \text{ cm}^{-3}$ .

### Plasma Expansion Velocity

To calculate the expansion velocity of the plasma front, the temporal profiles of various transitions were recorded at different distances from the target surface.<sup>69</sup> The slope of the curve for the variation of delay of the transient emission intensity maximum of plasma species versus the distance from the target gives the velocity of the plasma front. The

expansion velocity of the C II specy is found to be  $1.2 \times 10^5$  and  $1.9 \times 10^4$  cm/s in vacuum and 1 Torr argon gas respectively.

## Vibrational Temperature

The vibrational temperature was estimated using C<sub>2</sub> Swan band head intensities.<sup>208</sup> The relative population in each vibrational level  $N_{v'}$  can be obtained using a theoretical Franck-Condon factor<sup>209</sup>  $F_{v' v''}$  and the band head intensity  $I_{em}^{v' v''}$  observed at frequency  $\nu$ ,

$$N_{v'} = \frac{C I_{em}^{v' v''}}{D_v F_{v' v''} \nu^4} \quad (6)$$

where C is a constant and  $D_v$  represents the correction factor for the detection system,  $v'$  and  $v''$  are the vibrational levels of the upper and lower electronic states respectively. Since in thermal equilibrium the population  $N_{v'}$  of the initial state is proportional to  $[-G(v')hc/k_B T_{vib}]$ , we have

$$\frac{N_{v'}}{N_{v'=0}} = \exp \left[ \frac{-[G(v') - G(v'=0)] hc}{k_B T_{vib}} \right] \quad (7)$$

where  $G(v')$  is term value of the upper vibrational level  $v'$ ,  $k_B$  is the Boltzmann constant and  $T_{vib}$  is the molecular vibrational temperature. The relative population in each vibrational level are calculated using the Frank-Condon factor from Spindler.<sup>209</sup> The relative population of the upper vibrational levels as derived from the measured intensities is plotted against the vibrational quantum number, the slope of the curve gives the vibrational temperature. The vibrational temperature was calculated at various laser energies and ambient gas pressures using various laser wavelengths. The estimated vibrational temperature lies between 6000 and 12000 K.

## II. ION PROBE DIAGNOSTICS

The ion probes are simple and extremely useful for in-situ diagnostics of the flowing plasmas for LAD. Ion probes provide the local information on plasma conditions unlike emission or absorption spectroscopy, laser-induced fluorescence or imaging techniques which are useful along the line of sight. The schematic of the experimental arrangement for the ion probe diagnostics is shown in figure 6. It consisted of a Langmuir probe made of tungsten wire of 0.6 mm diameter and a power supply. Figure 7 shows a schematic sketch of the probe. The port at an angle of  $45^\circ$ , figure 6, of the interaction chamber with respect to laser entrance port was used for ion-probe diagnostics. The probe to target distance could be varied continuously. The ion probe was connected through a teflon shielded wire to the power supply outside the vacuum chamber. The power supply consisted of a variable -180 V to +180 V DC supply. The probe circuit is shown in figure 7(c). Output signal due to the electron/ion current from the probe was fed to a storage oscilloscope through a  $50\ \Omega$  terminator. The digitized ion probe signals were fed to the PC for further data processing. The experiment was carried out at various argon gas pressures from  $10^{-3}$  to 100 Torr and at various angular positions of the probe ( $\theta$ ) with respect to the target surface normal (TSN). The angle between the ion probe and the target was varied by rotating the target about target holder axis. Immediately prior to each ion probe measurement, the probe tip was cleaned to avoid the contamination on the probe surface. The peak of the ion probe signal ( $I_p$ ) was plotted against the probe voltage ( $V_p$ ) to get  $I_p$ - $V_p$  characteristics. A typical  $I_p$ - $V_p$  characteristics of the ion probe is shown in figure 8. The electron temperature and ion density were calculated using  $I_p$ - $V_p$  behavior of the ion probe.

### Electron Temperature

The evaluation of plasma parameters from the ion probe characteristics depends on the shape of the probe, probe dimension and collision length etc. Assuming Maxwellian velocity distribution of the charge carriers, the total probe current ( $I_p$ ) flowing through the probe is given by<sup>210</sup>



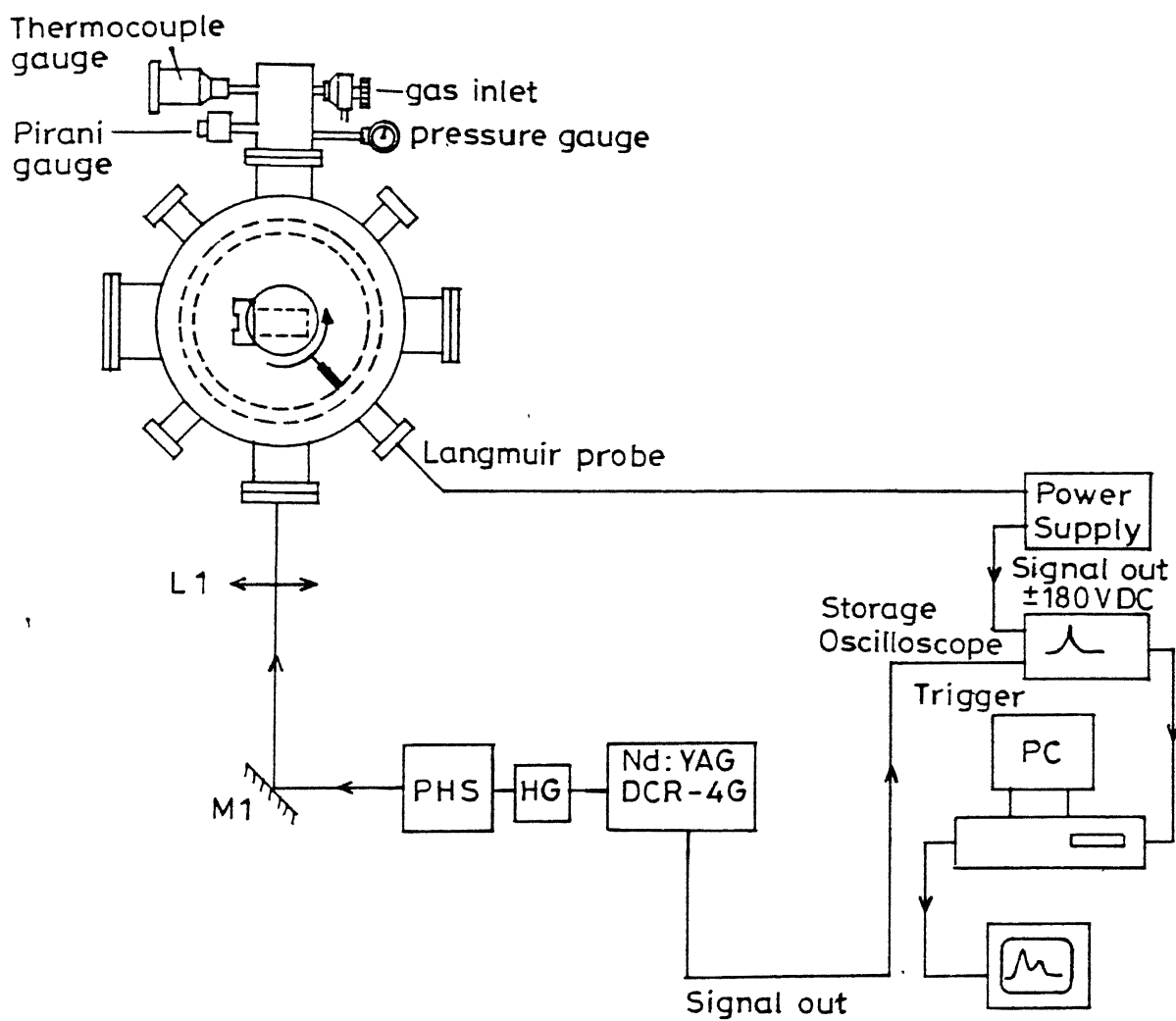
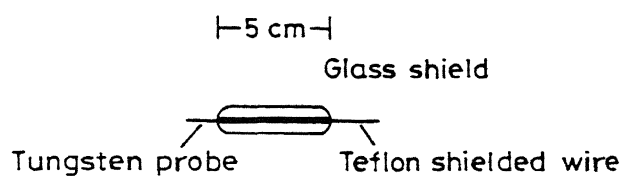
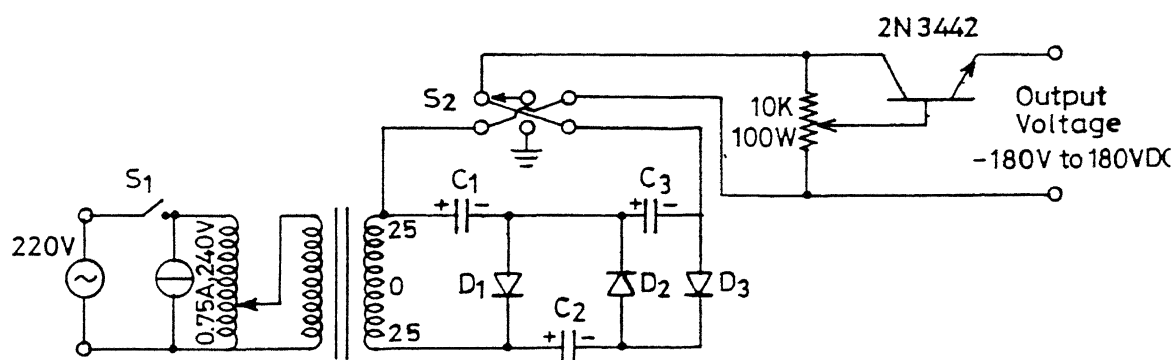


Fig. 6. Schematic of the experimental arrangement for ion probe diagnostics of the plasma plume.



(a)



$$D_1 = D_2 = D_3 \equiv \text{IN4007}$$

$$C_1 = C_2 = C_3 = 1000 \mu\text{f}/200\text{V}$$

(b)

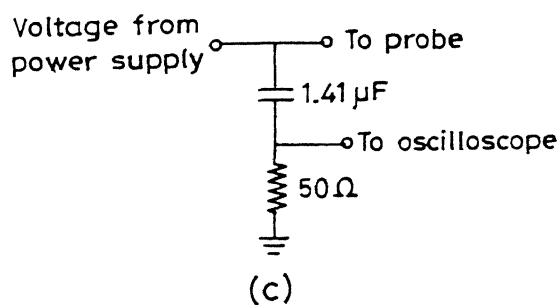


Fig. 7. Sketch of the (a) ion probe assembly (b) power supply (c) ion probe circuit.

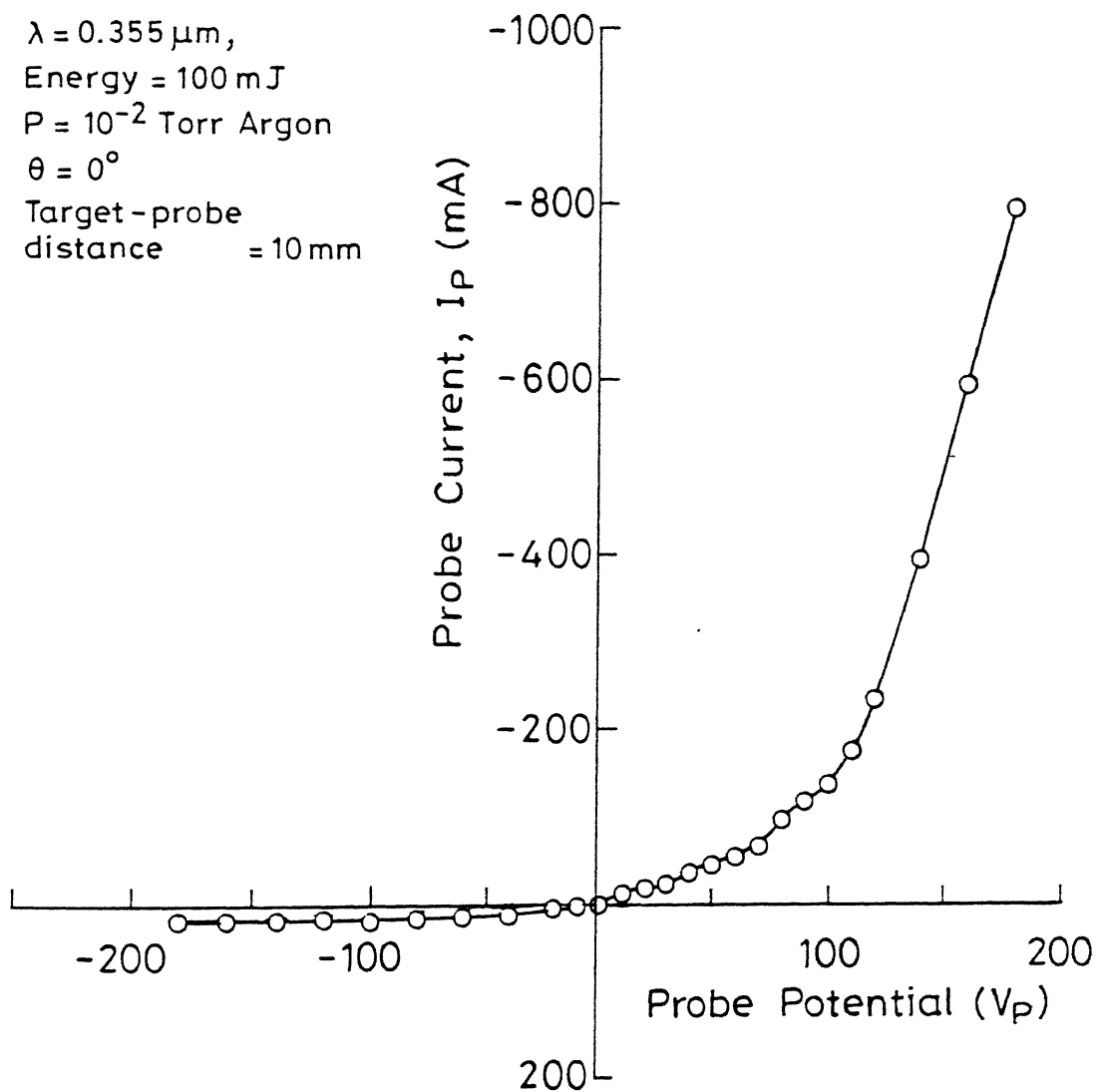


Fig. 8. Typical  $I_P$  -  $V_P$  characteristics of an ion probe.

$$I_P = I_{+0} + I_{e0} \exp\left(\frac{e V_P}{k_B T_e}\right) \quad (8)$$

where  $I_{+0}$ ,  $I_{e0}$ ,  $V_P$ ,  $e$ ,  $T_e$  represents the ion saturation current, electron saturation current, applied probe voltage, charge on the electron and electron temperature respectively. Below electron saturation current, Eq. (8) can be used to estimate  $T_e$  by using the formula,

$$T_e = \left[ \frac{\partial \ln (I_P - I_{+0})}{\partial V_P} \right]^{-1} \quad (\text{eV}) \quad (9)$$

The electron temperatures calculated lie in the range 10-60 eV depending on the ambient pressure.<sup>85</sup>

### **Ion density**

The knowledge of the variation of the ion current with applied probe voltage offers the possibility to estimate the plasma ion density. Several ways of estimating ion density using ion probe characteristics are available in the literature.<sup>210</sup> The second derivative of the probe current with respect to the probe potential yields a straight line for cylindrical probes, the slope of the straight line gives the density,

$$N_i = \left[ \frac{4 \pi m (-dI_P^2 / dV_P)}{3 A_P^2 e^3} \right]^{1/2} \quad (10)$$

where  $N_i$  represents the ion density,  $A_P$  is the area of the ion probe,  $e$  the electron charge and  $m$  is the mass. The ion density calculated using Eq. (10) was found to be  $10^{10} - 10^{14} \text{ cm}^{-3}$ .

## Velocity of Plasma Species

The variation of the time of flight of the ions with distance from the target surface can be used to estimate the velocity of the ionic species. The delay in the maximum of the ion probe signal was plotted against the distance from the target surface, the slope of the curve gives the velocity of the ionic species in the plasma.

## DEPOSITION AND CHARACTERIZATION OF THIN CARBON FILMS

A schematic of the experimental setup used for thin carbon film deposition is shown in figure 9. The laser radiation was line focused onto the graphite target enclosed in a vacuum chamber using a cylindrical lens of focal length 25 cm. The ablated carbon was deposited on silicon and glass substrates placed at 10 mm from and parallel to the target surface. The films were deposited at various helium and argon gas pressures ranging from  $10^{-2}$  to 100 Torr. The deposition time (20 minutes) was kept constant for all the deposited films.

Various techniques used for characterization of the thin films are listed in Table 2. We have used Scanning Electron Microscopy (SEM), X-Ray Diffraction (XRD), Transmission Electron Microscopy (TEM), Raman spectroscopy and Resistivity of the films to characterize the deposited films.

### Scanning Electron Microscopy

Scanning electron microscopy is one of the most widely used analytical tool for studying the structure and surface morphology of the deposited films. We used Scanning Electron Microscope (JEOL, JSM 840A) to record SEM images of the deposited films. The system has a resolution of around  $50 \text{ \AA}$ . The surface morphology of the deposited films showed a strong influence of the nature and the pressure of the ambient gas.<sup>132,174</sup> The film deposited at 1 Torr argon gas showed the maximum nucleation density on the film surface which decreased with change in argon gas pressure on either side.<sup>174</sup>

**Table 2**  
**Different methods used for thin film characterization**

Optical Characterization	Absorption and Luminescence <sup>102, 211, 212</sup> Raman Spectroscopy <sup>213-217</sup> Infrared Spectroscopy <sup>217-219</sup>
Electron Spectroscopy	Photo Electron Spectroscopy (PES) <sup>220, 221</sup> Auger Electron Spectroscopy (AES) <sup>218, 219, 222</sup>
Analytical Electron Microscopy	Scanning Electron Microscopy (SEM) <sup>223-227</sup> Transmission Electron Microscopy (TEM) <sup>224-226</sup> Atomic Force Microscopy (AFM) <sup>227</sup> Scanning Tunneling Microscopy (STM) <sup>228</sup> Electron Energy Loss Spectrometry (EELS) <sup>107, 229</sup> Energy Dispersive X-ray Spectrometry (EDS) <sup>230</sup>
X-ray Analysis	X-ray Diffraction (XRD) <sup>231, 232</sup> X-ray Fluorescence (XRF) <sup>18</sup>
Ion Spectrometry and Microscopy	Secondary Ion Mass Spectrometry (SIMS) <sup>182, 233, 234</sup> Rutherford Back Scattering (RBS) <sup>94, 235, 236</sup>
Magnetic Resonance Methods	Electron Spin Resonance (ESR) <sup>103</sup> Nuclear Magnetic Resonance (NMR) <sup>103</sup>
Electrical Characterization	Electrical Resistivity <sup>108, 152, 237</sup> Electrical Conductivity <sup>108, 152, 237</sup>
Mechanical Characterization	Internal Stress and Adhesion <sup>103</sup> Hardness <sup>103</sup> Frictional Coefficient and wear <sup>103</sup>

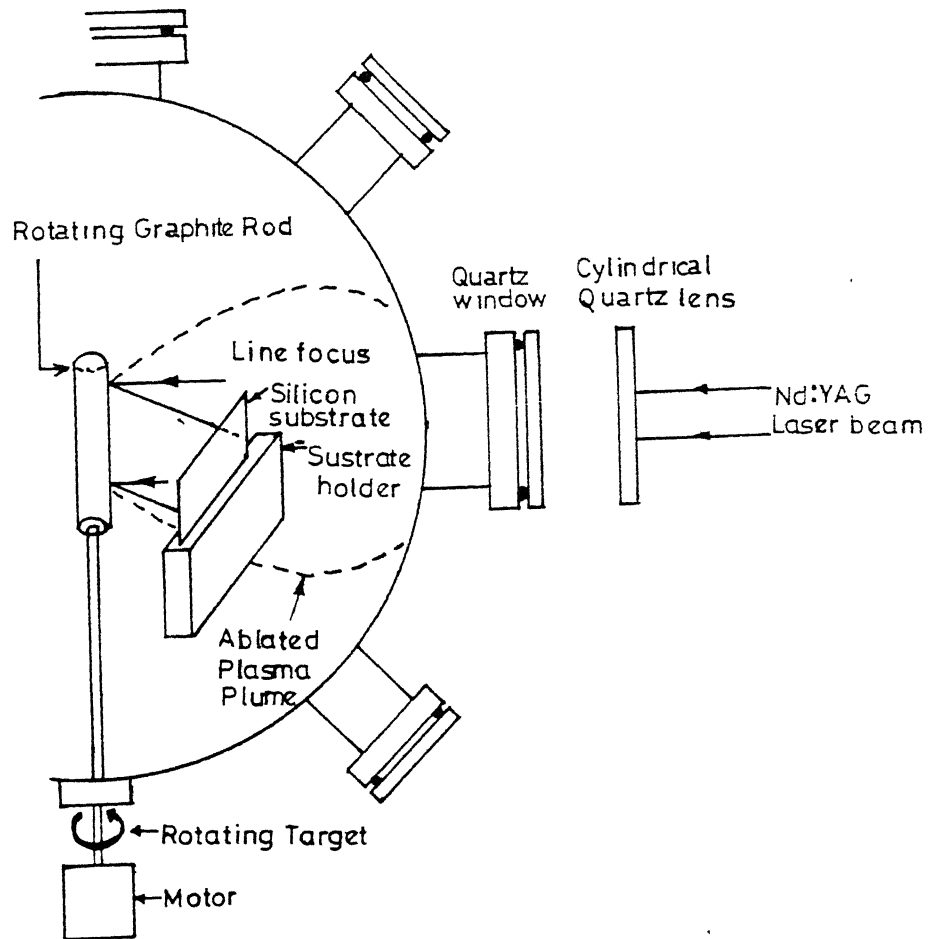


Fig. 9. Schematic of the experimental arrangement for thin carbon film deposition.

## Transmission Electron Microscopy

In TEM a thin solid specimen is bombarded in vacuum with highly focused mono-energetic beam of electrons. The beam has sufficient energy to propagate through the specimen. A series of electromagnetic lenses magnify the transmitted signals. The directly transmitted image is usually referred to as a bright field image, however, an image formed for the diffracted electron is referred to as the dark field image. Detailed micro-diffraction can be obtained by focusing the beam onto the area of the specimen under investigation. This is often referred to as Selected Area Electron Diffraction (SAED). We have used Transmission Electron Microscope (JEOL, JEM-2000-FX-II) to get the structural information of the deposited films. The diameter of the rings observed in the SAED pattern and the calibrated camera constant ( $\lambda L$ ) gave the  $d_{\text{lattice}}$  - spacing of the plane. The  $d_{\text{lattice}}$  - spacing calculated using the SAED pattern of the deposited film at 1 Torr argon matched well with that of diamond.<sup>132</sup>

## X-ray Diffraction

To get the structural information, XRD patterns of the deposited films were obtained using an X-ray diffractometer (Rich-Seifert, JSO-debyeflex 2002) with Cu-K $\alpha$  source. The diffraction pattern gives the maxima in the intensity of the scattered x-rays. The position of the maxima provides information about the size and the shape of the unit cell while the width of the maxima can be used to measure its structural properties such as the size, orientation and strain of grains in polycrystalline materials. Diffraction peaks observed at 43.5 $^{\circ}$ , 76 $^{\circ}$ , 91.5 $^{\circ}$  and 120 $^{\circ}$  show the presence of (111), (220), (311) and (400) crystalline planes of cubic diamond.<sup>110</sup>

## Raman Spectroscopy

Raman spectroscopy has emerged as a very important technique in the characterization of the carbon films due to its ability to distinguish different bonding types, domain size and its sensitivity to internal stresses. The intensity of the Raman peaks is directly proportional to the concentration of the scattering species which provides a basis for



quantitative analysis. We used linearly polarized 514.5 nm (Argon ion laser, Spectra physics) laser radiation as the excitation source. The estimated laser power at the sample was 20 mW, focused to a 30  $\mu\text{m}$  spot. A Spex 1403 double monochromator coupled with a photon counting system was used to record the spectra. The recorded micro-Raman spectra for the carbon films<sup>54</sup> deposited at various argon gas pressures using 0.355  $\mu\text{m}$  laser wavelength showed the presence of two well defined peaks at 1350  $\text{cm}^{-1}$  (D-line) and 1580  $\text{cm}^{-1}$  (G-line).

## Resistivity Measurements

Two-point-probe method<sup>238</sup> was used to measure the resistivity of the deposited films. Figure 10 shows the sketch of the experimental setup used for resistivity measurements. The sample holder was fabricated in house using Lava stone. Two thin gold probes were used to make contact with the film surface. The separation between the probe was about 2 mm. The sample holder was surrounded by a canthal heating tape of 60  $\Omega$  resistance. The temperature was controlled by temperature controller (Indotherm, MPL-500). The complete sample holder assembly was kept inside the cryocan for low temperature measurements. The cryocan could go as low as  $-190^{\circ}\text{C}$  with liquid nitrogen. A variable DC regulated power supply (Aplab, 0-100V) was used for voltage (V) across the probes. The voltage was measured using Digital Multimeter (HIL, 2605). An autoranging picoammeter (Keithley, 485) was used to measure the current (I) flowing through the probes. The I-V behavior of the films was recorded at various temperatures in the range  $-190^{\circ}\text{C}$  to  $+200^{\circ}\text{C}$ . The temperature at the film surface was estimated with the help of K - type thermocouple. The I-V characteristics were used to determine the resistivity using the relation  $\rho = [VA_s/IL]$   $\Omega\text{-cm}$  where  $A_s$  is the cross-sectional area ( $\text{cm}^2$ ) and L is the length (cm).

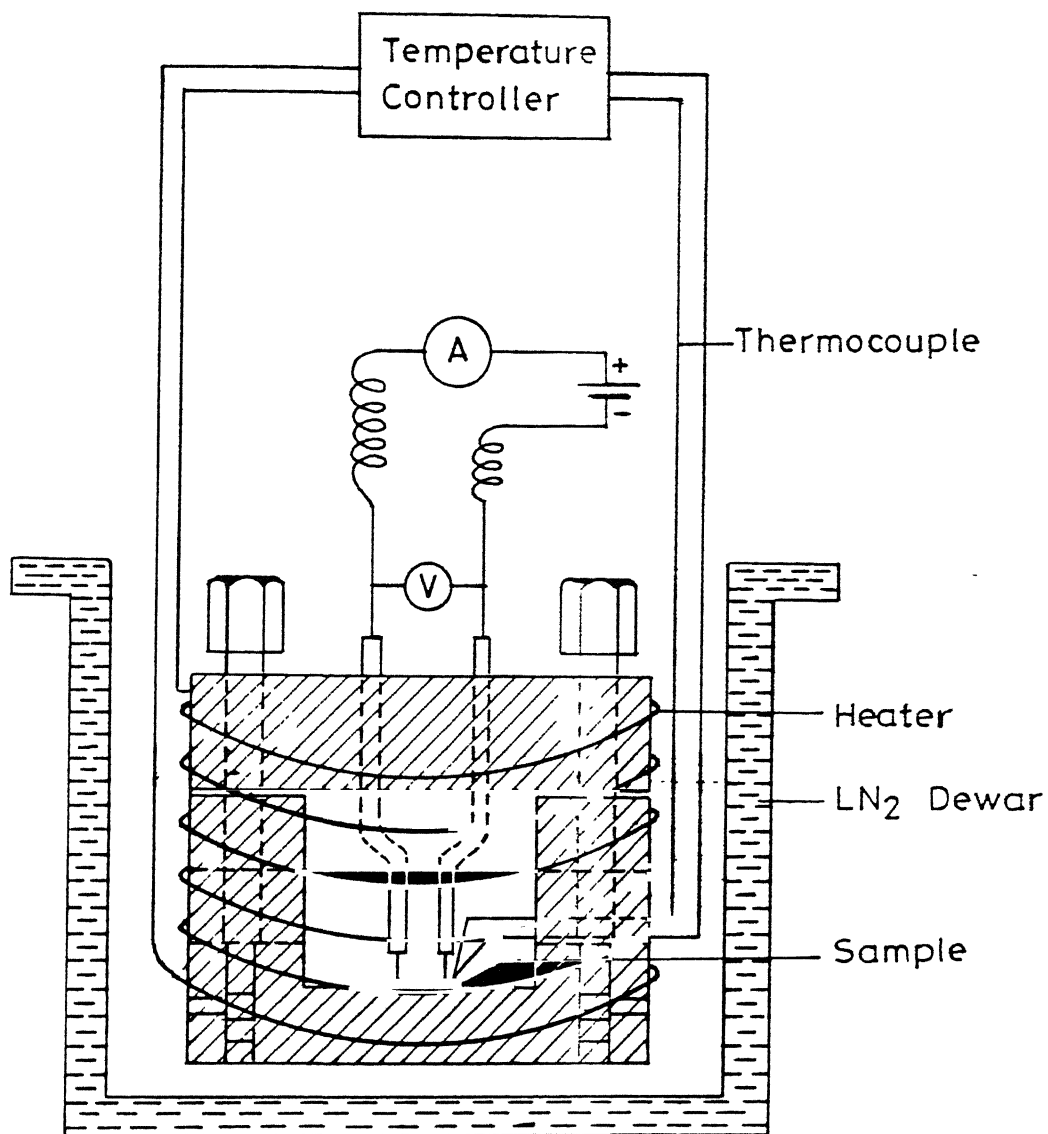


Fig. 10. Experimental setup for resistivity measurement of the films.

## CHAPTER III

### PHOTOABLATED CARBON PLUMES

#### INTRODUCTION

The laser produced plasmas in the presence of an ambient gas are being used to grow good quality films and nanostructures with superior properties relative to conventional manufacturing techniques.<sup>40,132,232</sup> However, in practice the optimisation is rather difficult due to lack of physical understanding of the LAD process. The important steps of laser interaction with matter are laser energy transfer to the target, evaporation of solid material, generation of dense plasma and formation of charged and neutral species, and in case of pulsed laser deposition the interaction of ablated species with the substrate surface. Laser created plasma depends on several laser and target parameters along with the nature and pressure of the ambient gas.<sup>239</sup>

A physical understanding of the dynamics of vaporized plume is crucial to the process of depositing good quality films. The parameters defining the vapor plume conditions include its density, temperature, composition, spatial extent and duration etc. Various parameters for an optimum deposition process have already been discussed in chapter I. The knowledge of the plasma parameters as a function of these control variables may act as an in-situ diagnostics to control the characteristics of the deposited films with desired properties.

Various theoretical models are available in the literature to describe the material removal from a solid surface by high power laser irradiation. The thermal models of Afanas'ev and Krokhin<sup>240</sup> and Olstad and Olander<sup>241</sup> are the early theoretical attempts to understand the problem of material removal using laser. An one dimensional steady state model describing the damage caused by vaporization and liquid expulsion due to the laser irradiation was also developed by Chan and Mazumder.<sup>242</sup> All these models did not describe the behavior and dynamics of the ablated species. Wood and Giles<sup>243</sup> studied the heat transfer and phase change during pulsed laser annealing process based on microscopic diffusion equations. Using finite difference method for solving the diffusion equations the temperature distribution, melting depth, duration of melting and melting front were

calculated. Phipps et al<sup>244</sup> developed a simple model to predict the ablation pressure and the impulse exerted on laser irradiated targets for laser intensities exceeding the plasma formation. Aden et al<sup>245,246</sup> discussed the laser induced expansion of metal vapor against a background gas pressure. Using a compressible gas dynamic model, they described the development of shock discontinuities in the plume. The model proposed by Singh and Narayan<sup>25,86</sup> yielded nonmaxwellian distribution of atomic and molecular species as well as the thickness of the deposited material as a function of target-substrate distance and irradiated spot size. However, the model is not applicable if ambient gas is introduced during deposition. A hydrodynamic model based on the behavior of a gas cloud created by transient desorption from a solid surface has been developed recently by Kools et al.<sup>247,248</sup> The model describes an one dimensional expansion away from the sample and subsequently three dimensional expansion of a gas cloud generated by evaporation of more than a few monolayer of a solid in typical time scales of less than a hundred nanosecond. The model gives semiquantitative prediction of trends in angular distribution and velocity distribution under specified conditions.

Gas dynamic effects are very important and play a leading role in determining the spatial and velocity distribution of vaporized material species. According to gas dynamic approach of Kelly et al<sup>249,250</sup> the collision between the ejectants during the initial expansion leads to a Knudsen layer (KL) or unsteady adiabatic expansion (UAE). The model describes various primary and secondary mechanisms taking place during the laser ablation and explains the results obtained for laser-pulse sputtering of PMMA and YBaCuO targets.<sup>250</sup> It has been shown that the angular distribution of laser generated flux is often much more strongly forward peaked than the flux obtainable from small area effusive source operative under collisionless conditions. It was found that a few collisions per particles can lead to a marked increase in the forward peaking of the emitted particles. A semiquantitative model developed by Saenger<sup>251</sup> describes the spatial non-uniformities in the composition of the pulsed laser deposited multicomponent target films. The propagation of the laser ablated plume in ambient atmosphere is a complex hydrodynamic problem. It has been shown that the plasma expanding against a background gas forms a shock wave.<sup>252</sup> As the shock expands, more and more background gas is swept up by the shock. Since the laser ablation delivers a finite energy the expansion velocity decreases with increasing distance from the target. Various investigators have used drag/shock wave model<sup>77,79,80,179,253-255</sup> to explain

their own experimental results. Although the laser ablation in presence of background gas is gaining much interest the models describing the LAD process in ambient atmosphere are rare. The combined theoretical and experimental approach for laser ablation deposition process may help to understand various aspects of the deposition process such as collisional interaction between the particles in the plume and the background gas, interaction of the energetic species with the substrate affecting the film quality and the hydrodynamic behavior of the vapor/plasma during and after ablating pulse.

In the present chapter, a numerical model for LAD of carbon in an ambient atmosphere is discussed. Dependence of various plasma parameters such as electron temperature, density and velocity of plasma as a function of time and distance from the target surface based on the model is presented.

### **Physical Aspects of Laser Ablation Deposition Process**

Laser ablation deposition process can be divided into three different regimes:

- (1) Laser-target interaction resulting in the evaporation of surface layers (Evaporation regime).
- (2) Laser-plasma interaction leading to the formation of a high temperature isothermal expanding plasma (Isothermal regime).
- (3) Adiabatic expansion of the plume and thin film growth (Adiabatic regime).

### **Laser-Target Interaction**

The interaction of laser light with the target surface depends mainly on the incident energy density, duration, wavelength of the laser light and temperature dependent optical and thermophysical properties of the material.<sup>15,23</sup> For low laser irradiation ( $\sim 10^6 \text{ W/cm}^2$ ) the absorbed radiation appears as heat which is slowly distributed throughout the material by thermal diffusion. For conducting material the incident laser energy is absorbed within a skin depth. At slightly higher laser irradiation ( $>10^6 \text{ W/cm}^2$ ) depending on the thermal conductivity, thermal diffusivity, reflectivity of the target material and the parameters of the laser pulse, intense local heating of the surface occurs resulting in a rise in surface temperature of the material. As the irradiation increases the temperature of the surface

increases and a molten pool of depth  $(D \tau_L)^{1/2}$  is formed, where  $D$  is thermal diffusivity and  $\tau_L$  is the laser pulse duration time. The standard heat equation can be used to calculate the increase in temperature. A further increase in the laser irradiation will cause the surface temperature of the molten pool to reach the boiling point resulting in evaporation. This will happen when the energy deposited is approximately equal to the latent heat of sublimation  $L_s$  (J/kg)  $= I_L \tau_L^{0.5} \rho_s^{-1} D^{-0.5}$  where  $\rho_s$  is the density of the solid target and  $I_L$  is the intensity of the laser irradiation.

The removal of the material from the target surface by laser irradiation depends on the coupling of laser beam energy with the solid. The irradiation of the target surface by pulsed laser results in melting and/or evaporation of the surface layers. The quantities of interest determining the evaporation process are the optical absorption depth  $\alpha^{-1}$  and thermal diffusion length  $L_{th} = (2D \tau_L)^{1/2}$ , where  $\alpha$  is the linear absorption coefficient. If the optical absorption depth is much smaller than the thermal diffusion length,  $\alpha^{-1} \ll L_{th}$  the energy absorbed is not appreciably diffusible from the surface region but mostly used to excite the atoms and particles, consequently surface heating occurs. The amount of material evaporated can be calculated using energy balance considerations. The energy deposited by the laser beam on the target is equal to the energy needed to vaporize the surface layers, the conduction losses in the target and the losses due to the absorption of the laser energy by the expanding plasma. The thickness of the target material evaporated/pulse ( $\Delta x_t$ ) is given by,

$$(1-R)[E - (\text{Conduction losses} + \text{Plasma losses})] = \Delta x_t [\rho_s C_p \Delta T + E \Delta H] \quad (11)$$

where  $R$ ,  $\rho_s$ ,  $C_p$ ,  $\Delta T$  and  $\Delta H$  represents the reflectivity, mass density, heat capacity, temperature rise and volume latent heat of the target material respectively. Since  $\Delta H \gg \rho_s C_p \Delta T$ , Eq. (11) gives

$$\Delta x_t = (1-R) \left[ \frac{E - E_{th}}{\Delta H} \right] \quad (\text{cm}) \quad (12)$$

Here  $E_{th}$  is the laser energy threshold. At higher laser energies Eq. (12) is no more valid due to the change in plasma losses and the variation in reflectivity. When  $\alpha^{-1} \gg L_{th}$ , thermal diffusivity does not play a major role and the evaporation depth is dependent on the

attenuation distance of the laser beam. It shows the logarithmic dependence of evaporated depth with laser energy. This regime is generally applicable for polymers and nonmetallic solids having low thermal diffusivity and absorption coefficient. The thickness ( $\Delta x_t$ ) of the evaporated material is an important parameter controlling the plasma absorption of the laser beam.

### Laser-Plasma Interaction

The interaction of the high power laser beams with the bulk target leads to very high surface temperature resulting in the emission of positive ions and electrons from the target surface. The flux of the electrons and ions can be predicted by Richardson and Langmuir-Saha equations respectively. The physical mechanisms involved in the penetration and absorption of laser energy by plasma depends on electron density, temperature as well as the wavelength of the laser light in general.<sup>256-260</sup> The dispersion relation for an electromagnetic wave travelling through plasma is given by

$$\omega^2 - \omega_p^2 = k^2 c^2, \quad (13)$$

where  $\omega_p$  is the plasma frequency,  $\omega_p = (4 \pi n_e e^2 / m_e)^{1/2}$  Hz,  $c$  is the speed of light,  $k$  is the propagation vector and  $n_e$  is the electron density. For  $\omega > \omega_p$ ,  $k$  is real and the propagation of electromagnetic wave take place whereas for  $\omega < \omega_p$ ,  $k$  is imaginary and the wave is not propagated at all. At  $\omega = \omega_p$ , the reflection of laser light occurs at the density called the critical density  $n_c = [m_e \omega^2 / 4 \pi e^2]$ . Most of the absorption of laser energy occurs at or close to  $n_c$ . For the third harmonic of Nd:YAG laser (355 nm), the laser frequency corresponds to  $8.45 \times 10^{14} \text{ s}^{-1}$  which gives the critical electron density equal to  $9.0 \times 10^{21} \text{ cm}^{-3}$ . This high value of  $n_c$  indicates that reflection losses of the laser beam from the plasma can be neglected. The laser light is absorbed in the plasma by an inverse bremsstrahlung process which occurs due to electron-ion collisions in the plasma. The absorption coefficient is given by,

$$\alpha_p = 3.69 \times 10^8 \left( \frac{Z^3 n_i^2}{T_e^{0.5} v^3} \right) \left[ 1 - \exp\left( \frac{-h\nu}{k_B T_e} \right) \right] \quad (\text{cm}^{-1}) \quad (14)$$

where  $Z$ ,  $n_i$  and  $T_e$  are respectively the average charge, ion density and temperature of the plasma,  $h$ ,  $k_B$  and  $\nu$  are the Planck's constant, Boltzmann constant and the frequency of the laser light respectively. The laser light is highly absorbed if  $(\alpha_p z)$  is large, where  $z$  is the distance perpendicular to the target of the expanding plasma. The term  $[1 - \exp(-h\nu/k_B T_e)]$  represents the losses due to stimulated emission which depends on the plasma temperature and laser frequency. For 355 nm laser wavelength, the exponential term becomes unity for  $T \ll 40416$  K and can be approximated by  $h\nu/kT$  for  $T \gg 40416$  K. The absorption term shows a  $T^{0.5}$  dependence for low temperature and  $T^{1.5}$  for high temperatures. The dependence of frequency also changes from  $\nu^2$  to  $\nu^3$  depending on the value of  $(h\nu/kT)$ . Eq. (14) shows that the rate of absorption depends on  $n_i^2$ . The absorbed energy causes an increase in kinetic energy of electrons i.e., an increase in electron temperature and this in turn produces further ionization with a consequent increase in electron density. Hence the rate of absorption and with it the rate of ionization adjusts such that the electron density increases further and approaches a critical density at which plasma becomes opaque. However, plasma growth does not cease. Due to the high expansion velocity of the plasma leading edge, the electron and ion density decreases very rapidly with time thereby making plasma transparent to the laser beam.

A schematic of the laser plasma-target interaction is shown in figure 11. The figure shows the four different regions during the incidence of the laser pulse : (A) unaffected bulk target, (B) evaporated target material, (C) dense plasma absorbing laser radiation, and (D) rapidly expanding plasma outer edge transparent to the laser beam. It is reasonable to assume an isothermal temperature during the time of laser pulse for laser ablation deposition. A dynamic equilibrium exists between the plasma absorption and the rapid transfer of thermal energy into kinetic energy. These two mechanisms regulate the isothermal temperature attained by the plasma. At even higher density, when an appreciable amount of energy is absorbed by the plasma, a self regulating regime exist near the target surface. We can justify the formation of self regulating regimes as follows. If the absorption of the laser light by plasma becomes high (due to the lowering of temperature) the evaporation of the species from the target becomes less, thus decreasing the density of the ionized species. Its consequence is the increase in the absorption of laser energy and the temperature of the plasma. If instead, the absorption of plasma is less, the process is reversed with similar results. It has been shown<sup>261</sup> that the density, temperature and the plasma length



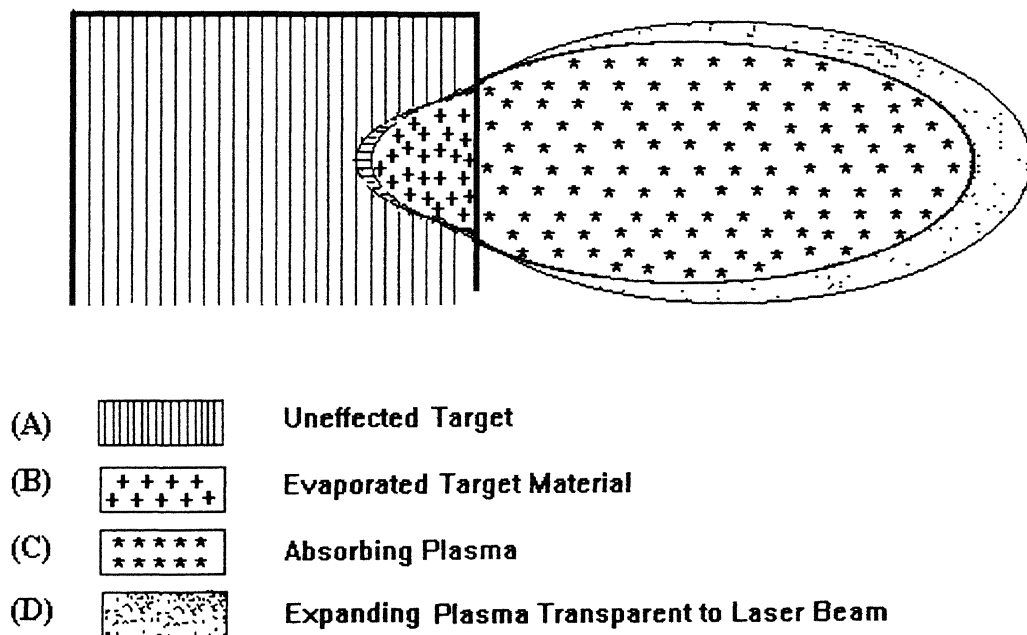


Fig. 11. Schematic diagram showing the different phases present during laser ablation of a target (A) unaffected target (B) evaporated target material (C) dense plasma absorbing laser radiation and (D) expanding plasma outer edge transparent to the laser beam.

adjusts in such a manner that it absorbs the same amount of incoming laser radiation. Also due to the small plasma volume, the radiation losses are negligible.<sup>15</sup> Hence, it is reasonable to assume that the plasma losses are insignificant for the condition of LAD. In the initial stages of plasma expansion, the particle density is high and mean free path of the particles is small, the plasma can be assumed to behave as fluid. The expansion of plasma can be simulated using the gas dynamic equations, adiabatic equation of state and equation of temperature<sup>257</sup> viz;

$$n M \left( \frac{\partial v}{\partial t} \right) + (v \cdot \nabla) v = - \nabla P \quad (15)$$

$$\left( \frac{\partial v}{\partial t} \right) + \nabla \cdot (n v) = 0 \quad (16)$$

$$\left( \frac{1}{P} \right) \left( \frac{\partial P}{\partial t} + v \cdot \nabla P \right) - \left( \frac{\gamma}{n} \right) \left( \frac{\partial n}{\partial t} + v \cdot \nabla n \right) = 0 \quad (17)$$

$$\frac{\partial P}{\partial t} + v \cdot \nabla T = (1 - \gamma) T \nabla \cdot v \quad (18)$$

Here  $n$  is the number density,  $v$  is the velocity,  $P$  is the pressure and  $\gamma (= C_p / C_v)$  is the adiabatic exponent. The density of the plasma can be expressed as a Gaussian function given by

$$n(x, y, z, t) = \frac{N_T t}{\sqrt{2\pi}^3 \tau_L X(t)Y(t)Z(t)} \exp \left[ -\frac{x^2}{2X(t)^2} - \frac{y^2}{2Y(t)^2} - \frac{z^2}{2Z(t)^2} \right] \quad (19)$$

where  $N_T$  is the total number of ablated species at  $t = \tau_L$ . The evaporation rate of the target material being constant, a linear increase in number of particles in the plasma during the laser pulse is incorporated in Eq. (19). We assume plasma as an ideal gas, the pressure at any point can be expressed as

$$P(x, y, z, t) = n(x, y, z, t) k_B T \quad (20)$$

It has been shown that the gasdynamic equations follow similarity transformations<sup>252</sup> in which the velocity can be expressed as

$$\mathbf{v} = \hat{i} \frac{x}{X(t)} \frac{dX(t)}{dt} + \hat{j} \frac{y}{Y(t)} \frac{dY(t)}{dt} + \hat{k} \frac{z}{Z(t)} \frac{dZ(t)}{dt} \quad (21)$$

Substitution of Eq. (19) and (21) into the equation of motion gives rise to the following condition,

$$X(t) \left[ \frac{1}{t} \frac{dX}{dt} + \frac{d^2X}{dt^2} \right] = \frac{k_B T_0}{M} \quad (22)$$

where  $T_0$  is isothermal temperature of the plasma. Similar equations can be derived for the other two directions of expansion. To estimate the initial plasma expansion we have used Eq. (22). The initial dimensions  $X_0$  and  $Y_0$  are taken as the laser spot size  $130 \mu\text{m}$  while  $Z_0$  is less than  $1 \mu\text{m}$ . It can be seen from the Eq. (22) that the expansion velocity and the initial acceleration are governed by the dimension of the plasma. During the initial expansion stage, when the velocities are small, the acceleration is very high. With an increase in expansion velocity, acceleration starts to decrease and ultimately becomes zero resulting in an elongated plasma shape. Since the plasma dimensions are much smaller along the target normal than in the transverse direction, the expansion is anisotropic in nature.

### Adiabatic Expansion of the Plume

After the termination of the laser pulse the injection of the particles into the inner edge of the plasma is stopped giving rise to the adiabatic expansion of the plasma. The thermal energy rapidly gets converted to kinetic energy giving higher expansion velocities of the plasma. As the number of particles in this regime remains constant, the density and pressure can be written similar to Eq. (19) and (20). The density  $n$  of the plasma becomes

$$n(x, y, z, t) = \frac{N_T}{\sqrt{2} \pi^{1.5} X(t)Y(t)Z(t)} \exp \left[ -\frac{x^2}{2X(t)^2} - \frac{y^2}{2Y(t)^2} - \frac{z^2}{2Z(t)^2} \right] \quad (23)$$

The velocity expression remains similar to Eq. (21). Substitution of density, velocity and pressure into Eqs. (15) to (18) yields

$$X(t) \frac{d^2X}{dt^2} = Y(t) \frac{d^2Y}{dt^2} = Z(t) \frac{d^2Z}{dt^2} = \frac{k_B T_0}{M} \left[ \frac{X_0 Y_0 Z_0}{X(t) Y(t) Z(t)} \right]^{\gamma-1} \quad (24)$$

where  $X_0$ ,  $Y_0$  and  $Z_0$  are the dimensions of the plasma at  $t = \tau_L$ . Eq. (24) shows that the acceleration of plasma species depends on the temperature and dimensions of the plasma. It gives rise to the largest expansion in the direction perpendicular to the target surface giving forward directed nature of the LAD process. Solving Eq. (24) numerically gives the plasma dimensions and velocity. Figure 12 shows the variation of the plasma dimensions as a function of time. The calculations were carried out for graphite target irradiated with Nd:YAG laser ( $\lambda = 355$  nm,  $\tau_L = 5$  ns and focal spot diameter =  $260 \mu\text{m}$ ). The plasma dimensions are seen to increase in all directions with the expansion being larger along the target normal as compared to other directions. The dependence of the velocity of the plasma with time is shown in figure 13. The velocity first increases with increase in time and becomes constant at later time. The velocity is larger along the target normal in agreement with our experimental results.<sup>85</sup> It indicates that the deposition of the film along the target normal may lead to optimum quality film. Also, the film deposition along the target normal is possible at longer distances due to its higher expansion along the target surface normal. Figure 14 shows the variation of plasma temperature with time. The temperature of the plasma remains constant during the time of the laser pulse and then decreases with increase in time due to the expansion of the plasma.

Since LAD usually requires an ambient environment, the model presented above cannot be applied and needs to be modified. The laser ablation in the presence of an ambient gas may result in slowing of the plume relative to its propagation in vacuum, spatial confinement and sharpening of the plume boundary indicative of shock front etc.<sup>253</sup> Different diagnostics of the laser-matter interaction in presence of an ambient gas have shown that the plume interacts hydrodynamically with the background gas. A blast wave model has been used to describe the luminous shock front caused by the expansion of laser produced plasma.<sup>77,79,80,179,254,255</sup> However, a classical drag force model is used at low background gas pressures such as those employed for LAD.<sup>262</sup>

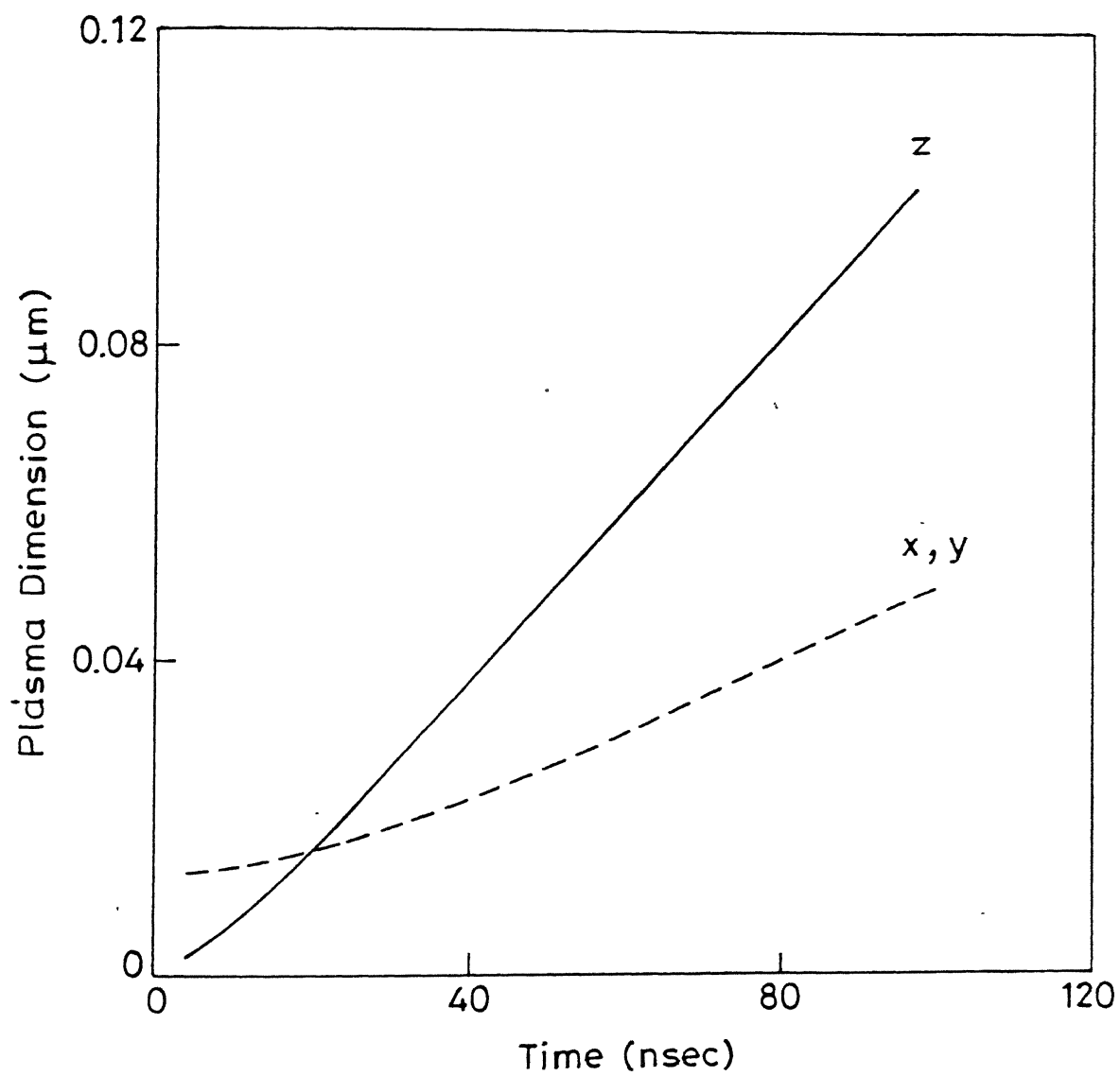


Fig. 12. Dependence of the plasma dimensions on time in vacuum.

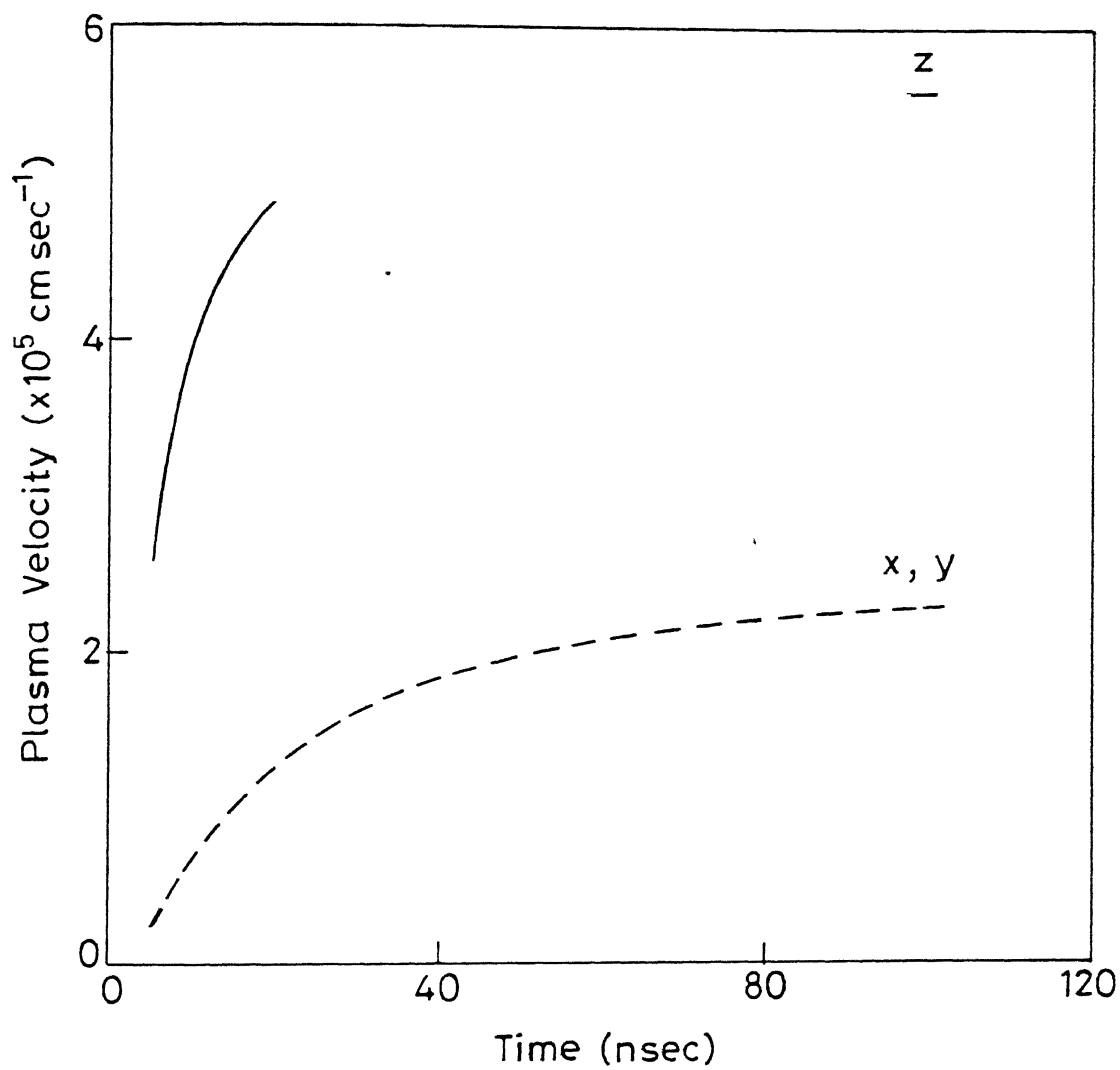


Fig. 13. Variation of the velocity of carbon plasma front with time in vacuum.

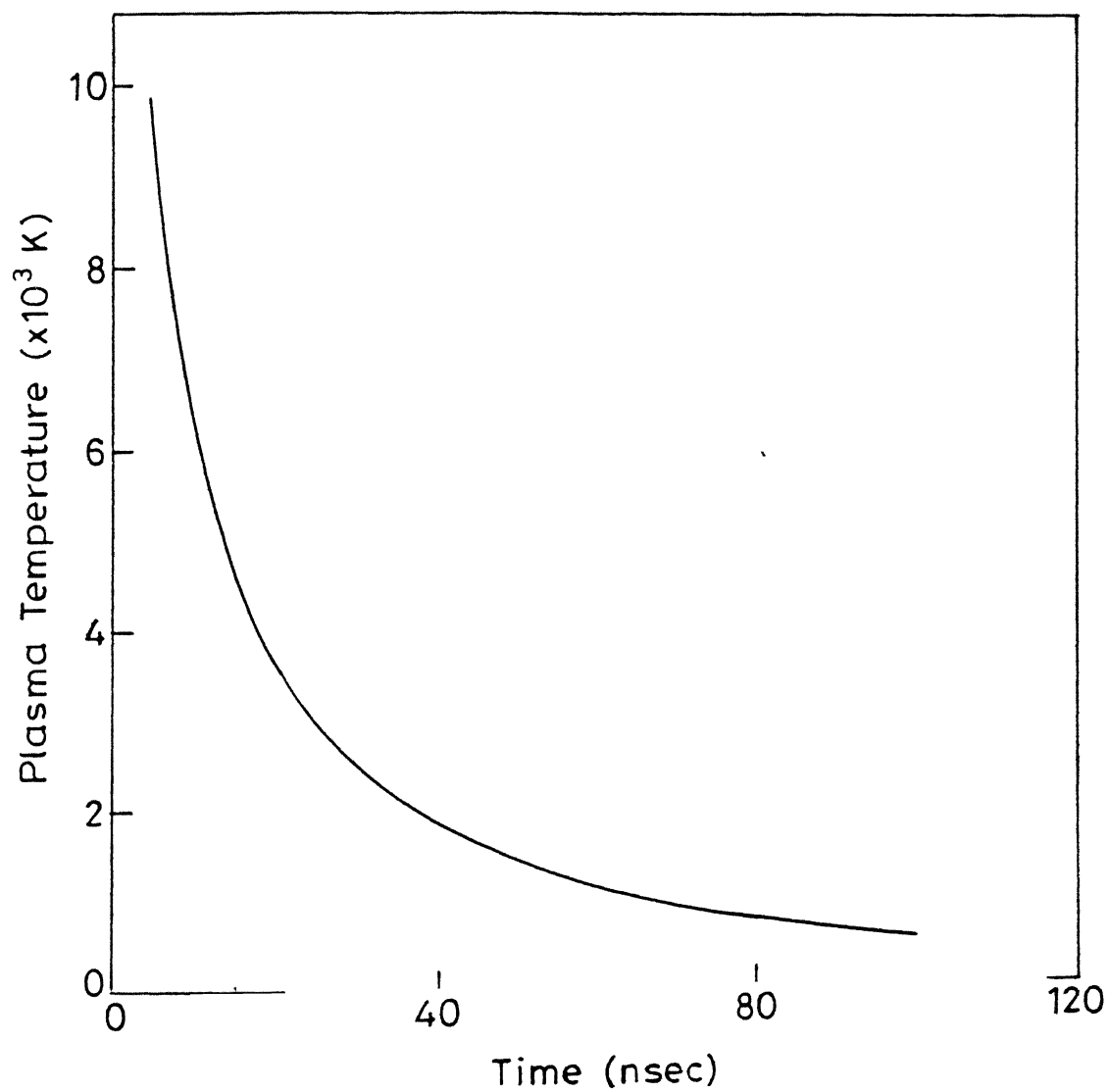


Fig. 14. Variation of plasma temperature as a function of time.

It has been shown by several investigators<sup>254,262,263</sup> that the expansion dynamics of the plume during initial stages of expansion remains unhindered by the environmental gas and resembles free expansion in vacuum. We assume that the initial density distribution for ablation in gas corresponds to that in vacuum if the number of collisions between plasma species and background gas atoms are negligible and it is true up to mean free path (mfp) only. Hence the background gas will play a role after the mean free path which is given by

$$\text{mfp} = \frac{k_B T}{\pi r^2 P_o} \quad (25)$$

where  $T$  is the temperature of the gas,  $P_o$  is gas pressure and  $r$  is the sum of the radii of the colliding partners. During the expansion of the plume, the pressure within the plume decreases and approaches the pressure of the ambient gas ( $P_o$ ) i.e.,

$$P(x, y, z, t) = P_o. \quad (26)$$

The distance at which the above relation is satisfied gives the plume length,  $L_P$  given by<sup>21</sup>

$$L_P = \zeta \left[ \frac{(\gamma-1) \epsilon E_P V_o^{\gamma-1}}{P_o} \right]^{1/3\gamma} \quad (27)$$

where  $E_P$  is the laser pulse energy,  $\epsilon$  is the fraction of laser energy absorbed in the plasma plume,  $V_o$  is the initial volume of the plume,  $P_o$  is the background gas pressure and  $\zeta$  is the geometrical factor. The plume length is the distance after which the ambient gas can diffuse inside the plume. We assume that a classical drag force proportional to its velocity acts on the plasma plume in presence of background gas. A drag force term  $(-\beta v)$  where  $\beta$  is the slowing coefficient is introduced in Eq. (15).  $\beta$  is defined as  $L_P / v_o$ ,  $v_o$  being the initial velocity of plasma. Assuming Maxwell-Boltzmann distribution function for density, Eq. (15) reduces to

$$v_x = v_{x0} e^{-\beta t} \quad (28)$$



where  $v_{xo}$  is the x-component of the velocity of the plasma after traversing a distance equal to mfp. Similar equations can be obtained for other directions also.

The velocity of the plasma decreases in presence of an ambient gas with increase in time. The decrease in velocity depends on  $\beta$  which in turn depends on the ambient pressure. Figure 15 shows the variation of the plasma velocity with distance from the target surface in presence of argon gas at various pressures. The velocity of the plasma first increases with increase in distance and then decreases beyond a certain distance. The distance beyond which the velocity of the plasma decreases depends on the ambient gas pressure. It is seen to decrease with increase in ambient gas pressure.

The film thickness  $t(x, y)$  at any point on the substrate can be calculated by summing up all the particles striking the substrate. It can be expressed as

$$t(x, y) = \int_0^{\infty} n(x, y, z) v(t) dt. \quad (29)$$

We have used Eq. (29) to calculate the film thickness. Figure 16 shows the variation of the film thickness with distance from the centre of the film. The thickness is seen to decrease with increase in distance. It indicates that most of the ablated material is deposited in the region perpendicular to the irradiated spot. Our ion probe diagnostics results<sup>85</sup> on the variation of ion density with angle from the target surface normal match well with the simulated thickness profile. It showed the ion density to be maximum along the target normal giving more thickness along the normal.

In conclusion, a hydrodynamic model of LAD in an ambient atmosphere is discussed. Various plasma parameters such as temperature, density and velocity of the plasma species are highly dependent on the nature of the surroundings. The simulated thickness of the film is seen to decrease with increase in distance from the centre of the film and shows the same trend as observed for ion density experimentally.

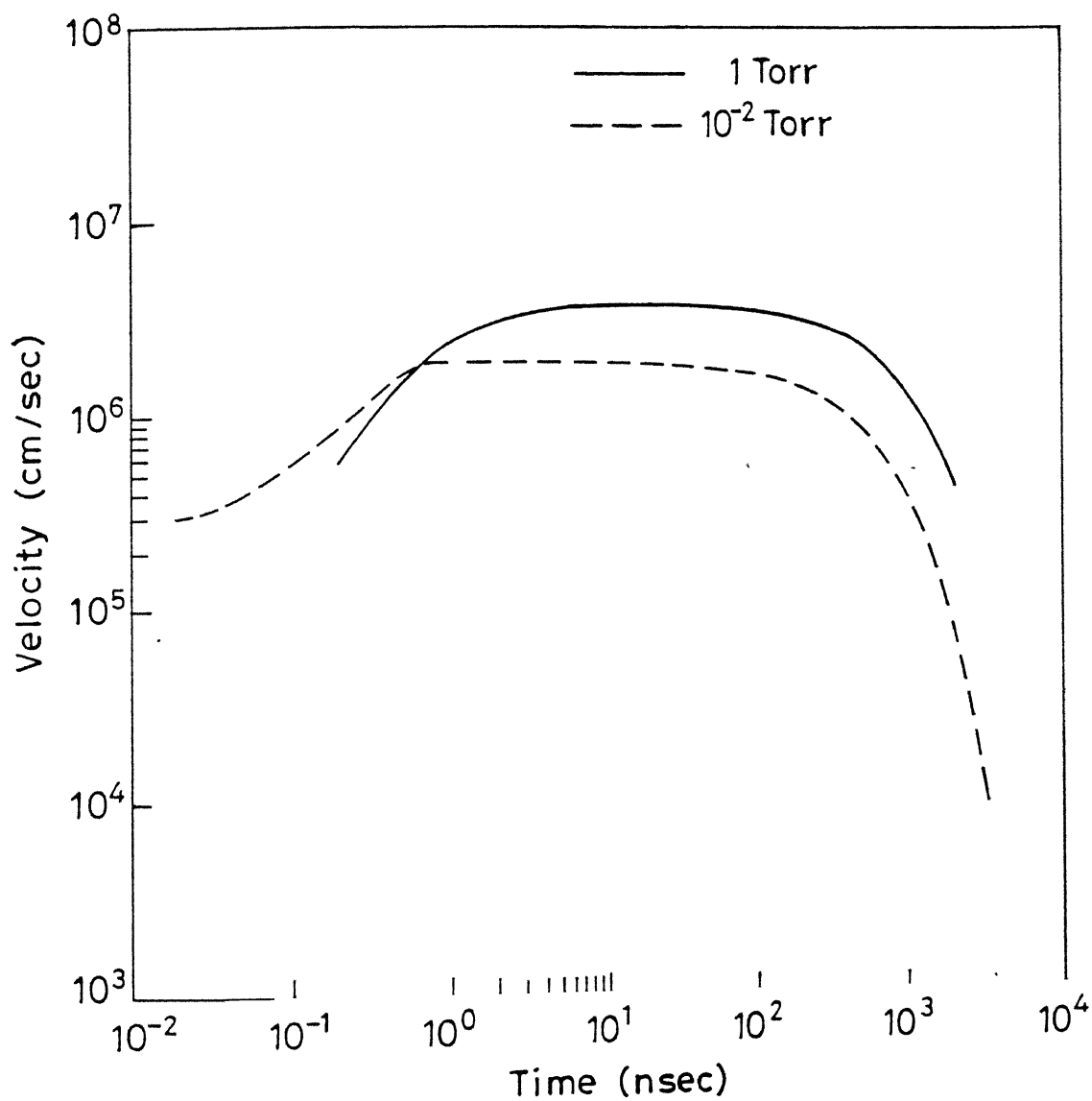


Fig. 15. Dependence of the velocity of the plasma on time in presence of argon gas.

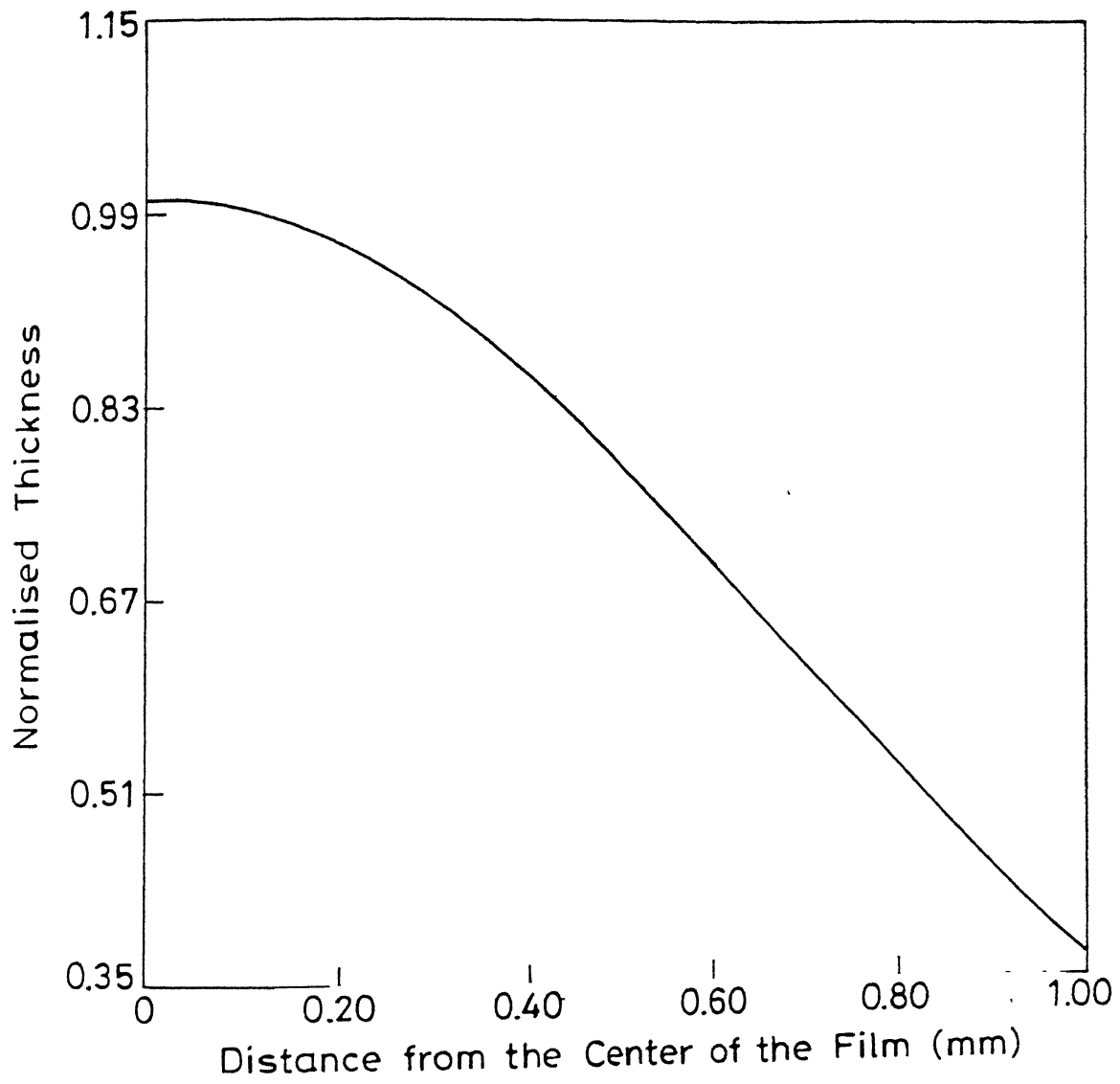


Fig. 16. Variation of the film thickness with distance from the center of the film.

## CHAPTER IV

# DIAGNOSTICS OF LASER ABLATED PLUMES FOR LASER ABLATION DEPOSITION

## INTRODUCTION

Pulsed laser induced ablation or vaporization from material surfaces has been a subject of immense interest for quite some time in view of its importance in the context of understanding the nature of laser-solid interactions.<sup>264-267</sup> As has already been said in chapter II, the characteristics of laser ablated plasmas depend on several factors such as the wavelength and energy of the laser used, presence of ambient gas and the properties of target material.<sup>23,239</sup> Several reports have appeared in the literature on the theoretical and experimental investigations of the interaction of laser produced plasma with the ambient gas.<sup>74,75,252-254,268-272</sup> The large efforts are being made to characterize the ablation process and to unravel its basic aspects for thin film deposition through the development of suitable diagnostic tools. Various diagnostics employed are listed in Table 1, Chapter II.

In the present chapter, an extensive work on the diagnostics developed, optical emission diagnostics and ion probe measurements, to study the laser ablated carbon plasma is presented.<sup>85,113,174,175</sup> The detailed analysis of the composition of the plasma, the dynamics of plume evolution and the variation of plasma parameters may be helpful in understanding the LAD process as well as the deposited films. We have used optical emission diagnostics to monitor the spatial and temporal variation of molecular clusters, neutral and ionic species within the plume at various laser irradiances, laser wavelength and ambient gas pressures. Langmuir probe is used to get local information on the plasma conditions at various distances from the target surface and angular positions with respect to target surface normal (TSN) at various argon gas pressures.<sup>85</sup>

## EXPERIMENTAL SET UP

CENTRAL LIBRARY  
113  
No. A 125662

The experimental setup used for optical emission diagnostics is similar to the one shown in figure 5. A Nd:YAG laser ( $\lambda = 1.064, 0.532, 0.355$  and  $0.266 \mu\text{m}$ ) was focused

onto a continuously rotating spectroscopic grade pure graphite target rod, the focused spot on target being 260  $\mu\text{m}$ . Experiments were carried out at various ambient gas pressures in the range  $10^{-3}$  - 100 Torr. The instrumental broadening of the detection system was measured by monitoring the line of a He-Ne laser at 632.8 nm for the minimum slit width used in the experiment. It was found to be much smaller than the width of the Stark broadened profiles recorded for the various transitions. The temporal profiles of the selected transitions were also recorded using a monochromator and the data acquisition system, already described in chapter II.

The details of ion probe diagnostics have also been discussed in chapter II, figure 6. The third harmonic of Nd:YAG laser was focused onto the graphite target mounted in the vacuum chamber. The space and angle resolved studies of the laser ablated carbon plume were performed at various argon gas pressures from  $10^{-3}$  - 100 Torr. The digitized ion probe signals were fed to the PC for further data processing. The experiment was repeated several times to ensure the reproducibility of the data.

## **RESULTS OF THE IN-SITU DIAGNOSTICS AND DISCUSSION**

### **1. Optical Emission Diagnostics at High Laser Irradiance ( $\sim 10^9$ - $10^{12}$ W/cm<sup>2</sup>)**

Emission spectra of laser ablated carbon plume was recorded at both low and high irradiances in presence of argon and helium gas pressures from  $10^{-3}$  to 100 Torr at various distances (z) away and parallel to the target surface. The emission spectra were recorded by moving the monochromator in the horizontal plane in direction perpendicular to the expanding plume direction at various laser intensities and laser wavelengths. The plasma emission from the target at higher laser irradiances was found to be dominated by various atomic/ionic species irrespective of laser wavelength. A typical emission spectrum of the carbon plasma in vacuum (better than  $10^{-4}$  Torr) recorded at 2 mm away and parallel to the target surface using 100 mJ energy of 0.355  $\mu\text{m}$  laser wavelength is shown in figure 17. The laser irradiance was calculated using irradiated focal spot (260  $\mu\text{m}$ ) and the laser pulse width (5 ns). The emission lines were identified from the available literature.<sup>206</sup> Various transitions from C IV to C I are observed in the emission spectrum.

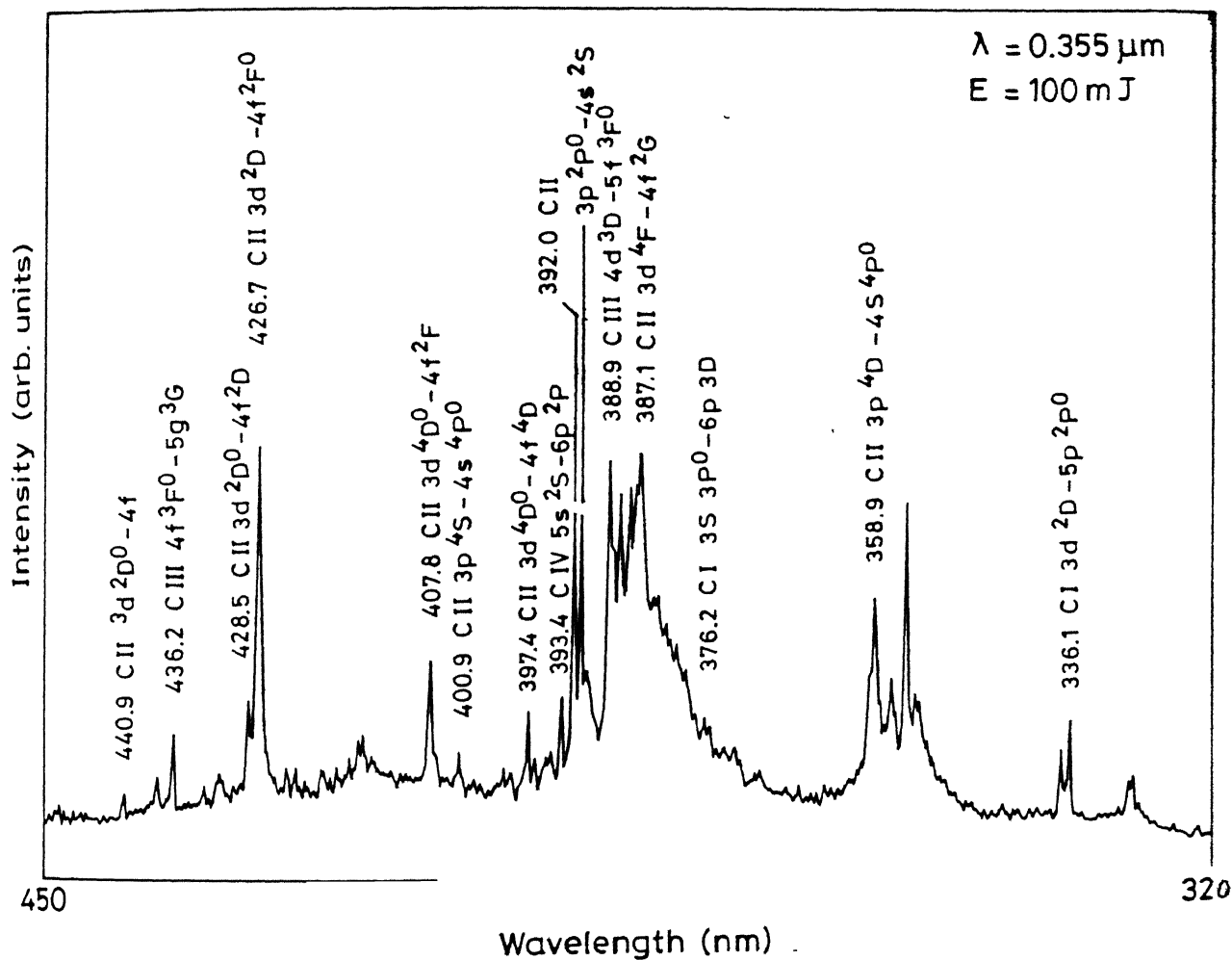


Fig. 17. Emission spectrum of the laser ablated carbon plume at 100 mJ of 0.355  $\mu\text{m}$  laser radiation recorded at a distance of 2 mm from the target surface in vacuum in the wavelength range 320–450 nm.

The relative intensity of the plume was found to be sensitive to a range of experimental parameters, particularly laser fluence, distance from the target surface and ambient gas pressure. The presence of ambient gas has a strong influence on the plume properties such as change of colour and reduction of plume length. The apparent size of the plume as seen visually was about 15 mm in vacuum and reduced to about 3 mm at 100 Torr of argon gas pressure. To see the effect of argon gas on laser generated plume, the emission spectra were recorded at various distances away and parallel to the target surface. The emission corresponding to the C II transition  $3p^2P^0 - 4s^2S$  at 392.0 nm and C III transition  $4f^3F^0 - 5g^3G$  at 436.2 nm are chosen to study the effect of background gas. Every point in the figures to follow is an average of five observations. Figure 18 shows the emission intensity for the transitions as a function of distance from the target surface in vacuum and 1 Torr argon gas pressure. It is observed that the intensity of the lines increases drastically in the presence of 1 Torr argon gas pressure. The line emission enhancement can be attributed to various interaction processes like collisional excitation, charge transfer and recombination processes etc. Our results can be qualitatively explained on the basis of recombination which occur either due to radiative or the three body recombination (TBR) process. The functional dependence of recombination rate for radiative and TBR can respectively be expressed as  $n_e n_i \bar{Z}^2 T_e^{-3/4}$  and  $n_e^2 n_i \bar{Z}^3 T_e^{-9/2} \ln(\sqrt{\bar{Z}^2 + 1})$  where  $\bar{Z}$ ,  $n_e$  and  $T_e$  represent the ion charge, electron density and electron temperature, respectively.<sup>273</sup> It can be seen that the radiative process is important only close to the target surface whereas TBR is a dominant process beyond a few mm from the target surface. The background gas basically provides a heat sink so that the recombination can continue for a longer period. Also, the excitation of molecules of background gas results in reducing the electron energy, increasing collisional cooling, which in turn increases TBR rate. This results in populating the excited neutral and ionic carbon species in presence of a background gas. The intensity of both the transitions decreased with increase in distance from the target surface. However, the decrease in intensity is found to be faster in presence of argon gas. In vacuum the plasma expands freely, however, it is confined to a small region in presence of background gas which results in reduced expansion rate and hence enhanced cooling rate. Similar results have been reported for excimer laser<sup>75</sup> and nitrogen laser<sup>274</sup> ablated plasmas. The results<sup>175</sup> obtained using 0.532  $\mu\text{m}$  laser wavelength showed the similar behavior in the intensity of the spectral lines with distance from the target surface and argon gas pressure.

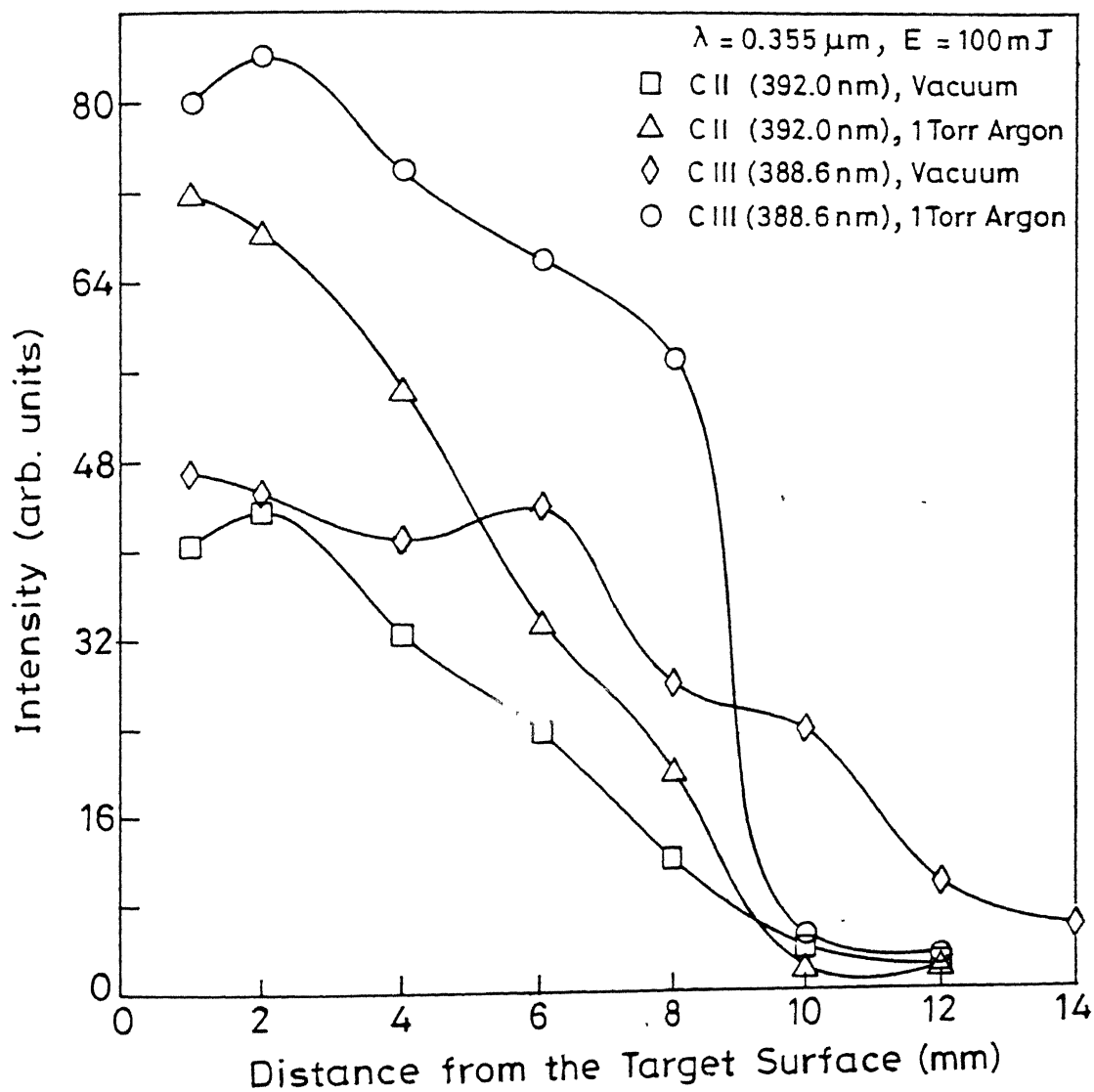


Fig. 18. Dependence of the intensity of C II transition at 392.0 nm and C III transition at 388.6 nm on distance from the target surface in vacuum and 1 Torr argon gas pressure using 100 mJ of 0.355  $\mu\text{m}$  laser wavelength.



Temporal profiles of various transitions were recorded at different distances away and parallel to the target surface. Figure 19 shows the variation in the peak intensity maxima for C II transition  $3p^2P^0 - 4s^2S$  at 392.0 nm in vacuum and 1 Torr argon gas. The velocity of the plasma front was estimated using the slope of the curve. The estimated velocity of C II species is  $1.2 \times 10^5$  and  $1.95 \times 10^4$  cm/sec in vacuum and 1 Torr argon gas respectively. The velocity decreased in presence of argon gas probably because of the energy transfer from the species to the ambient gas.

The electron temperature was estimated using intensities of various C II species. Figure 20 shows a typical plot of  $[\ln(I_s'' \lambda'' g' A' / I_s' \lambda' g'' A'')]$  versus  $E' - E''$  for 100 mJ of 0.355  $\mu\text{m}$  laser wavelength at a distance of 2 mm from the target surface in vacuum. The slope of the curve gives the electron temperature of 4.4 eV. The variation of electron temperature with distance from the target surface in vacuum and 1 Torr argon gas is shown in figure 21. Electron temperature is found to be larger in presence of argon gas. The electron temperature decreases with increase in distance from the target surface.

The electron density of the plasma was determined from the Stark broadening of selected species. We have used the C II transition  $3p^2P^0 - 4s^2S$  at 392.0 nm for estimating the electron density. Figure 22 shows a typical Stark broadened profile of C II transition at 392.0 nm at a distance of 10 mm from the target surface in vacuum. The electron density was calculated using Eq. (5). Figure 23 shows the variation of the electron density with distance from the target surface in vacuum and 1 Torr argon. The electron densities at various distances increased in the presence of ambient gas. The dependence of electron density with distance from the target surface showed  $z^{-0.24}$  and  $z^{-0.87}$  dependence in vacuum and 1 Torr argon gas respectively.

## II. Optical Emission Diagnostics at Low Laser Irradiance ( $\sim 10^8 - 10^9 \text{ W/cm}^2$ )

At low laser irradiance the spectrum was found to be dominated by  $C_2$  species. Molecular  $C_2$  has been claimed as a critical species for the diamond like carbon and hence the study of  $C_2$  is very helpful in understanding characteristics of the deposited films. Figure 24 show the emission spectrum of carbon plasma in vacuum at  $3.6 \times 10^8 \text{ W/cm}^2$  of laser intensity using 1.06  $\mu\text{m}$  laser wavelength. The spectra was recorded at a distance of 3 mm from the target surface in the wavelength range 415-620 nm. The spectrum is dominated by

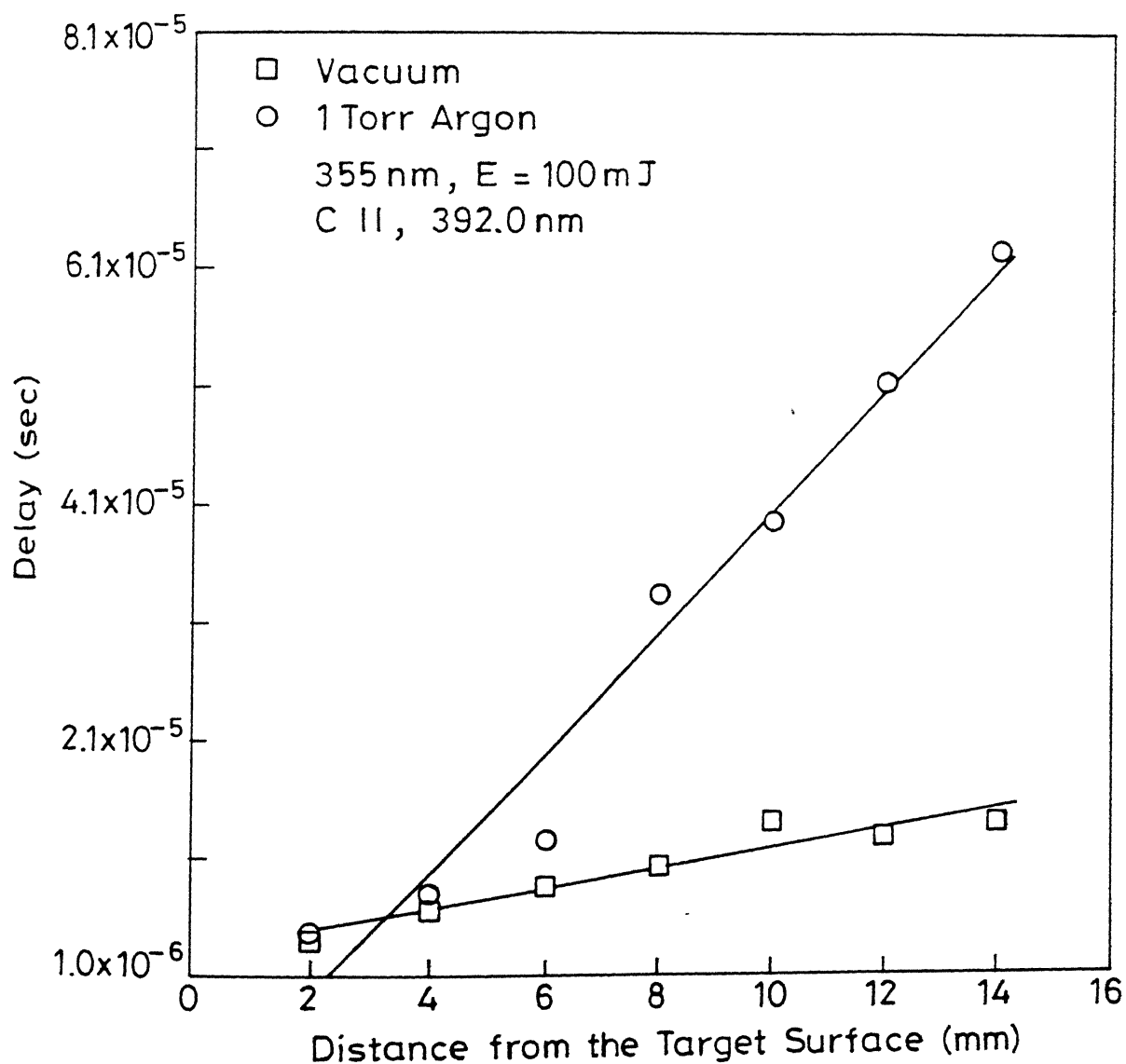


Fig. 19. Variation of the time delay in the peak intensity maxima of C II transition ( $3p \ ^2P^0 - 4s \ ^2S$ ) at 392.0 nm with distance from the target surface at 100 mJ of 0.355  $\mu\text{m}$  laser radiation in vacuum and 1 Torr argon.

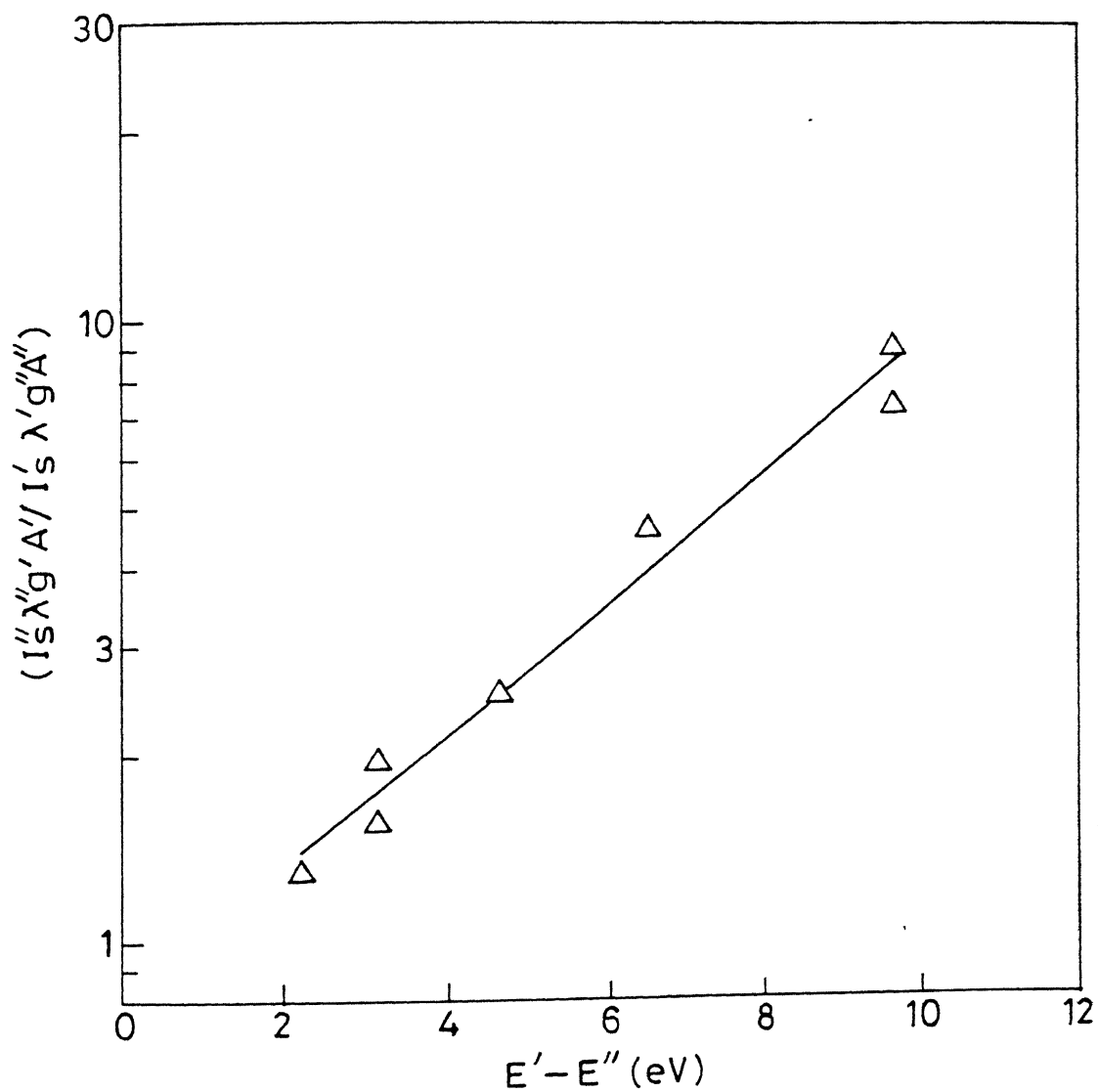


Fig. 20. Typical plot of  $\ln [(I_s'' \lambda'' g' A' / I_s' \lambda' g'' A'')]$  versus  $E' - E''$  for C II species at 2 mm distance from the target surface in vacuum.

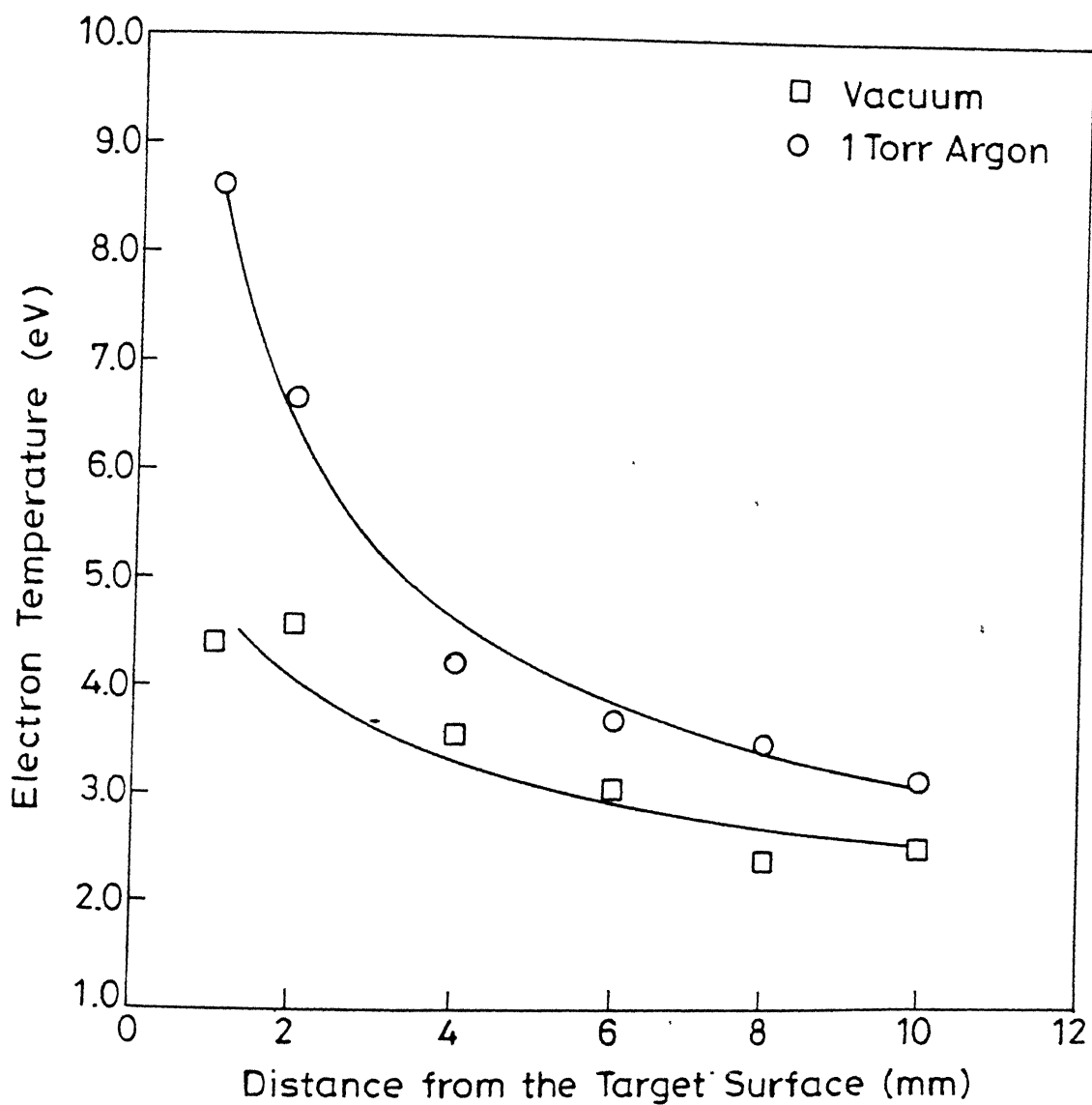


Fig. 21. Variation of electron temperature with distance from the target surface using 100 mJ laser energy of  $0.355 \mu\text{m}$  radiation in vacuum and 1 Torr argon.

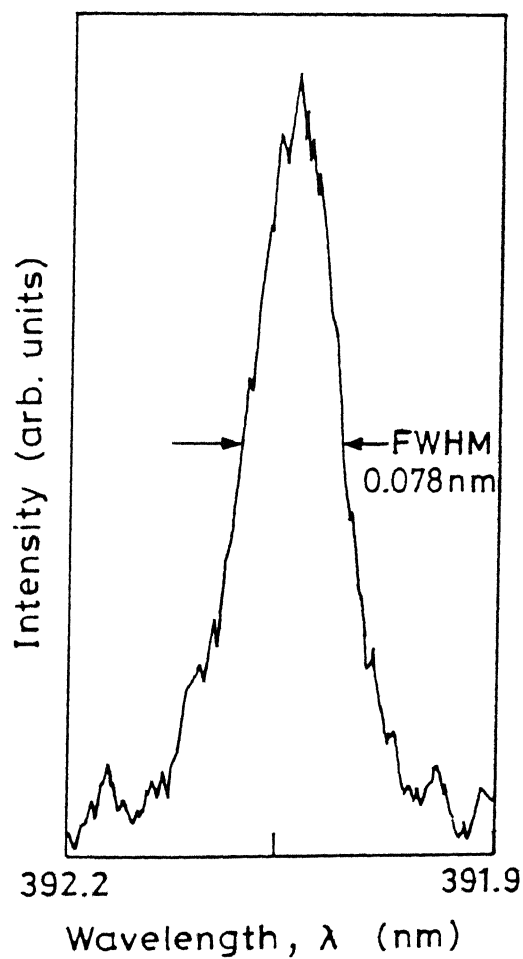


Fig. 22. Typical Stark broadened profile of C II transition  $3p\ ^2P^0 - 4s\ ^2S$  at 392.0 nm in vacuum at a distance of 10 mm using 100 mJ of 0.355  $\mu\text{m}$  laser wavelength.

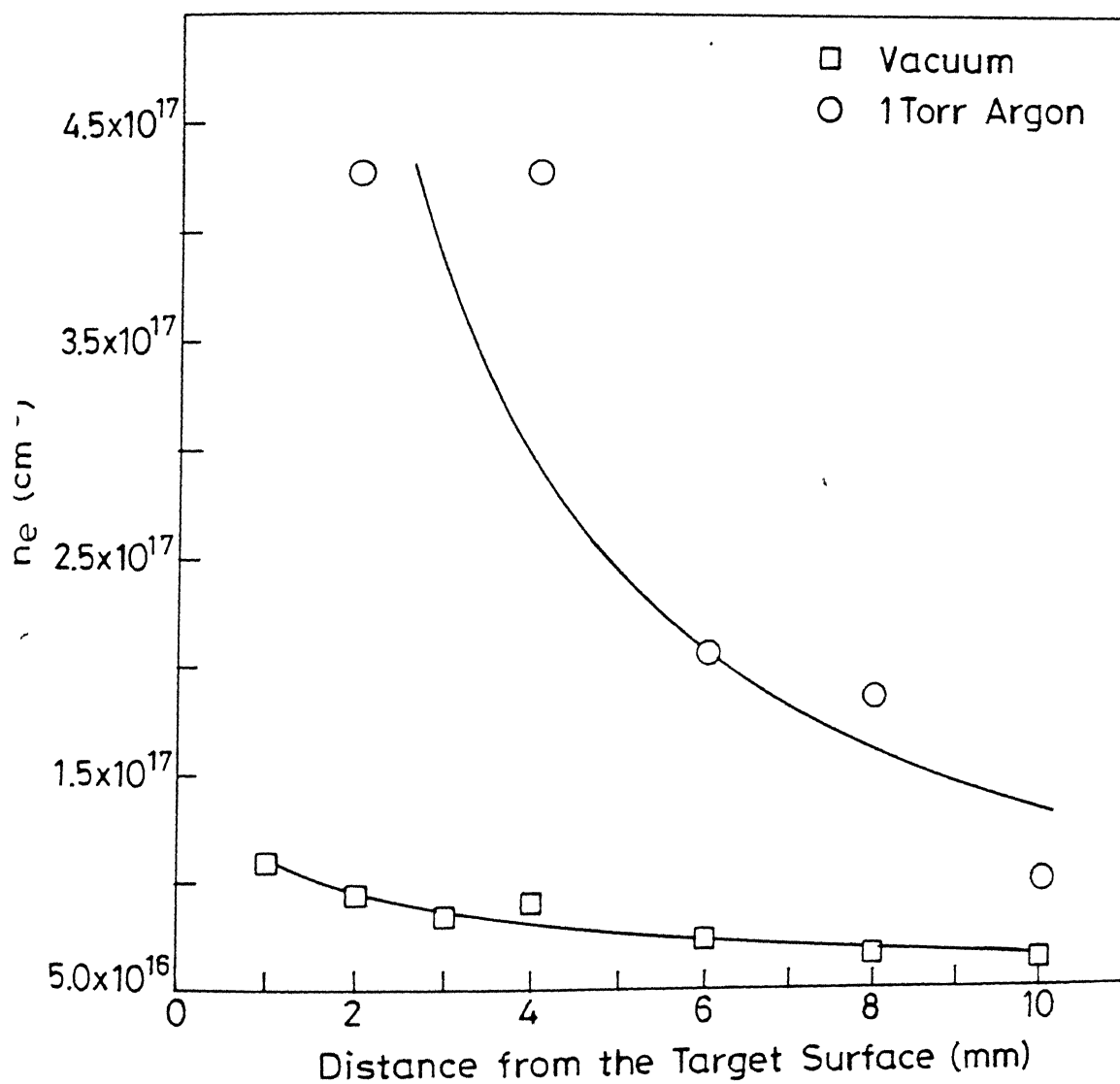


Fig. 23. Variation of electron density of C II transition  $3p\ ^2P^0 - 4s\ ^2S$  at 392.0 nm as a function of distance from the target in vacuum and 1 Torr argon.

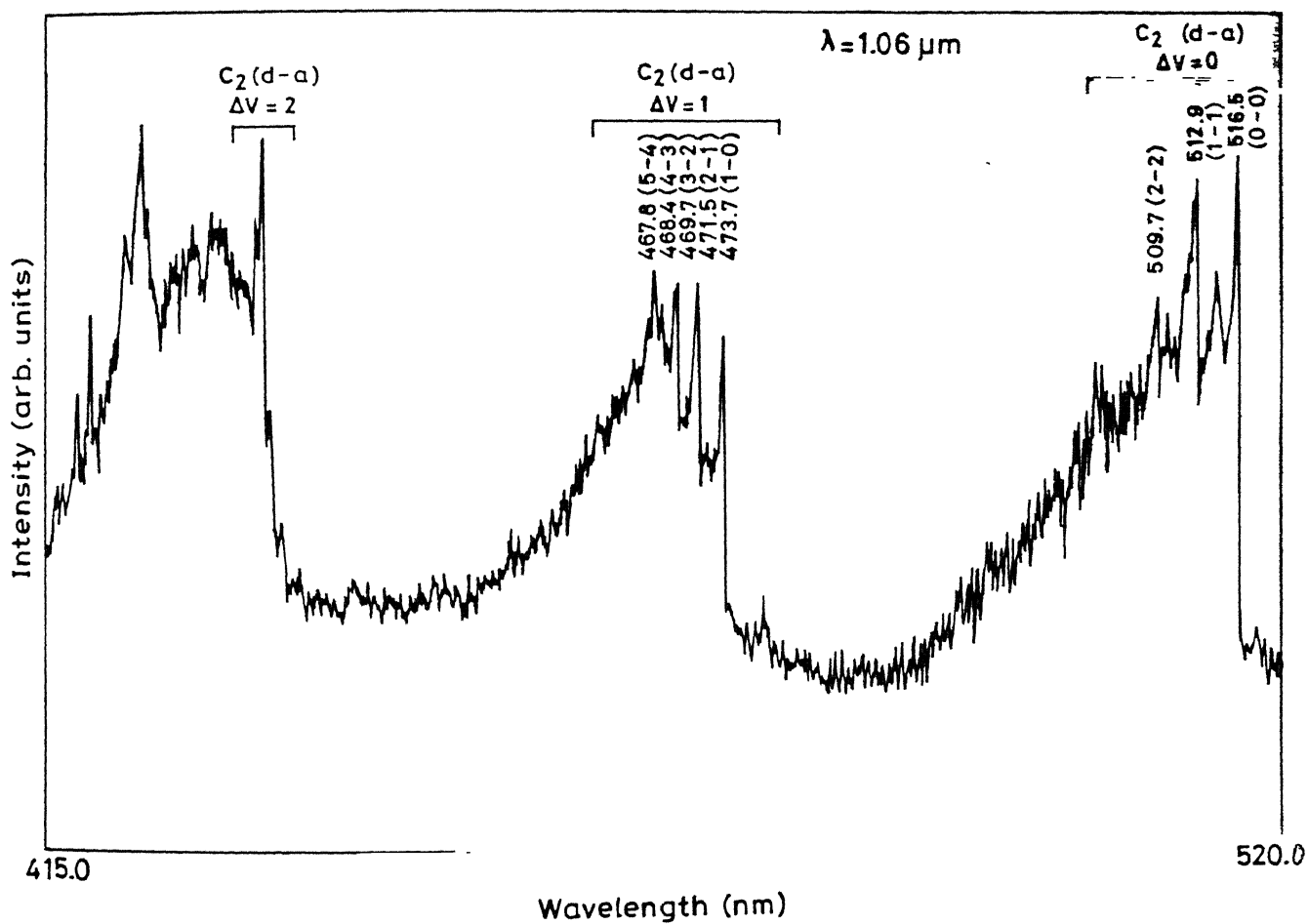


Fig. 24. Emission spectrum of the carbon plasma in vacuum at  $3.6 \times 10^8 \text{ W/cm}^2$  of  $1.06 \mu\text{m}$  laser radiation ;  
 (a) Spectrum range 415 - 520 nm

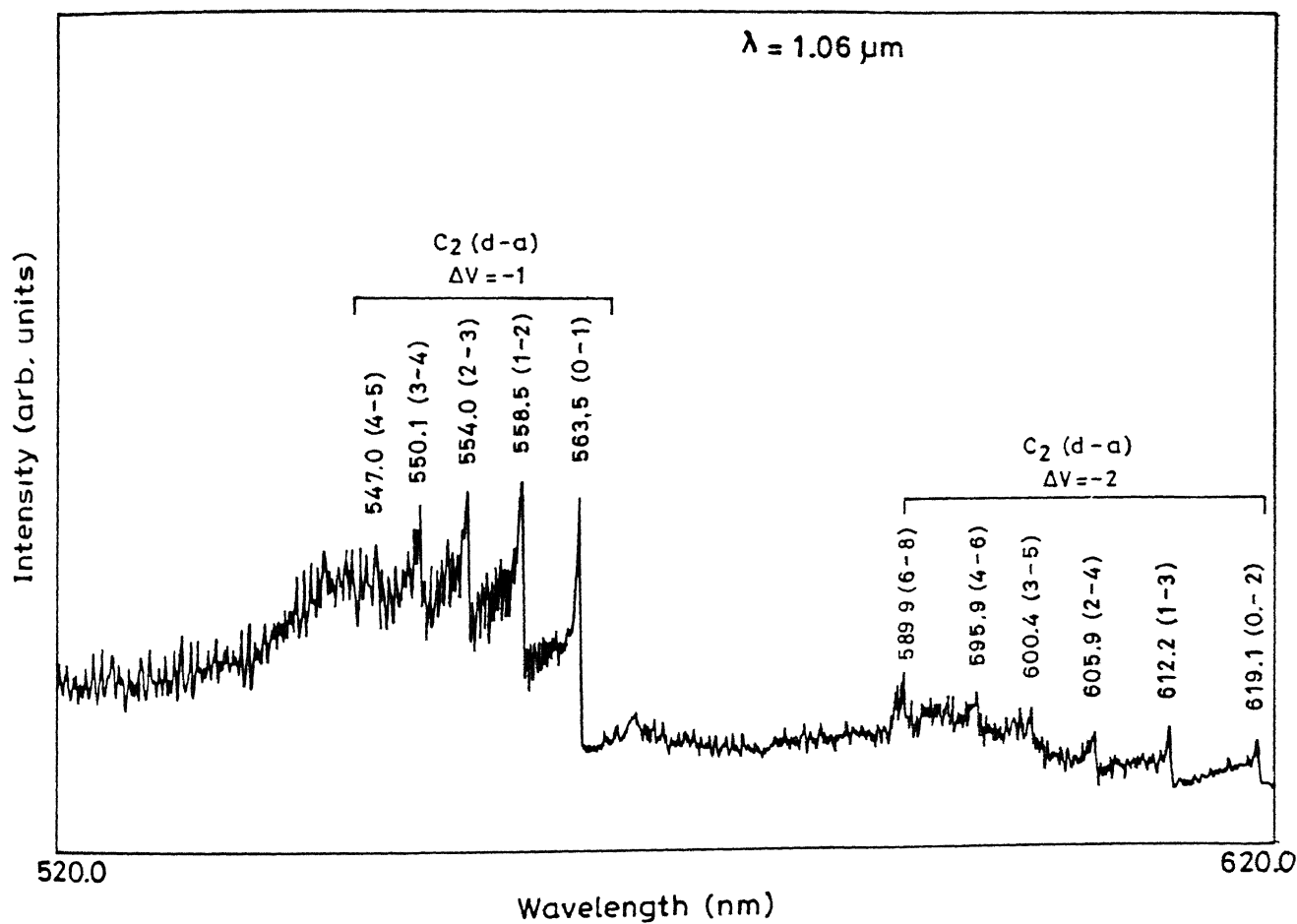


Fig. 24. Emission spectrum of the carbon plasma in vacuum at  $3.6 \times 10^8 \text{ W/cm}^2$  of  $1.06 \mu\text{m}$  laser radiation ;  
 (b) Spectrum range 520 - 620 nm.



$C_2$  emission in the  $\Delta v = -2, -1, 0, +1, +2$  sequence of the Swan ( $d^3\pi_g - a^3\pi_u$ ) bands and  $\Delta v = 0$  and  $+1$  sequence of the Deslandres - d'Azambuja ( $C^1\pi_g - A^1\pi_g$ ) bands.<sup>121</sup> No cometary bands at 405 nm were seen with or without argon gas in our experiment, though, few C I and C II lines were present in addition to molecular  $C_2$  bands. All the  $C_2$  Swan bands have been recorded which include  $\Delta v = -2, -1, 0, +1, +2$  where  $\Delta v = v' - v''$  is the difference of the vibrational quantum number between the upper ( $v'$ ) and lower ( $v''$ ) states of transition. The  $C_2$  d-a  $\Delta v = 0$  Swan band sequence in vacuum consisted of Swan band heads (0-0) at 516.5 nm, (1-1) at 512.9 nm and (2-2) at 509.7 nm only, while for  $\Delta v = 1$ , the bands (1-0) at 473.7 nm, (2-1) at 471.5 nm, (3-2) at 469.7 nm, (4-3) at 468.4 nm and (5-4) at 467.8 nm are found to be prominent. We also observed the  $\Delta v = -2$  Swan band sequence with the Swan band heads of (0-2) at 619.1 nm, (1-3) at 612.2 nm, (2-4) at 605.9 nm, (3-5) at 600.4 nm and (4-6) at 595.9 nm. The intensity of band heads increased with increase in ambient gas pressure and decrease in laser wavelength. The emission spectra obtained resemble those observed during laser ablation of graphite using KrF (248 nm) excimer laser.<sup>114</sup> The only difference is that we observed a few ionic lines at a relatively low irradiance level. The appearance of the  $C_2$  bands at such low irradiance suggests that they are probably formed from atomic carbon recombination or due to electron impact excitation of ground state  $C_2$  molecules emitted directly from the target or formed from the fragmentation of higher clusters in the plasma.

To study the incident laser wavelength dependence, emission spectra of  $C_2$   $\Delta v = -1$  Swan band sequence were recorded in presence of helium and argon gas pressures at various laser energies using 1.06, 0.532, 0.355 and 0.266  $\mu\text{m}$  laser wavelengths.<sup>113</sup> The spectra were recorded at various distances from the target. The intensity of the band heads increased upto a distance of 3 mm from the target surface and then decreased very rapidly beyond this distance. Every point in the figures to follow is an average of five observations. Figures 25 and 26 show the emission spectra of  $C_2$   $\Delta v = -1$  Swan band sequence for 1.06  $\mu\text{m}$  laser wavelength at  $10^{-3}$  and  $10^{-1}$  Torr of argon gas at 22, 33, 44 and 66 mJ of laser energies, the corresponding irradiances being 2.4, 3.6, 4.8 and  $6.0 \times 10^8 \text{ W/cm}^2$  respectively. It is observed that the intensity of band heads first increases with energy, attains a maximum value and then decreases. Similar variation in  $C_2$  emission intensity with laser energy was observed using 0.532 and 0.355  $\mu\text{m}$  laser wavelengths. Figure 27 shows the intensity of  $C_2$  Swan band heads of ( $v' - v''$ ) i.e. (0-1) at 563.5 nm and (1-2) at 558.5 nm for 0.532 and 0.355  $\mu\text{m}$  laser wavelengths at  $10^{-1}$  Torr of argon gas, recorded at a distance of 3 mm away and

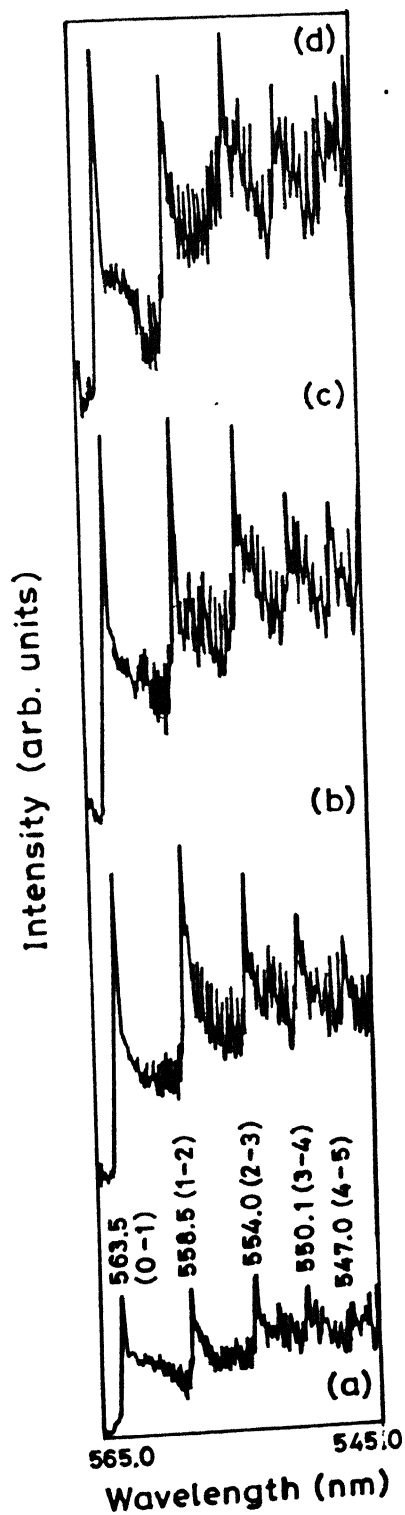


Fig. 25. C<sub>2</sub> d-a Swan band sequence  $\Delta v = -1$  at  $10^{-3}$  Torr of argon gas pressures at (a) 22 mJ, (b) 33 mJ, (c) 44 mJ and (d) 66 mJ of laser energy.

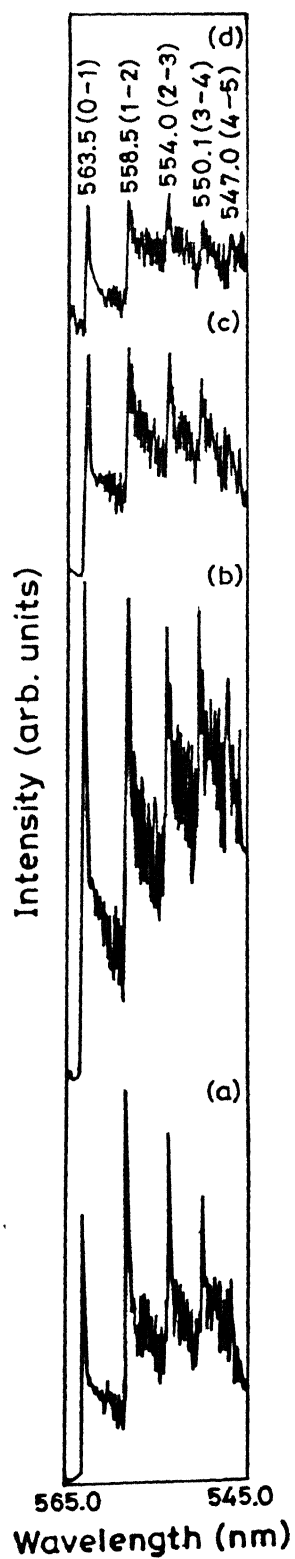


Fig. 26.  $C_2$  d-a Swan band sequence  $\Delta v = -1$  at  $10^{-1}$  Torr of argon gas pressures at (a) 22 mJ, (b) 33 mJ, (c) 44 mJ and (d) 66 mJ of laser energy.

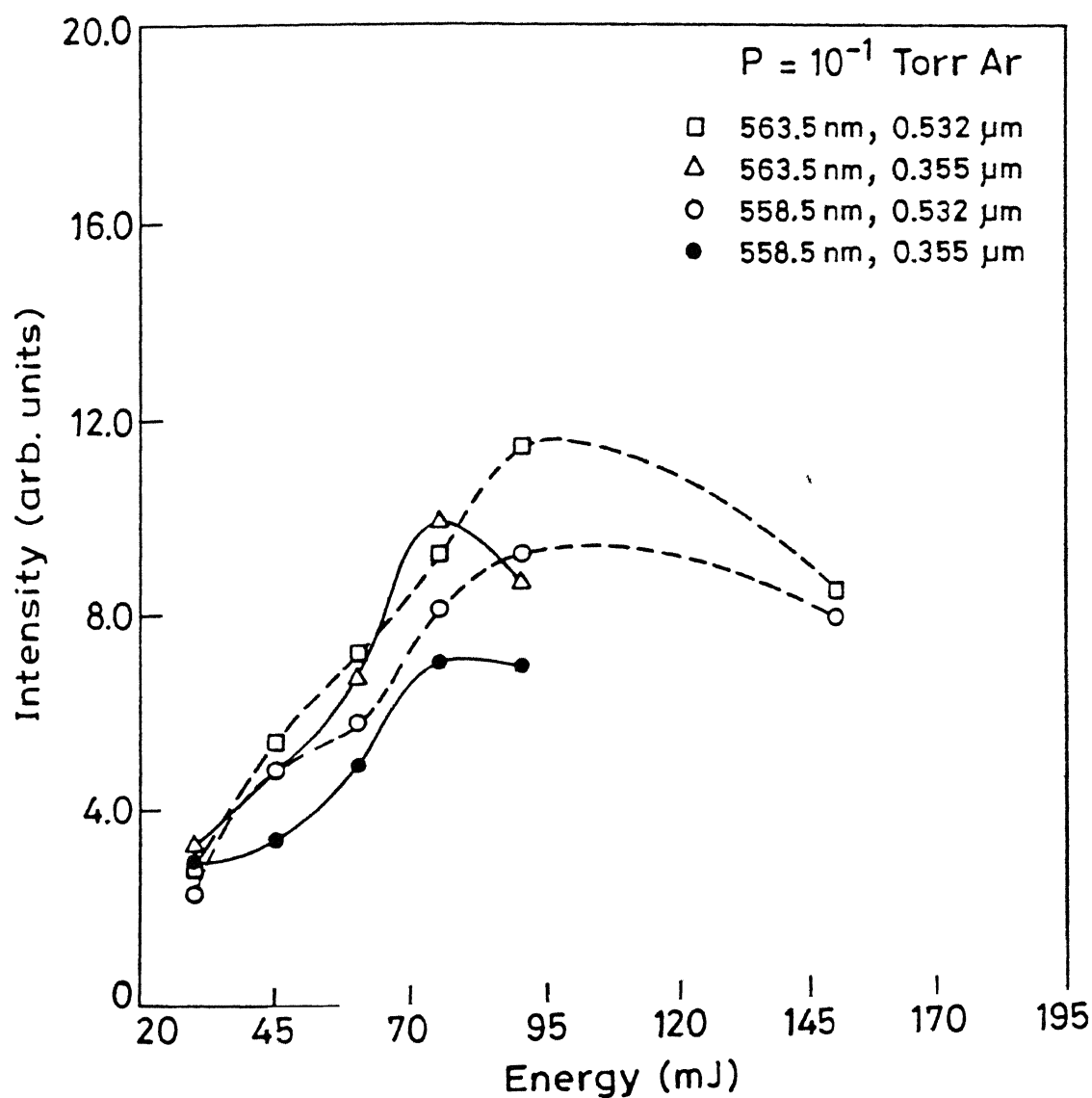


Fig. 27. Intensity of  $\text{C}_2$  Swan band heads (0-1) at 563.5 nm and (1-2) at 558.5 nm at various laser energies of 0.532 and 0.355  $\mu\text{m}$  laser wavelength at  $10^{-1}$  Torr argon gas pressure.

parallel to the target surface. For all the wavelengths, the intensity peaks at some intermediate energy. Also the peak intensity maximum shifts towards low energies with decrease in wavelength which may be due to the photo fragmentation of higher clusters in ablated plume.

To see the effect of ambient gas on molecular  $C_2$  emission, emission spectra of  $C_2$  Swan bands was recorded at various argon gas pressures at different laser energies. Figure 28 shows the  $C_2$  Swan band spectra at  $10^{-1}$ , 1 and 10 Torr of argon gas pressures at 33 mJ of 1.06  $\mu\text{m}$  laser wavelength, recorded at a distance of 3 mm from the target surface. The intensity of bands increased as the pressure of the argon gas increased from  $10^{-3}$  to 100 Torr. Thus the incorporation of the ambient gas helps to cool the molecular species and increase the recombination rate. Figure 29 shows the variation in intensity of Swan band head i.e. (0-1) at 563.5 nm for 1.06, 0.532 and 0.355  $\mu\text{m}$  laser wavelengths in pressure range of  $10^{-3}$  to 100 Torr of argon gas, recorded at 3 mm from the target surface. The intensity increases with pressure for all the laser wavelengths. The observed intensity of the band is largest at 0.355  $\mu\text{m}$  at all pressures. This probably is due to a change in optical penetration depth which decreases with wavelength. The decreased volume of the material with which the laser can interact results in a more effective coupling to the target.

The dependence of  $C_2$  band heads intensity with laser energy and ambient pressure showed almost the similar behavior in presence of helium. It was found that, for all the laser wavelengths there is an optimum energy at which the intensity of  $C_2$  bands is maximum.<sup>113</sup> However, the intensity of  $C_2$  bands at a particular energy increased with increase in helium gas pressure upto  $10^{-1}$  Torr and no significant change was noticed after that pressure.

The plume emission was also found to be strongly dependent on the choice of the ambient gas. Figure 30 shows the emission spectrum of  $C_2$   $\Delta v = -1$  Swan band sequence with 10 Torr of helium and argon gas at a laser energy of 45 mJ with 0.355  $\mu\text{m}$  laser wavelength. It can be seen from the figure that the enhancement is more pronounced in presence of argon. Figure 31 shows the variation in the relative intensity of  $C_2$  d-a  $\Delta v = -1$  Swan band heads at 563.5 nm (0-1) and 558.5 nm (1-2) using 0.355  $\mu\text{m}$  laser at 40 mJ of laser energy at various helium and argon gas pressures. The intensity of the band heads increased with the pressure of the ambient gas. However, the intensity in presence of argon is found more than that of helium. The difference could be the result of the effect of the mass of the ambient gas atoms. Gases of heavy atoms exert a greater opposing force on the plume

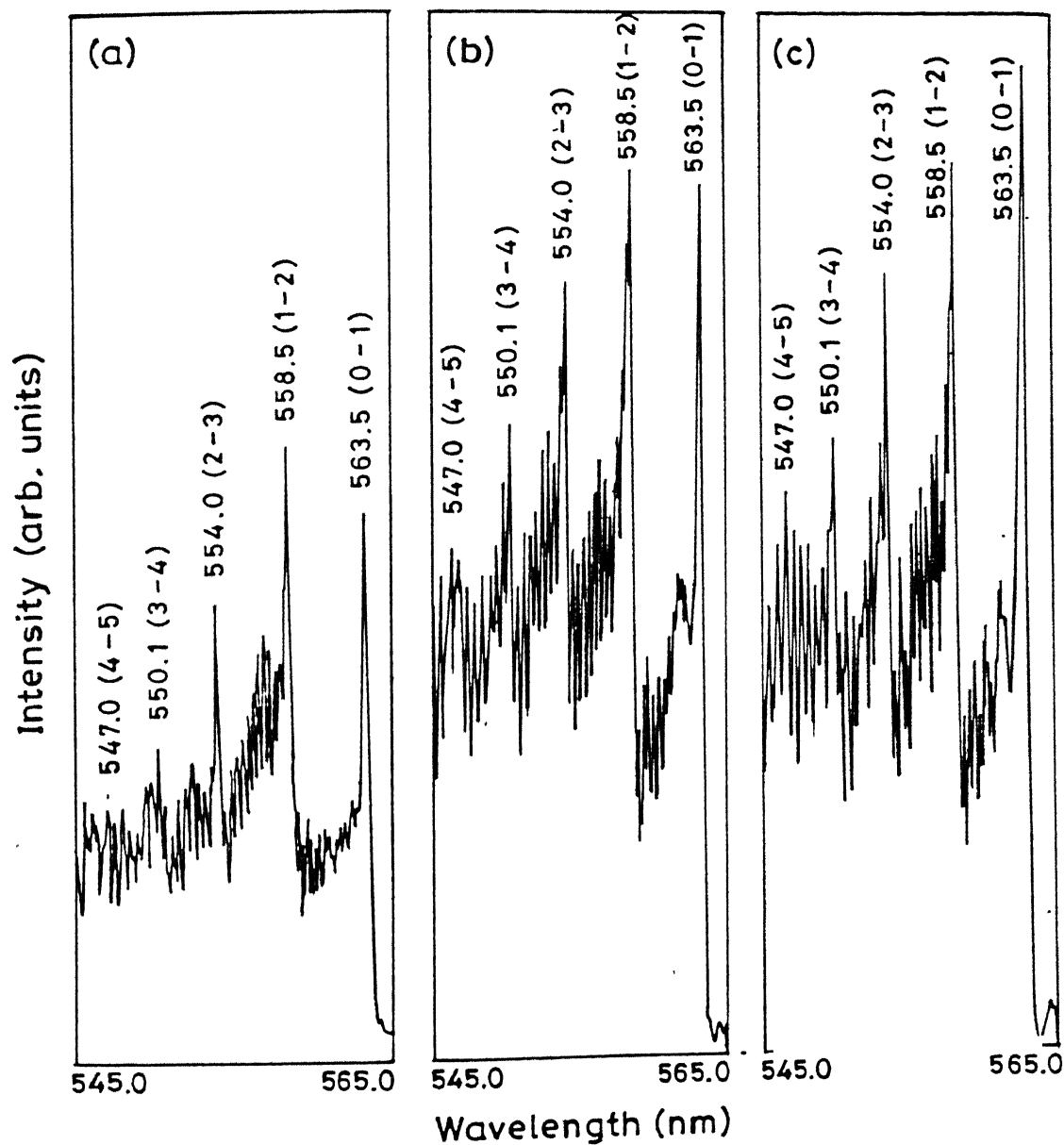


Fig. 28. C<sub>2</sub> d-a Swan band sequence  $\Delta v = -1$  at argon gas pressures of (a)  $10^{-1}$  (b) 1 and (c) 100 Torr using 1.06  $\mu\text{m}$  laser wavelength.

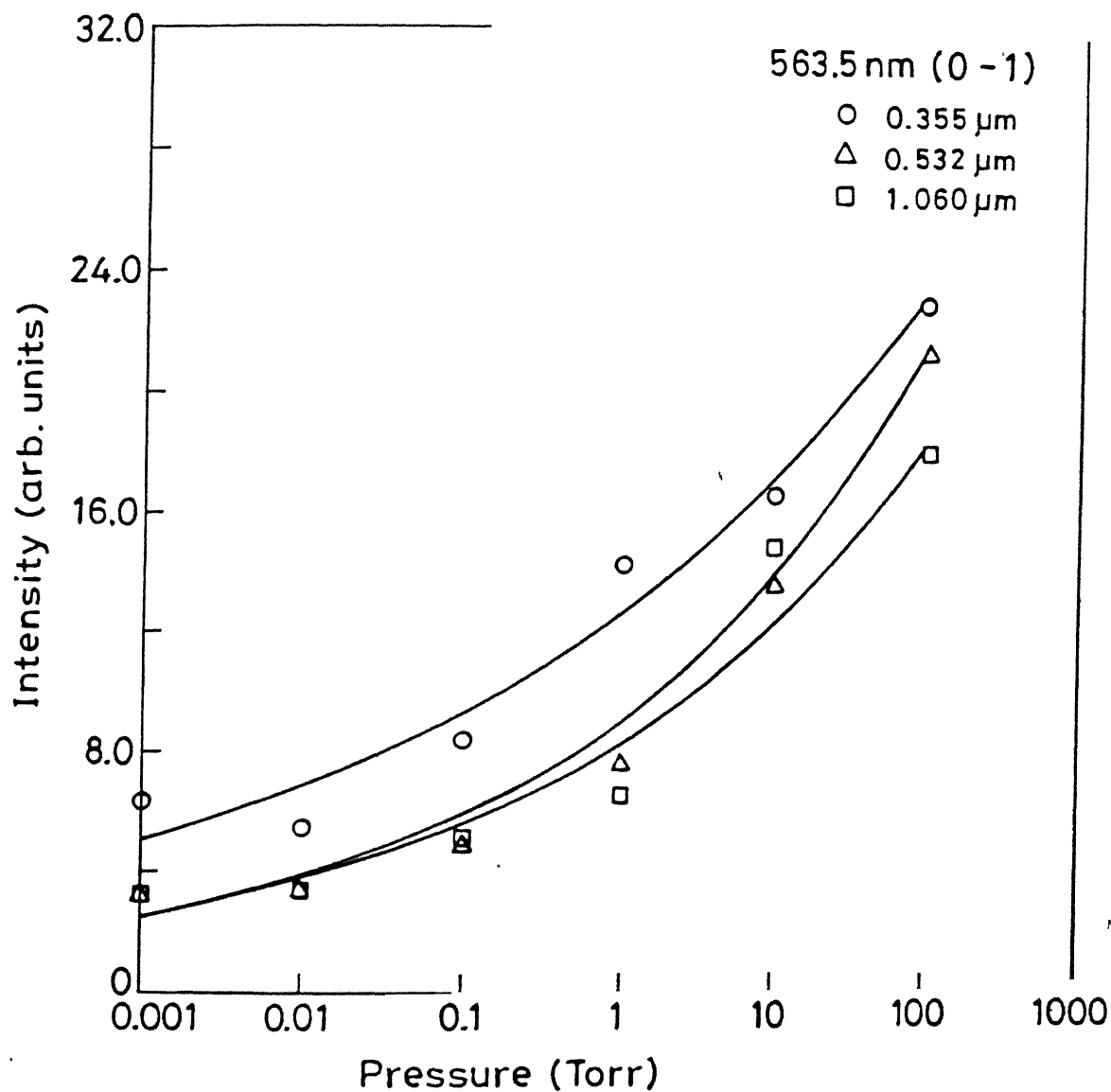


Fig. 29. Variation in intensity of Swan band head (0-1) at 563.5 nm as a function of argon gas pressure for 1.06, 0.532 and 0.355  $\mu\text{m}$  laser wavelength.

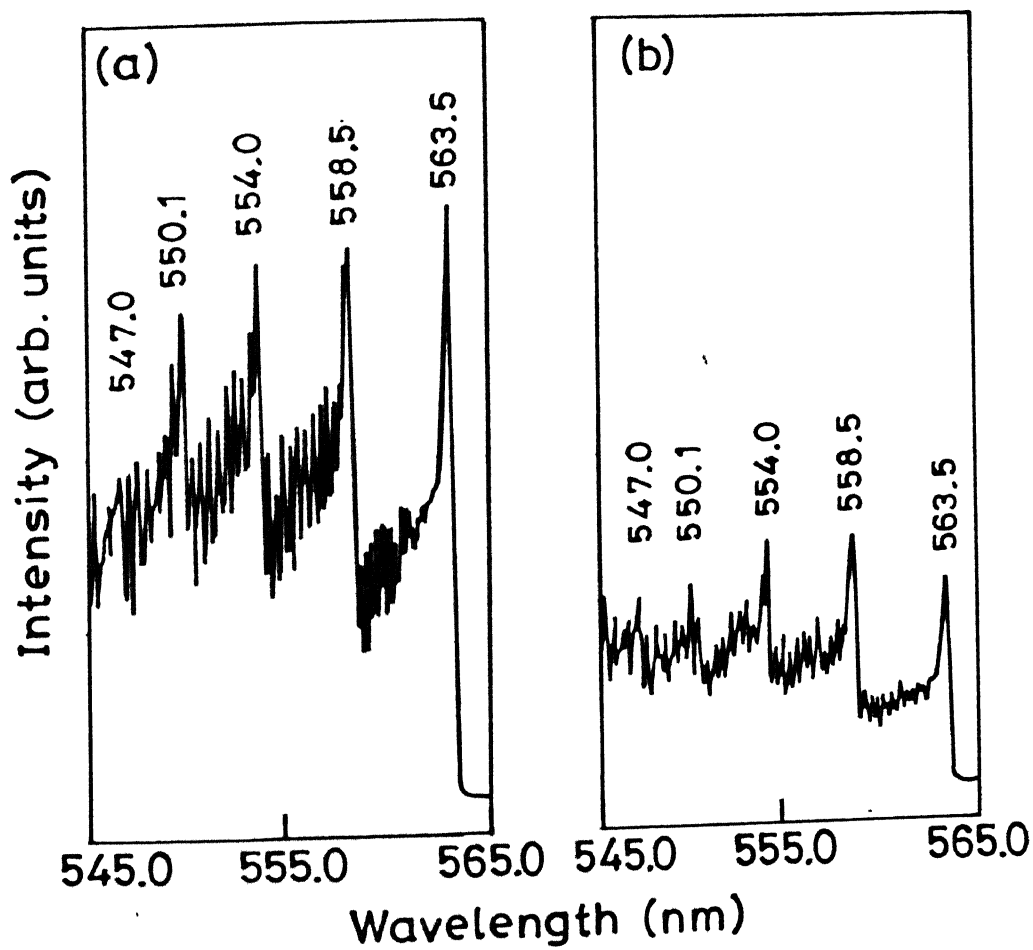


Fig. 30. C<sub>2</sub> d-a Swan band sequence at 10 Torr of (a) argon and (b) helium gas for 355 nm at 45 mJ of laser energy.



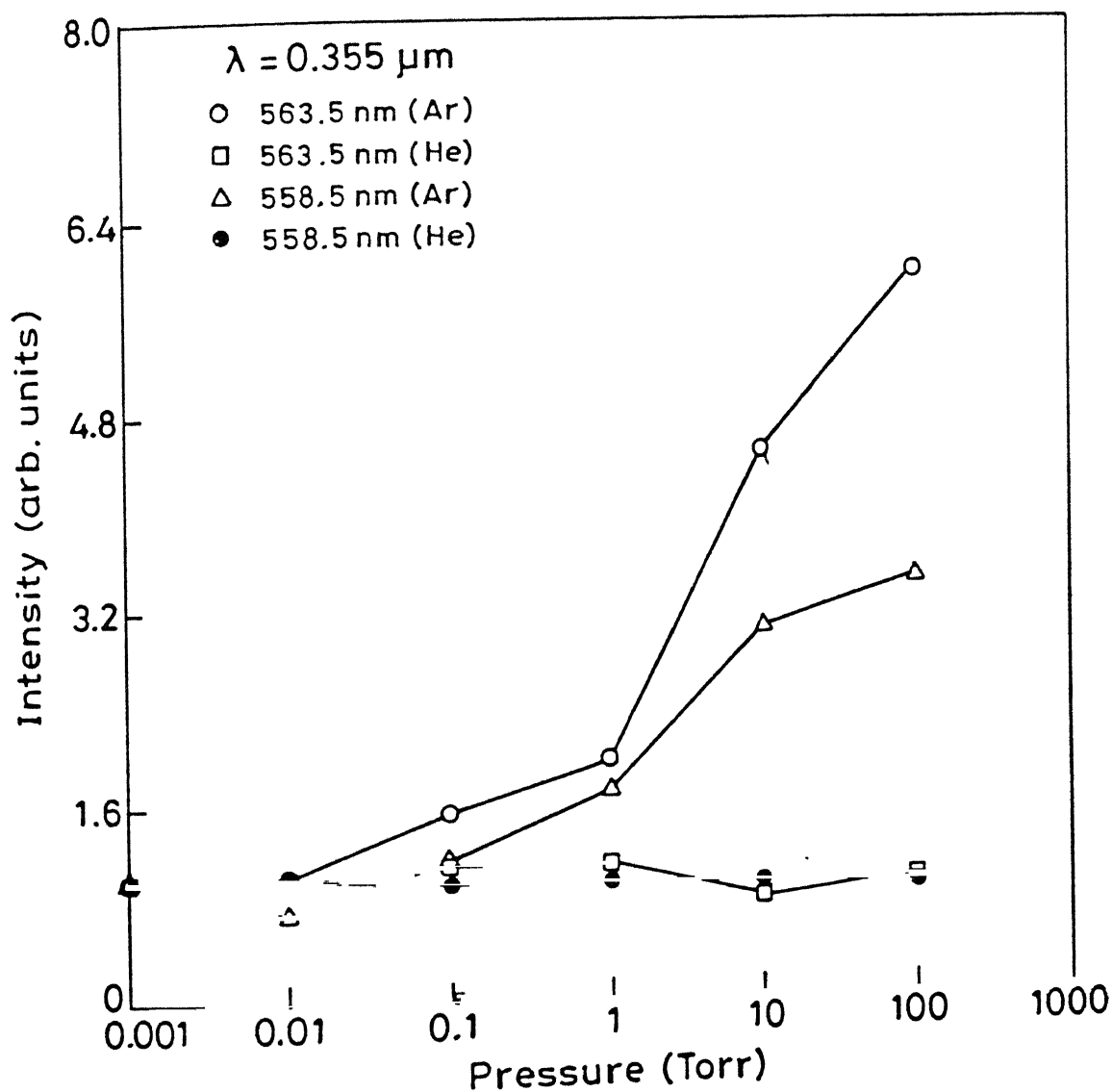


Fig. 31. Intensity of  $\text{C}_2$  Swan band heads, (0-1) at 563.5 nm and (1-2) at 558.5 nm for 0.355  $\mu\text{m}$  laser wavelength at various helium and argon gas pressures.

expansion than do the gases of light atoms. As a result, the plume maintains a different density during its movement and therefore has a different emission intensity.

It is argued by many workers that the characteristics of the deposited films are effected by the energy of the species being deposited which in turn is defined by the temperature of the species. Thus the temperature of the dominating species is a crucial parameter for defining the characteristics of the deposited films. In order to optimize the deposited film characteristics, the knowledge of the temperature of the dominant  $C_2$  species in the plume is essential. It has been shown that the properties of the DLC films can be defined in terms of  $C_2$  yield. We have calculated the vibrational temperature of the  $C_2$  species using  $C_2 \Delta v = -1$  Swan band head intensities<sup>275</sup> at various ambient pressures and laser energies using different laser wavelengths. Theoretical Franck-Condon factors<sup>209</sup> were used to get the relative population in each vibrational level using Eq. (6). A typical plot of the relative population of the upper vibrational level as derived from the measured intensities vs the vibrational quantum number for 1 Torr of argon gas pressure at 45 mJ laser energy of 0.355  $\mu m$  laser wavelength is shown in figure 32. The slope of the curve gave the vibrational temperature to be equal to 10400 K.

The vibrational temperature was calculated at different laser energies for various laser wavelengths at various helium and argon gas pressures. Figure 33 shows the variation of the vibrational temperature at  $10^{-1}$  Torr of argon gas pressure with 0.355 and 0.532  $\mu m$  laser wavelengths. The vibrational temperature is found to be maximum at an intermediate energy. It has been observed by several investigators<sup>107</sup> that the degree of diamond character in DLC films varies due to the different temperature in the laser plasma, deposition of thin film at this optimum intermediate energy may help in optimizing the film quality. It is also evident from the figure that a higher vibrational temperature is obtained for short laser wavelength laser irradiation which may be due to the small absorption depth of UV photons and to higher absorption by the ablated plasma fragments.

Figure 34 shows the dependence of vibrational temperature at various pressures of helium gas for 1.06  $\mu m$  at 60 mJ, 0.532  $\mu m$  at 40 mJ, 0.355  $\mu m$  and 0.266  $\mu m$  laser radiation at 30 mJ laser energy respectively. The increase of helium gas pressure decreased the vibrational temperature for a particular wavelength. Also, the short wavelength produced a high vibrational temperature. The vibrational temperature showed a similar behavior in presence of argon gas. The variation of vibrational temperature at various argon gas pressure

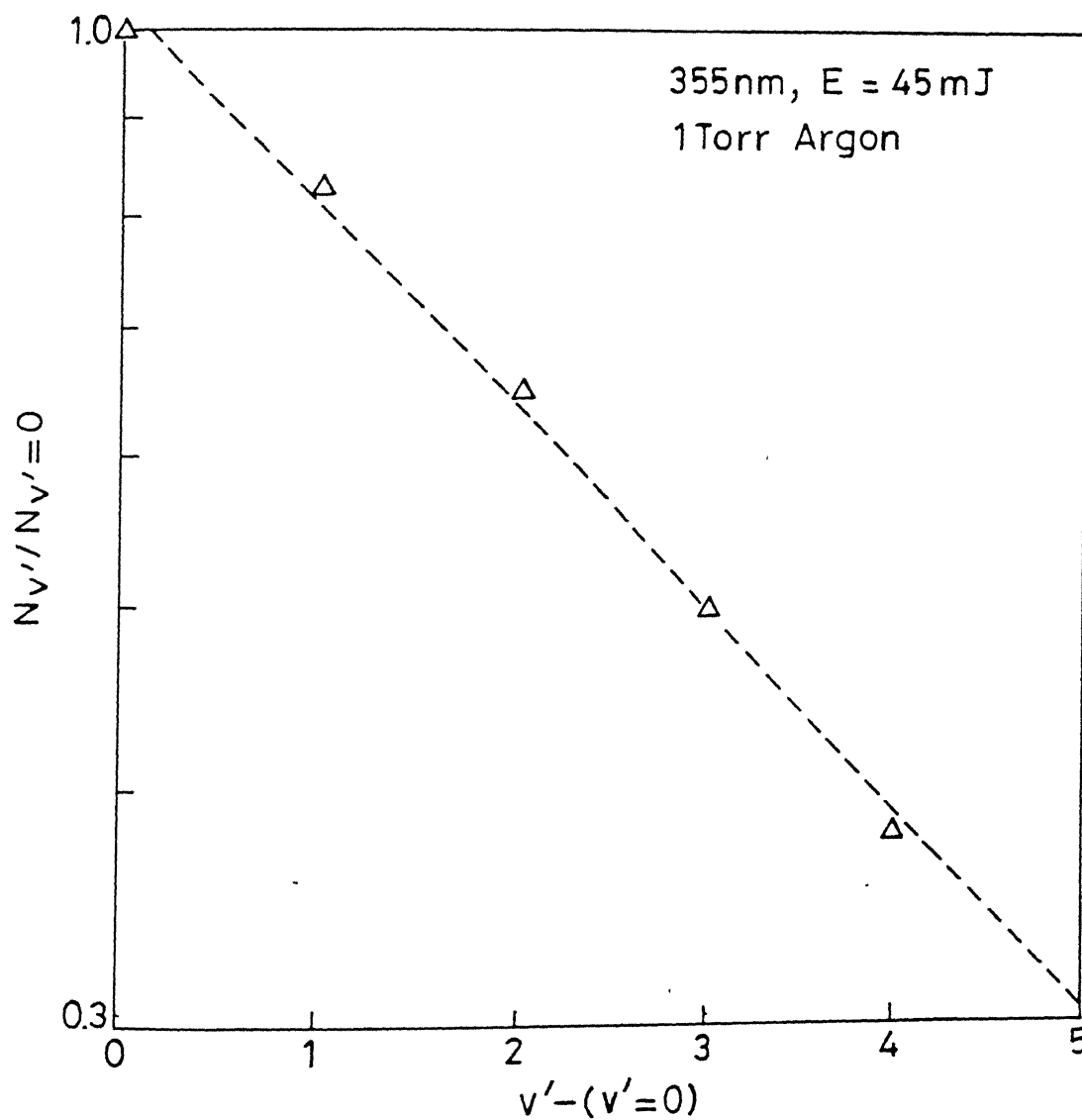


Fig. 32. Relative population of the upper vibrational level of the  $C_2$  Swan band sequence  $\Delta v = -1$  versus vibrational quantum number for 1 Torr argon gas pressure at 45 mJ energy of  $0.355 \mu\text{m}$  laser wavelength.

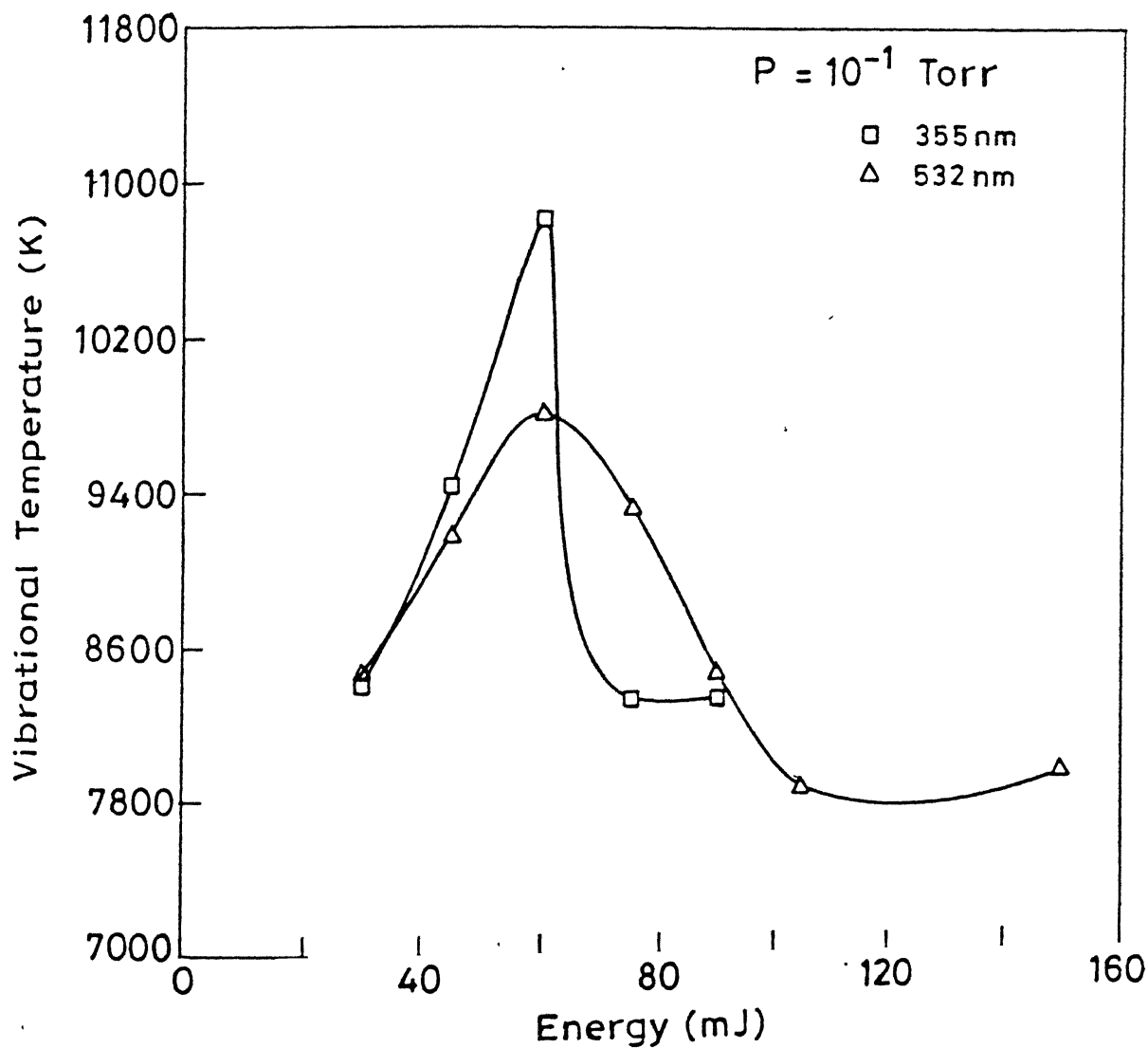


Fig. 33. Variation of vibrational temperature with energy for 0.532 and 0.355  $\mu\text{m}$  laser wavelengths at  $10^{-1}$  Torr argon gas pressure.

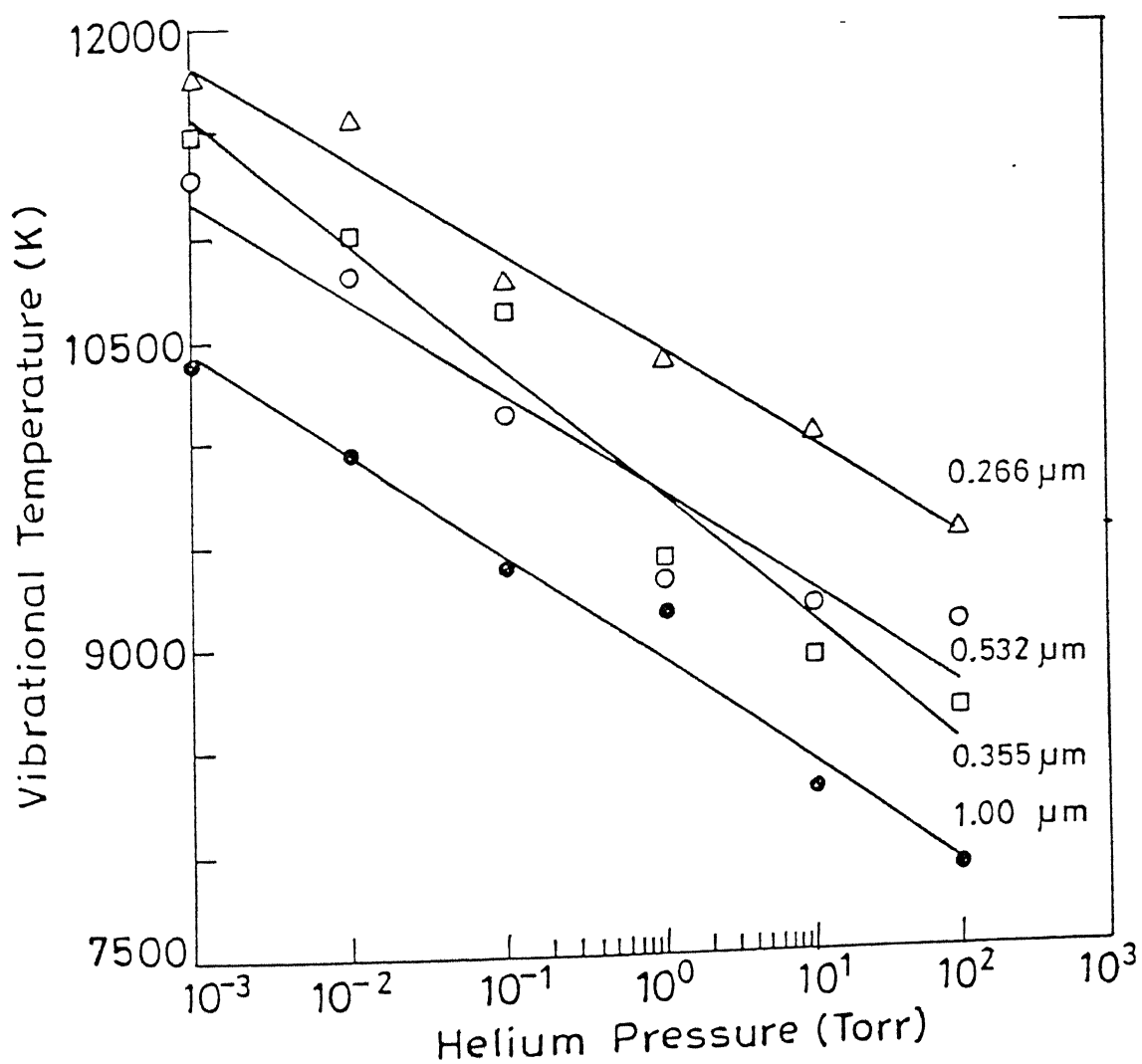


Fig. 34. Variation of vibrational temperature at various pressures of helium gas for 1.06  $\mu\text{m}$  at 60 mJ, 0.532  $\mu\text{m}$  at 40 mJ, 0.355  $\mu\text{m}$  and 0.266  $\mu\text{m}$  at 30 mJ laser energy.

for 1.06  $\mu\text{m}$  at a laser energy of 32 mJ, for 0.532  $\mu\text{m}$  and 0.355  $\mu\text{m}$  at 45 mJ is shown in figure 35. The vibrational temperatures in presence of argon gas are found to be relatively larger than that in presence of helium gas. This difference could be the result of the effect of the confinement of the gas. The restriction of the plasma expansion could be brought about by the surrounding gas. It results in the transfer of part of the plume expansion energy to the background atoms as thermal energy. The rate of removal of thermal energy by the gas atoms varies inversely as its mass, hence the heat removal by the argon gas atoms will be less than that for helium. It results in a higher plume temperature and also a larger emission intensity. The variation of vibrational temperature with argon gas pressure at 0.355  $\mu\text{m}$  behaved altogether differently. The vibrational temperature peaked at 1 Torr of argon gas and decreased with further change in argon gas pressure on either side. The larger vibrational temperature at 1 Torr of argon may yield the optimum quality films.

To estimate the expansion velocity of the  $\text{C}_2$  species, the temporal profiles of  $\text{C}_2$  d-a  $\Delta v = 0$  Swan band at 516.5 nm were recorded. The time resolved profiles at various ambient pressures were recorded corresponding to an optimum energy at which the  $\text{C}_2$  Swan band head intensity was found maximum. Figure 36 shows the temporal profiles of the  $\text{C}_2$  emission at various distances from the target surface at  $10^{-2}$  Torr helium gas using 60 mJ of 1.06  $\mu\text{m}$  laser radiation. It can be seen from the figure that the  $\text{C}_2$  species develop a double peak structure beyond a distance of 2 mm from the target surface. The fast component of the plasma was seen to dominate close to the target surface and is rapidly quenched with increasing distance. Beyond a certain distance the delayed slow component becomes predominant. The intensity of the peaks decreased with increase in distance at all ambient pressures. The delay corresponding to the fast component is found almost constant at all helium gas pressures. However, the delay for the slow peak behaved differently with change in helium gas pressure.

Since the presence of an ambient gas pressure has a significant influence on the plasma emission at various distances from the target, the dependence of delay on helium gas pressure at several distances was analyzed. Figure 37 shows the variation of the delay with helium gas pressure at various distances from the target surface. The delay time close to the target surface remains unaffected by the ambient pressure and increases with increase in helium gas pressure at larger distances. In vacuum the laser created plume undergoes a free expansion. However, in an ambient environment the collisional interaction with the

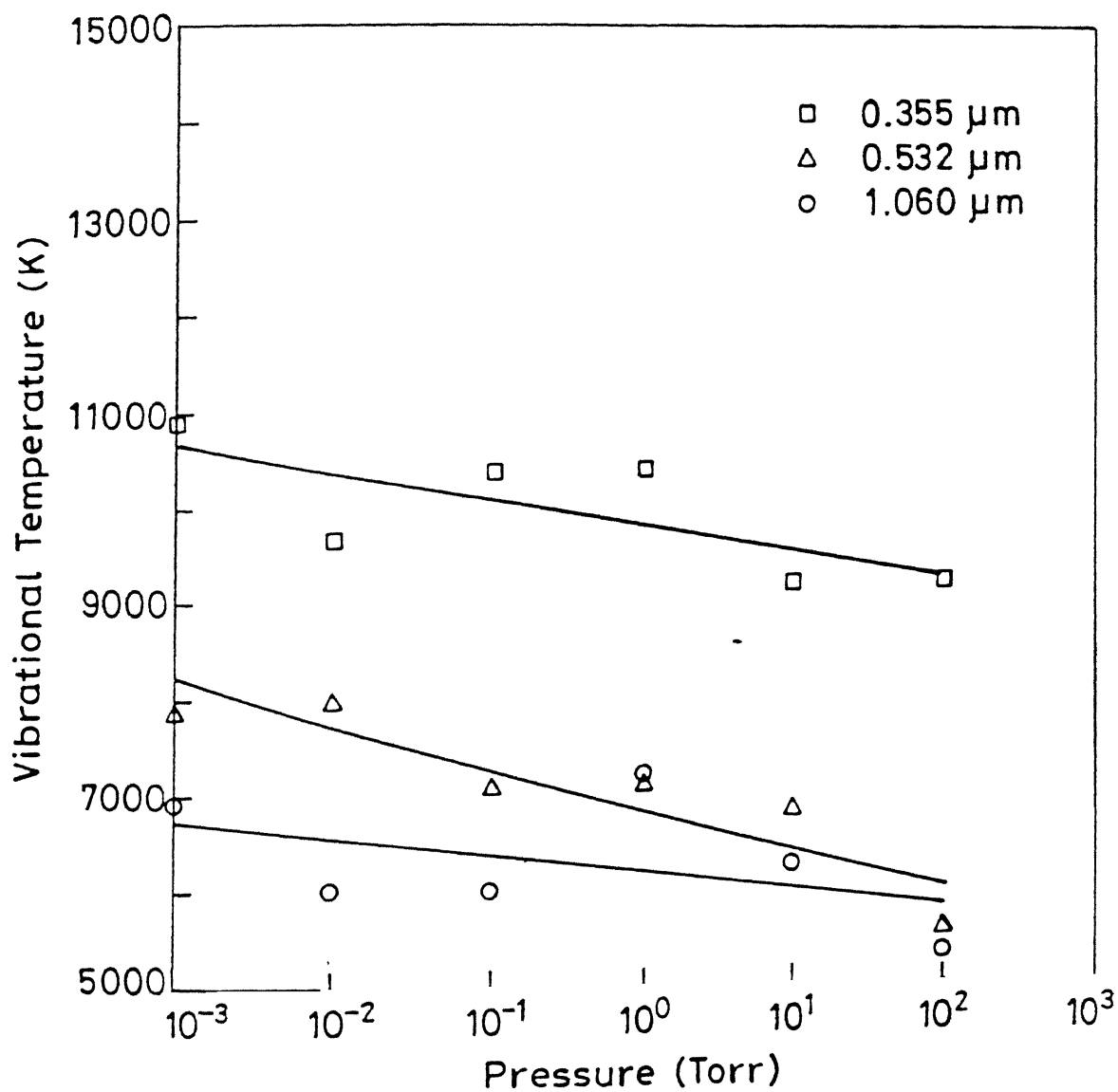


Fig. 35. Vibrational temperature as a function of Ar gas pressures for  $1.06 \mu\text{m}$  at 32 mJ,  $0.532 \mu\text{m}$  and  $0.355 \mu\text{m}$  at 45 mJ laser energy.

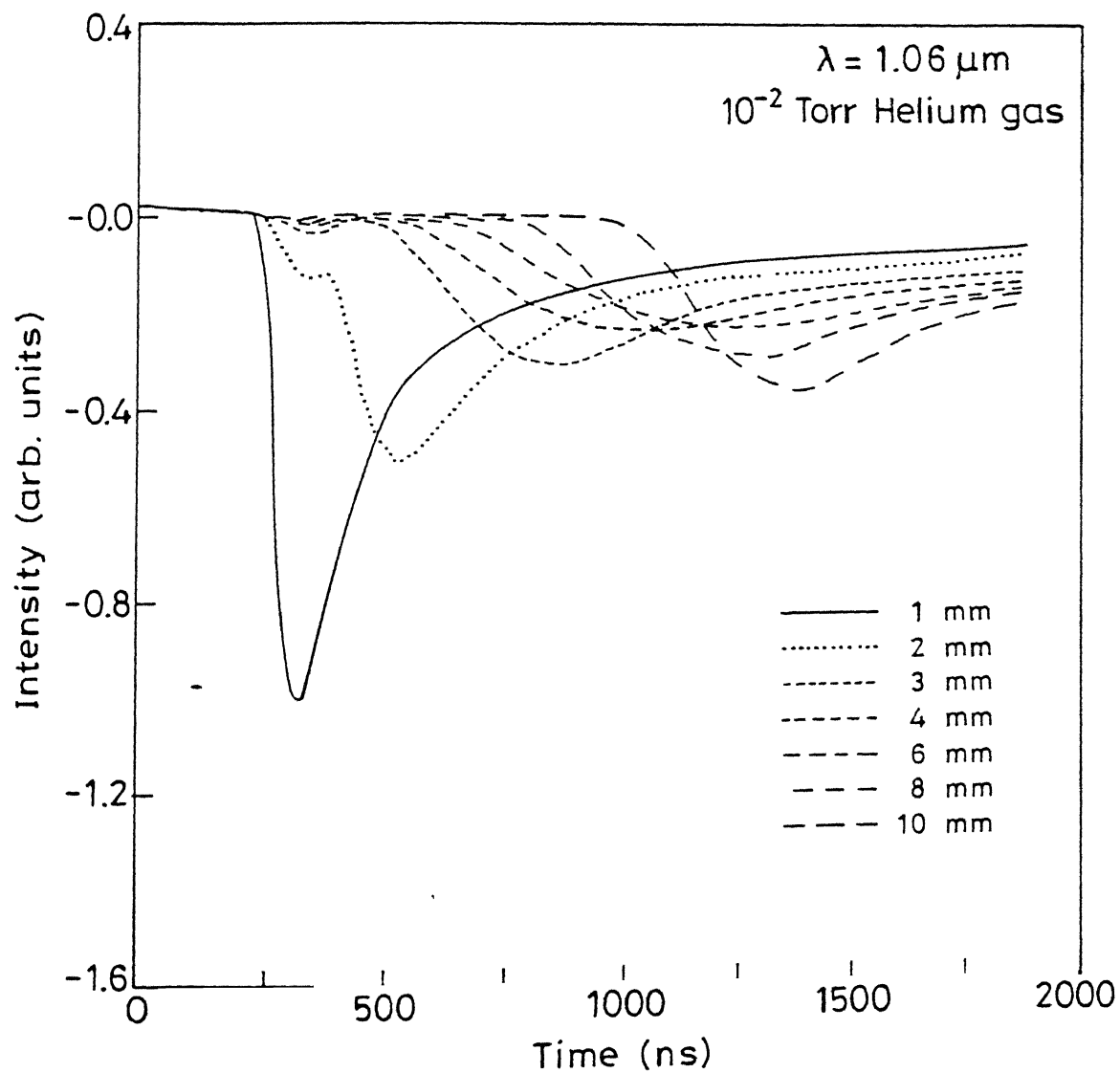


Fig. 36. Temporal profiles of C<sub>2</sub> band head at 516.5 nm at  $10^{-2}$  Torr helium gas pressure for 60 mJ energy of 1.06  $\mu\text{m}$  laser wavelength.



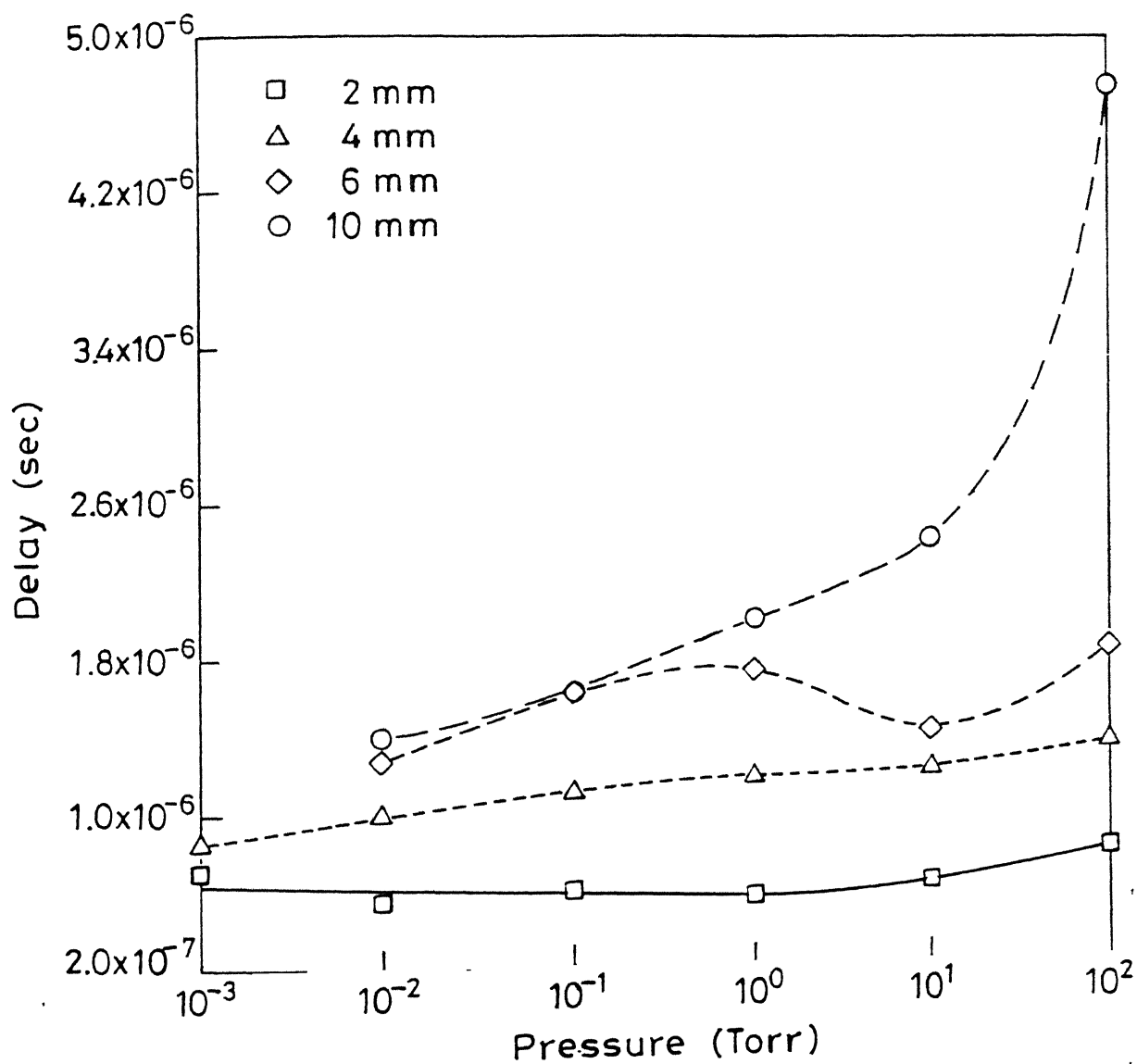


Fig. 37. Time delay for the appearance of second peak of  $C_2$  d-a  $\Delta v = 0$  Swan band with helium gas pressure.

background gas causes the plume to decelerate. The expanding plasma species can effectively be thought of as piston that acts to sweep up and drive the background gas causing a shock front to develop ahead of the contact surface. The propagation of the shock front by the background gas has been shown to follow a shock wave behavior of the form  $\xi = \xi_0 (E/\rho_0) t^{0.4}$ , where  $\xi_0$  is a constant,  $E$  is the total energy absorbed and  $\rho_0$  the density of the background gas.<sup>252-254</sup> Figure 38 shows the dependence of the time delay in attaining the  $C_2$  emission intensity maxima on the distance from the target surface in at 1, 10 and 100 Torr of helium gas pressures. The propagation of slow component follows a functional dependence of the form  $\xi = a t^\eta$  where  $a$  is a constant that depends on the pressure of the ambient gas. The value of  $a$  and exponent  $\eta$  both decreased with increase in helium gas pressure. The suppression of the plume expansion results with increase in helium gas pressure which may give rise to two different expansion mechanisms for the expansion front and the core of the plume. The expansion front which is subjected to plume-gas collisions would expand freely with a higher velocity than the high density core of the plume which undergoes extensive intraplume collisions. The slow component that represents the core of the plume leads to the formation of shock front that develops with increasing helium pressures.

### III. Ion Probe Diagnostics of Plasma Plume

The ion probe data for the laser ablated carbon plumes used for thin carbon film deposition were recorded at various argon gas pressures ranging from  $10^{-2}$  to 100 Torr using 100 mJ laser energy of 0.355  $\mu\text{m}$  laser wavelength. The data were taken at various angular positions of the probe ( $\theta$ ) with respect to target surface normal (TSN). The ion probe signals were recorded at various voltages in the range -180 to +180 volts. Figure 39 shows a typical ion and electron current signals as a function of time at probe voltage of -20 and +20 V respectively. Every point in the figures to follow is an average of five observations.

We observed the appearance of four ionic peaks at different delay times in vacuum along the target normal at all distances up to 20 mm. However, in presence of 1 Torr argon gas, the peaks were seen up to 8 mm only and thereafter only two peaks were observed. The maximum ion current for the peaks decreased with increase in distance. The maximum ion current corresponding to the second peak showed  $z^{-1.76}$  and  $z^{-2.51}$  dependence in vacuum and 1 Torr argon gas respectively. The square of the peak ion current plotted against probe

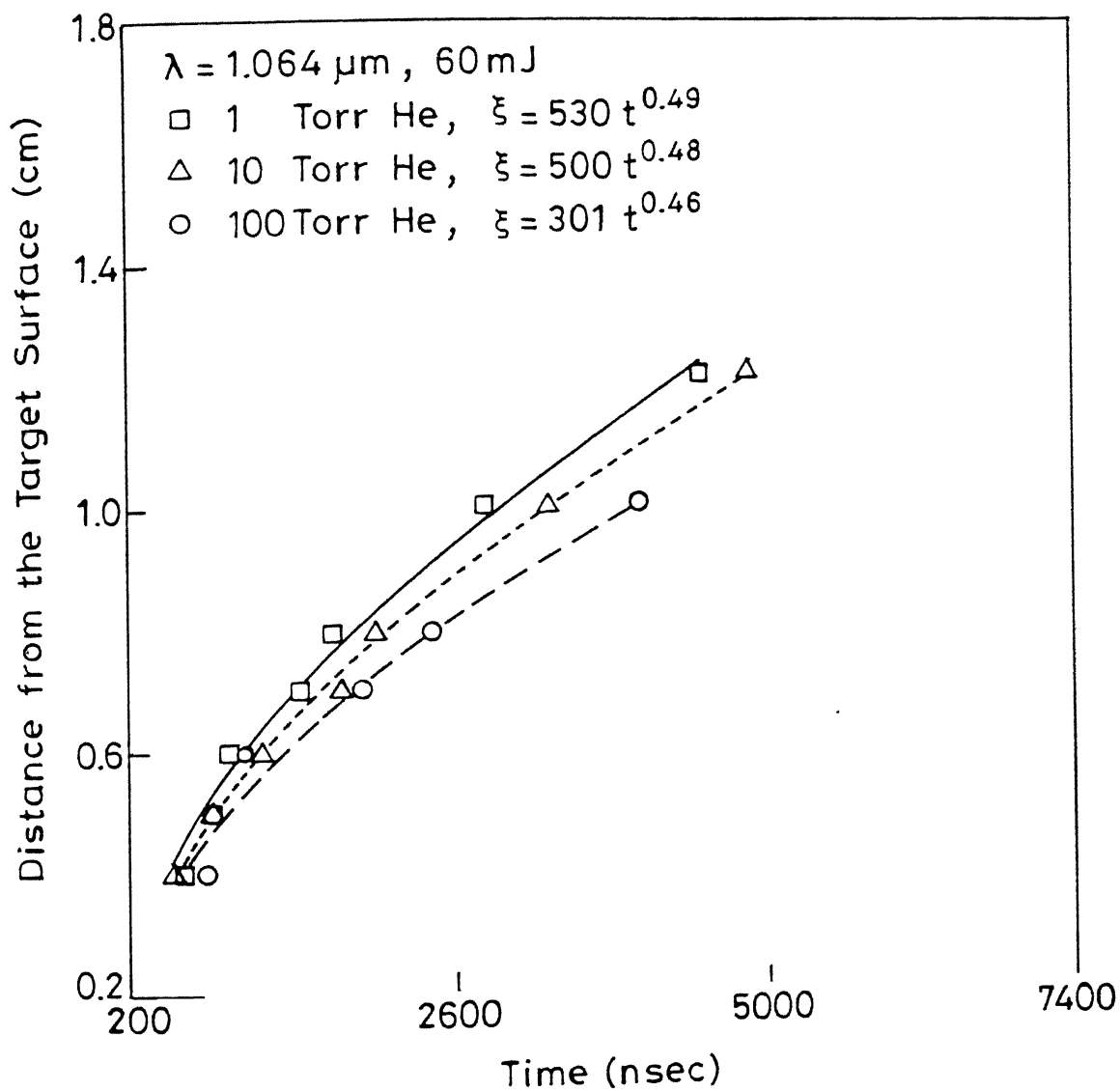


Fig. 38. Dependence of time delay with distance from the target surface.

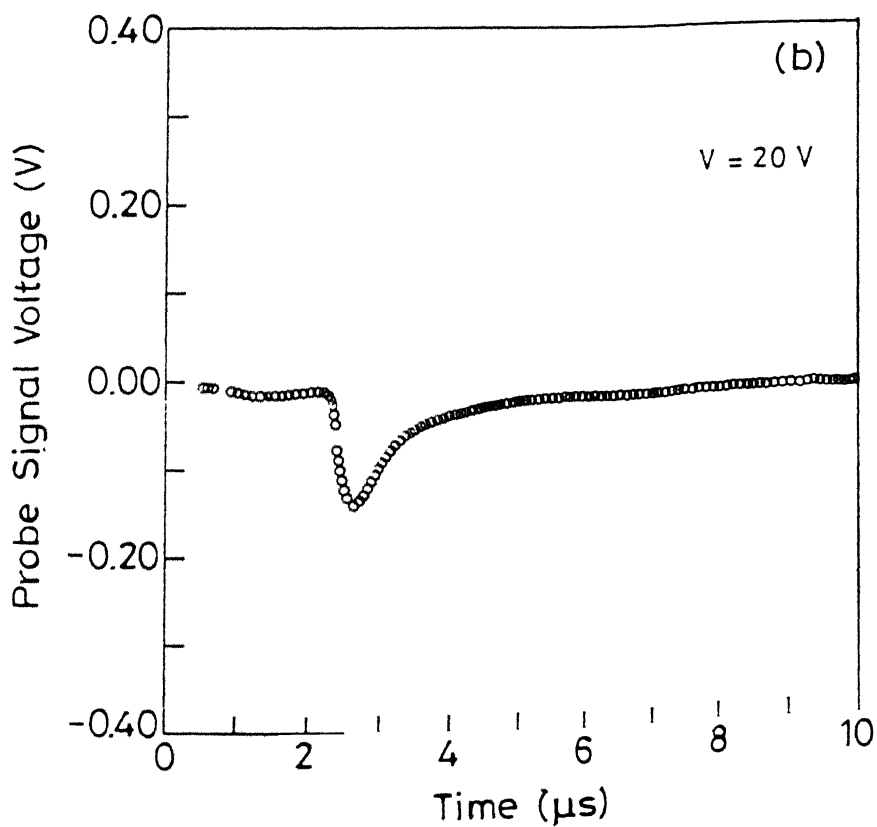
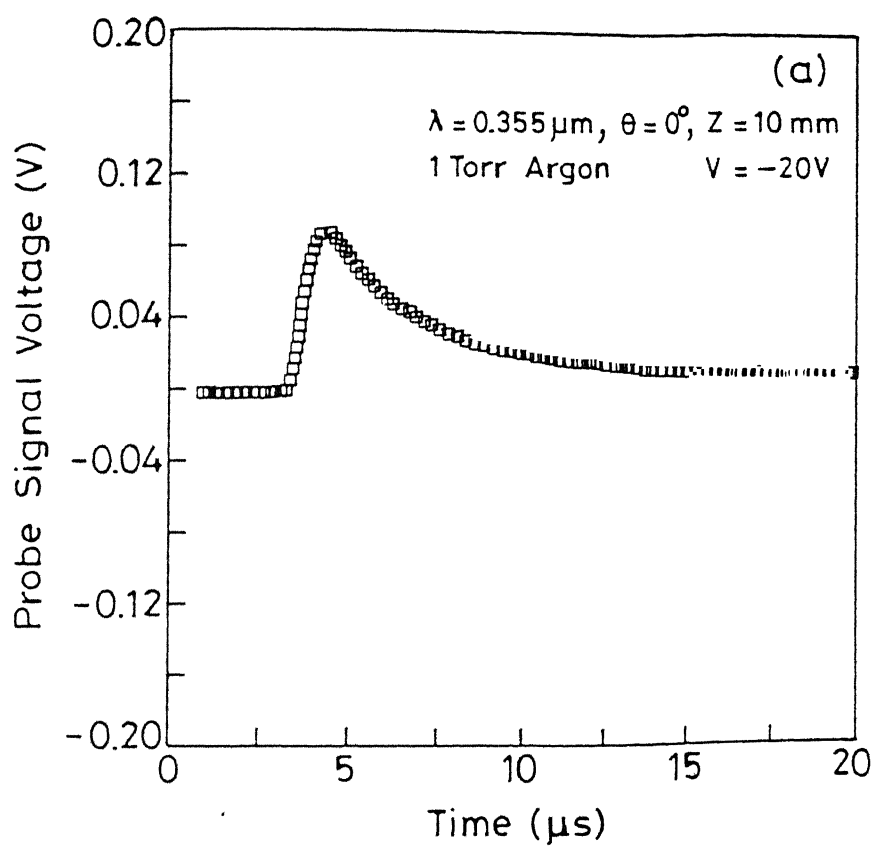


Fig. 39. Typical ion probe signal at (a) +20 V (b) -20 V for the probe target distance of 10 mm along the target surface normal at 1 Torr argon.

voltage is shown in figure 40. The slope of the linear part of the curve is used to calculate the ion density, Eq. 10. Figure 41 shows the variation of ion density with distance along the target normal for the first two ion peaks seen at all distances. The ion density decreased with increase in distance. The decrease in maximum ion current and density is attributed to recombination process in the expanding plume. The growth of the deposited films depend on the cumulative number of plasma species which in turn depend on the density. Hence the density of the plasma is an important factor in controlling the film structure.

The variation of the electron temperature with distance from the target surface along the target normal in vacuum and 1 Torr argon is shown in figure 42. The electron temperature in vacuum decreased slowly with increase in distance. However, the presence of argon gas altered the electron temperatures drastically. At 1 Torr of argon gas, the electron temperature is found to be higher than that in vacuum upto 10 mm and then attains a value close to that of vacuum. The marked differences in temperature in presence of 1 Torr argon is attributed to plasma confinement effect in presence of ambient gas. To correlate the results with deposited films, substrate was put at 10 mm in front of the target where the temperature is nearly constant. The details are given in Chapter V.

To study the angular variation of the plasma parameters in an ambient gas the probe was positioned at various angles with respect to target surface normal. Figure 43 shows the dependence of electron temperatures with argon gas pressures at  $\theta = 0^\circ, 30^\circ, 45^\circ$  and  $60^\circ$  at a distance of 10 mm from the target surface where  $\theta$  is the angle of the probe with respect to the target surface normal. The electron temperatures are strongly influenced by the pressure of ambient gas as well as the probe location with respect to target surface normal. In the direction of the target normal,  $\theta = 0^\circ$ , the electron temperature increases as the pressure is increased upto 1 Torr and then decreased with further increase in gas pressure. The behavior of the electron temperature variation with argon gas pressure at all other angles showed almost the same trend as  $\theta = 0^\circ$ , however, the variation in electron temperatures at other angles is not as large as  $\theta = 0^\circ$ . Also, the electron temperature decreases as the angle of the probe from the target normal is increased.

The behavior of ion density with argon gas pressures at a distance of 10 mm from the target surface at various angular locations is shown in figure 44. The density is found to be maximum at some intermediate pressure for  $\theta = 0^\circ, 30^\circ$  and  $45^\circ$ . The increase in density with pressure is attributed to three body recombination. The reduction in density may be due to

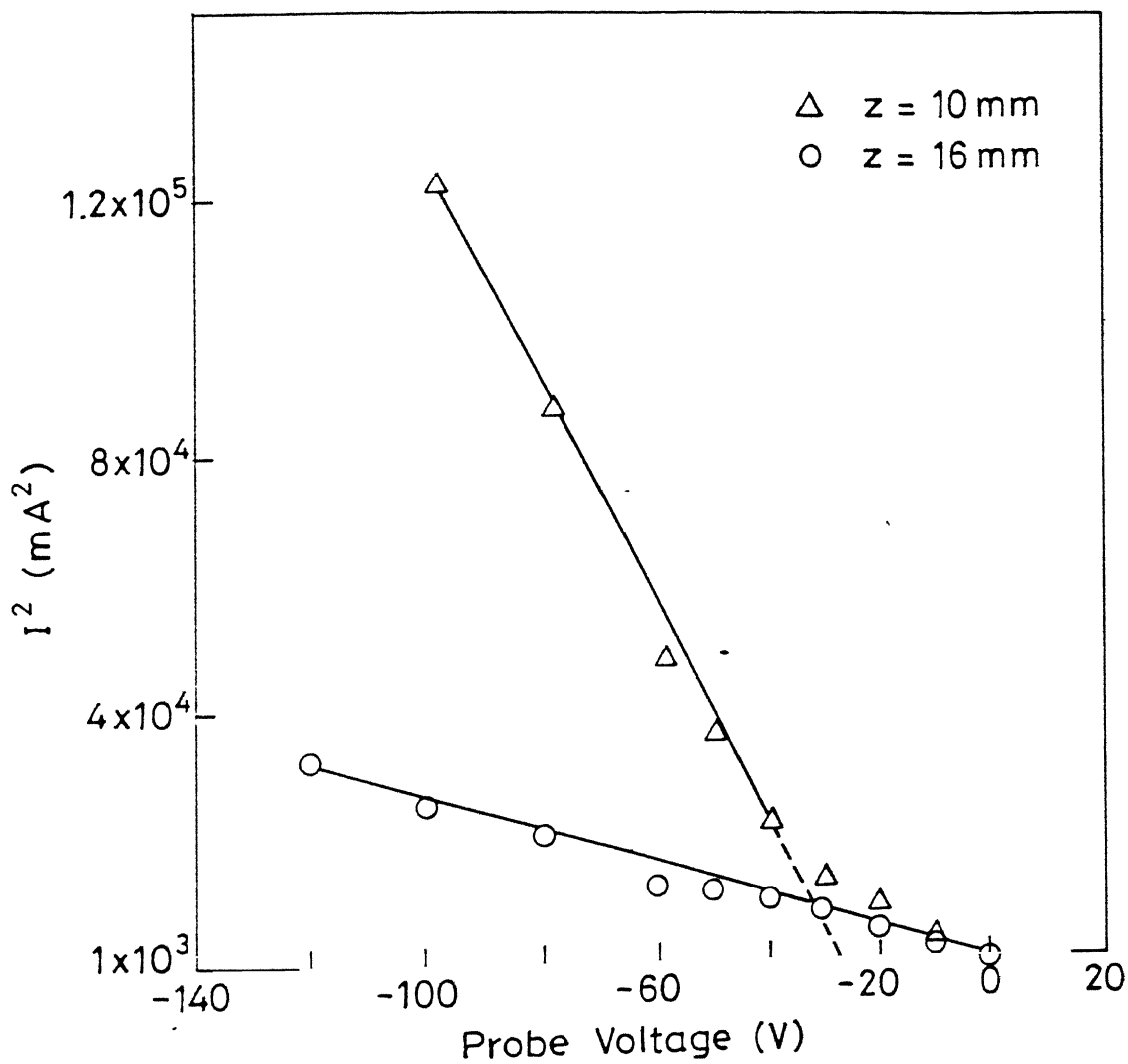


Fig. 40. Plot of square of ion current and probe voltage in vacuum at a distance of 10 and 16 mm along the target normal.

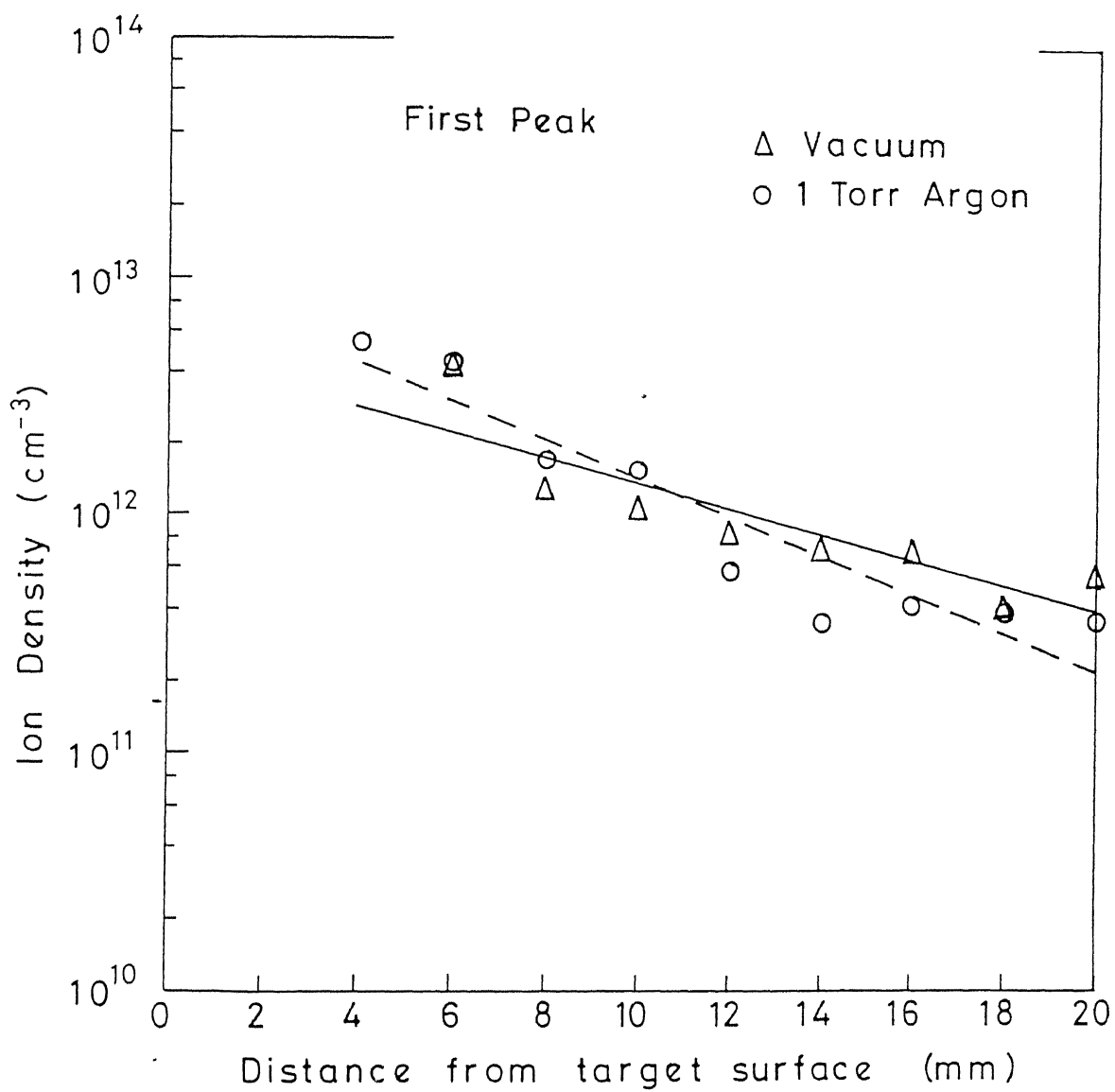


Fig. 41. Dependence of ion density on distance along the target normal for (a) first peak

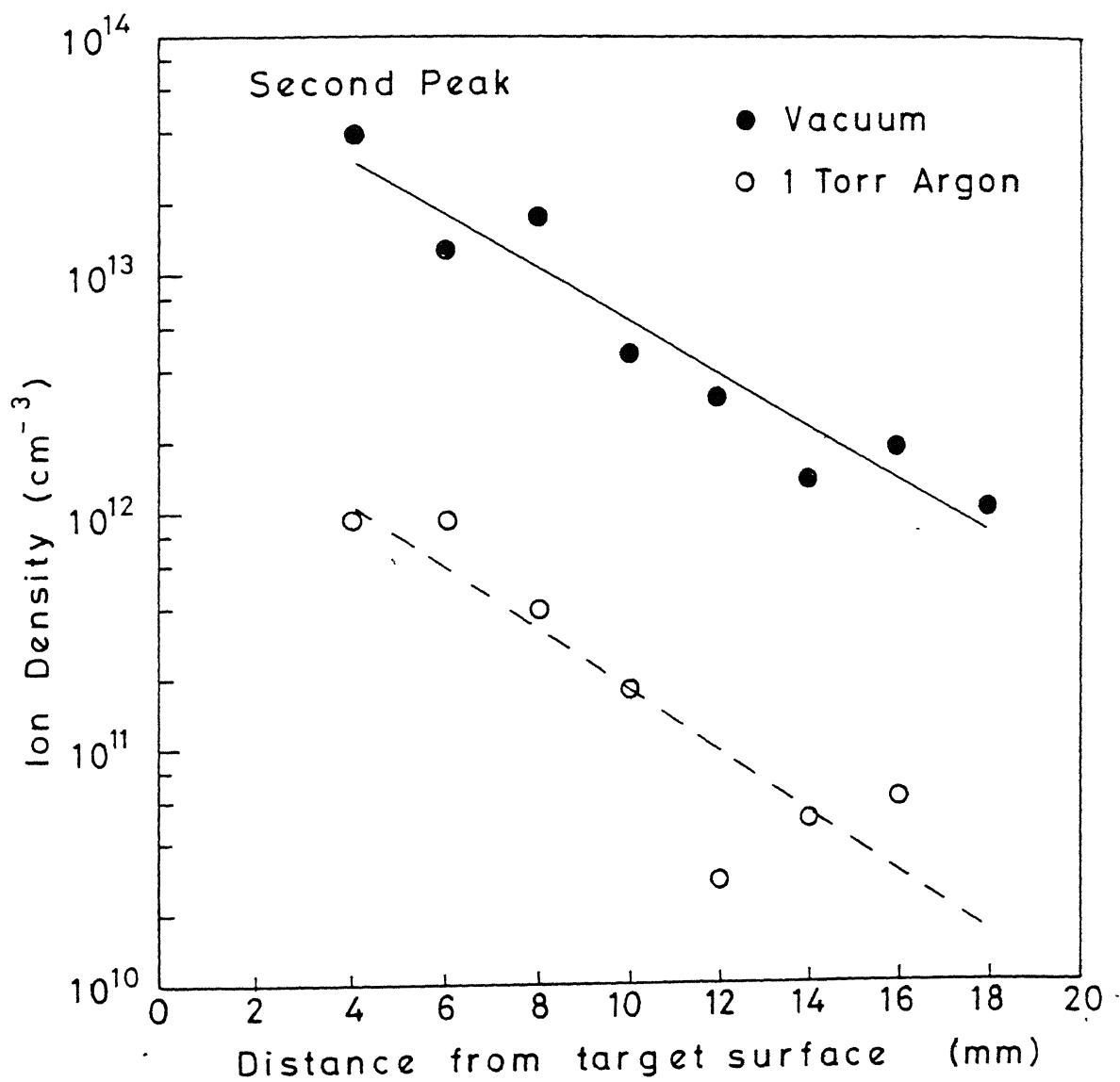


Fig. 41. Dependence of ion density on distance along the target normal for (b) second peak.



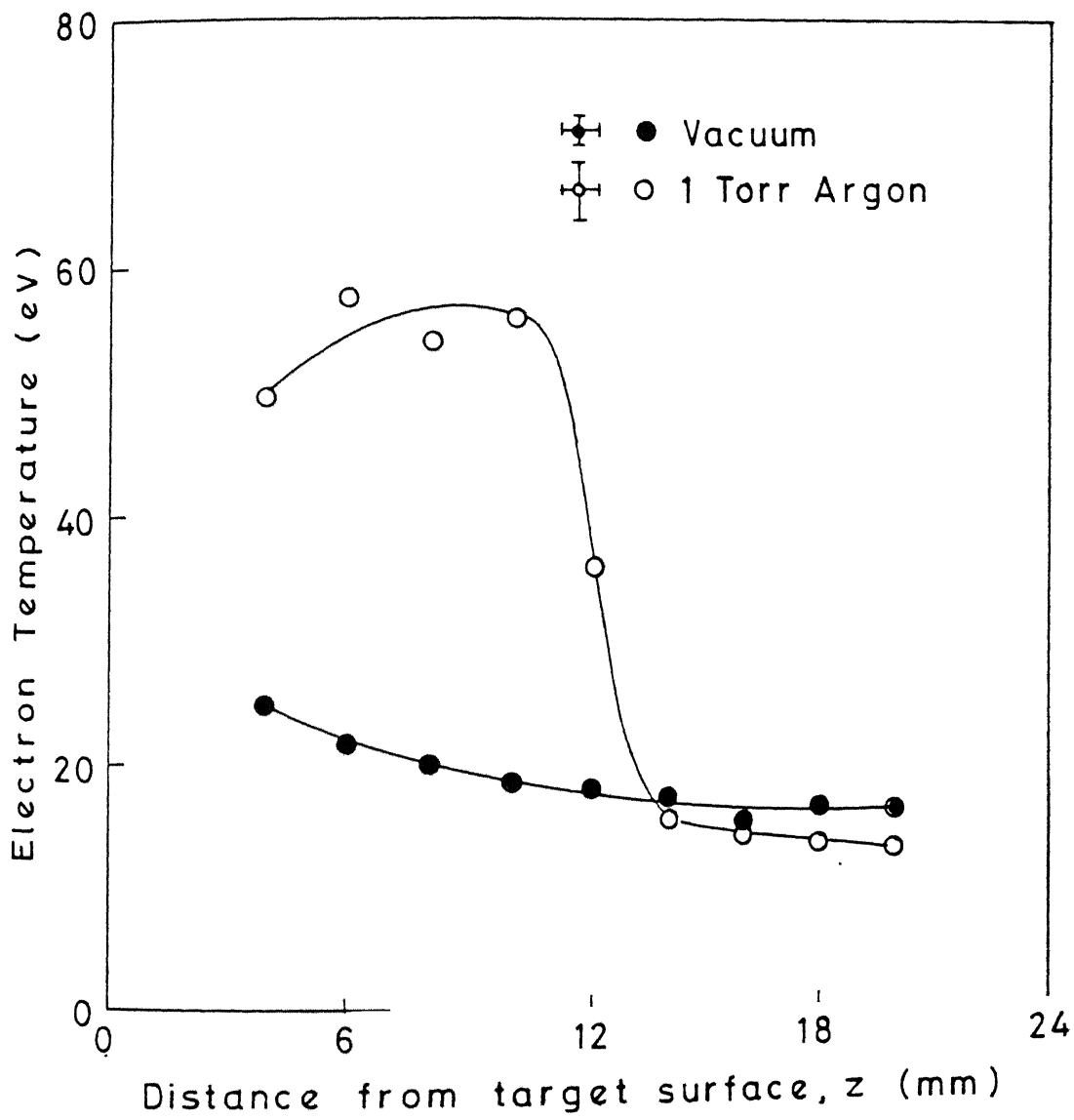


Fig. 42. Variation of the electron temperature with distance along the target surface normal.

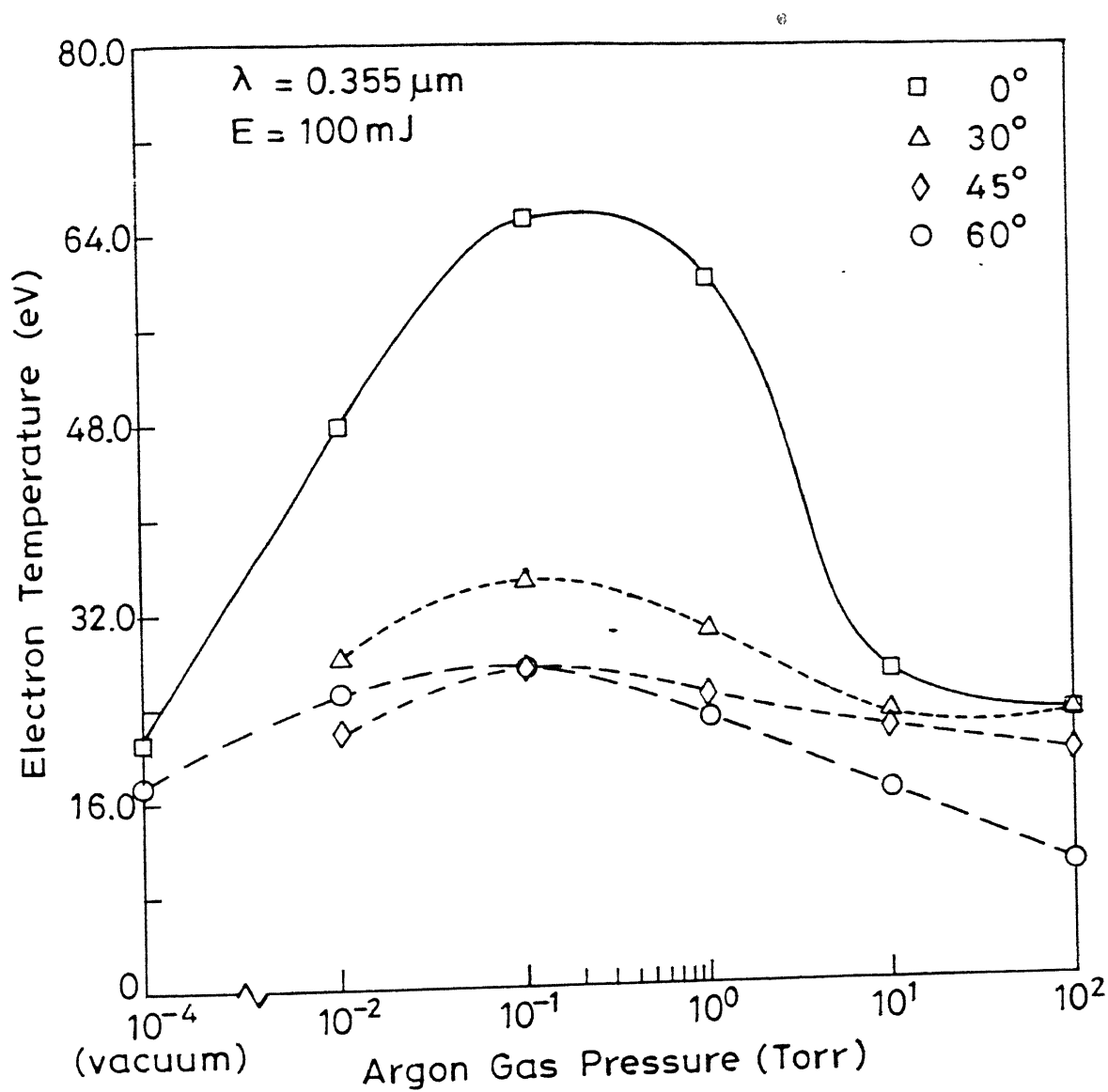


Fig. 43. Dependence of electron temperature with argon gas pressure at various angular positions with respect to target surface normal.

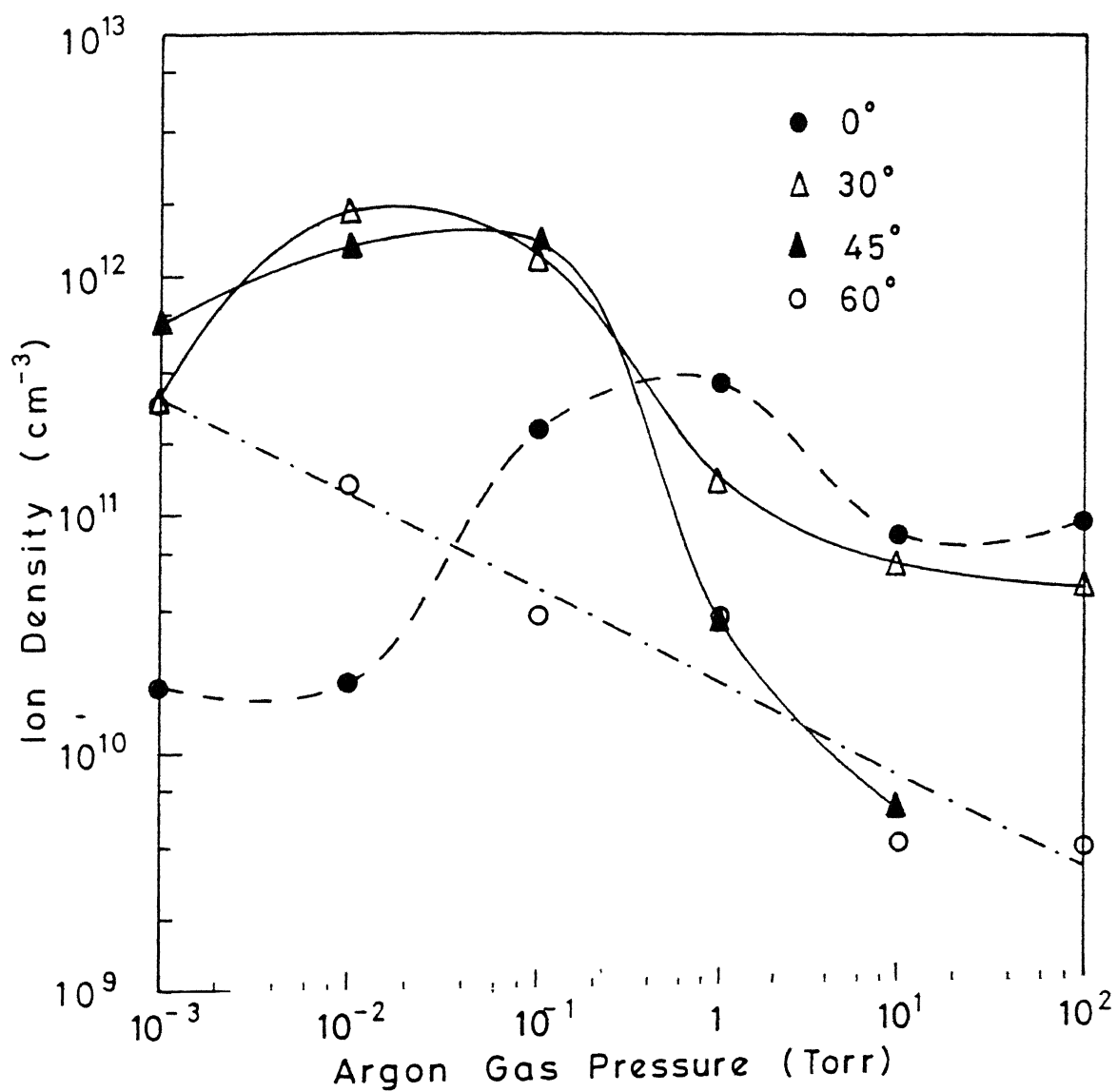


Fig. 44. Variation of ion density as a function of argon gas pressure.

high cooling rate at higher background gas pressure. However, at  $\theta = 60^\circ$  the density decreased as the pressure increased.

To see the effect of laser irradiated area on the target surface, the ion probe data were recorded at a distance of 10 mm along the target surface normal at 1 Torr of argon gas pressure. The laser spot size on the target surface was varied by moving the lens towards the target surface at fixed laser energy. Figure 45 shows the variation of ion density with the laser irradiance at a distance of 10 mm along the target surface at 1 Torr of argon gas pressure. The ion density is found to increase with increase in laser irradiance and then becomes constant at higher laser irradiances. Our results on the variation of ion density agree well with the results obtained on carbon using 248 nm KrF laser by Voevodin et al.<sup>82</sup>

Figure 46 shows the angular variation of ion density at various argon gas pressures. The ion density is found to be maximum at  $\theta = 45^\circ$  in vacuum (better than  $10^{-4}$  Torr). However, as the argon gas pressure is increased, the maxima in the ion density moves towards the target normal. It is found that the ion density is maximum along the target normal and decreases as the angle is increased at all pressures greater than 1 Torr. It looks from our observations that plume tilts towards the laser beam in vacuum and at argon gas pressures below 1 Torr. Beyond 1 Torr argon gas pressure, plume seems to be forward directed towards the target surface normal.

To investigate the angular spread of the ions in the plume, the ion density calculated at various angles at various argon gas pressures was fitted to cosine-functions. The fit gives the dependence of ion density which follows  $\text{Cos}^p \theta$  behavior. The behavior at 1 Torr argon gas pressure is shown in figure 47 at various target-probe distances. Here the data points represent the experimental observations. Every point is an average of five observations. The value of  $p$  is found to be 9.7, 6.7 and 3.1 at 6, 10 and 14 mm respectively. Figure 48 shows the variation of power of the fitted cosine-function ( $p$ ) with argon gas pressures. The value of  $p$  is strongly dependent on argon gas pressure. In vacuum ( $<10^{-4}$  Torr), the ion density distribution shows  $\text{Cos}^9 \theta$  dependence. The anisotropic distribution may be due to sharp angular distribution of the ablated species. The value of  $p$  decreases as the pressure of the background gas increases. This result implies that the directionality of the traveling plasma species is disturbed due to collisions with argon gas. In vacuum, the plume angular distribution is determined by collision of the plume particles among themselves. In presence of background gas the plume angular distribution is perturbed by additional collisions of

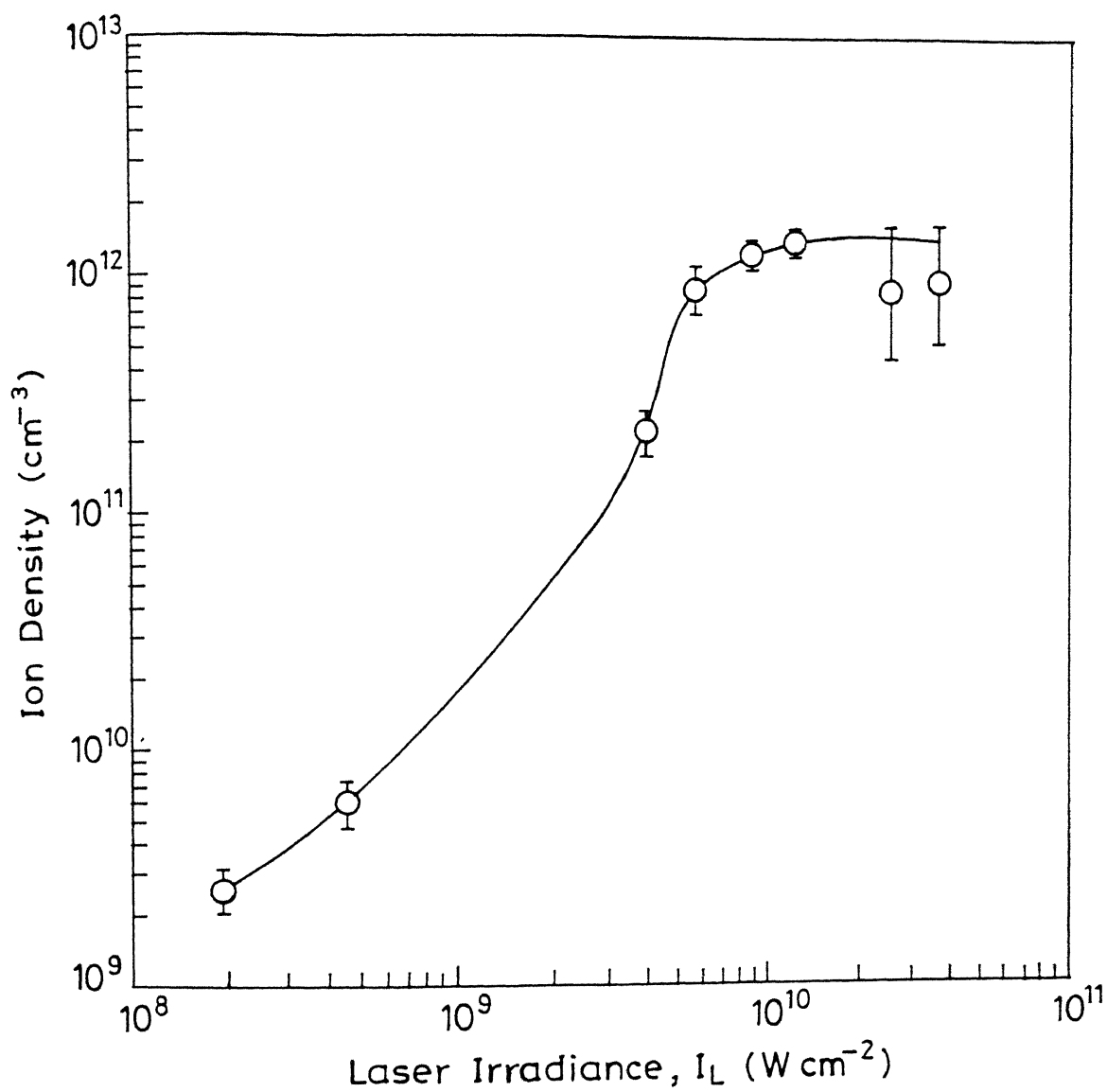


Fig. 45. Dependence of ion density on the laser irradiance at 10 mm distance along the target surface normal at 1 Torr argon gas pressure.

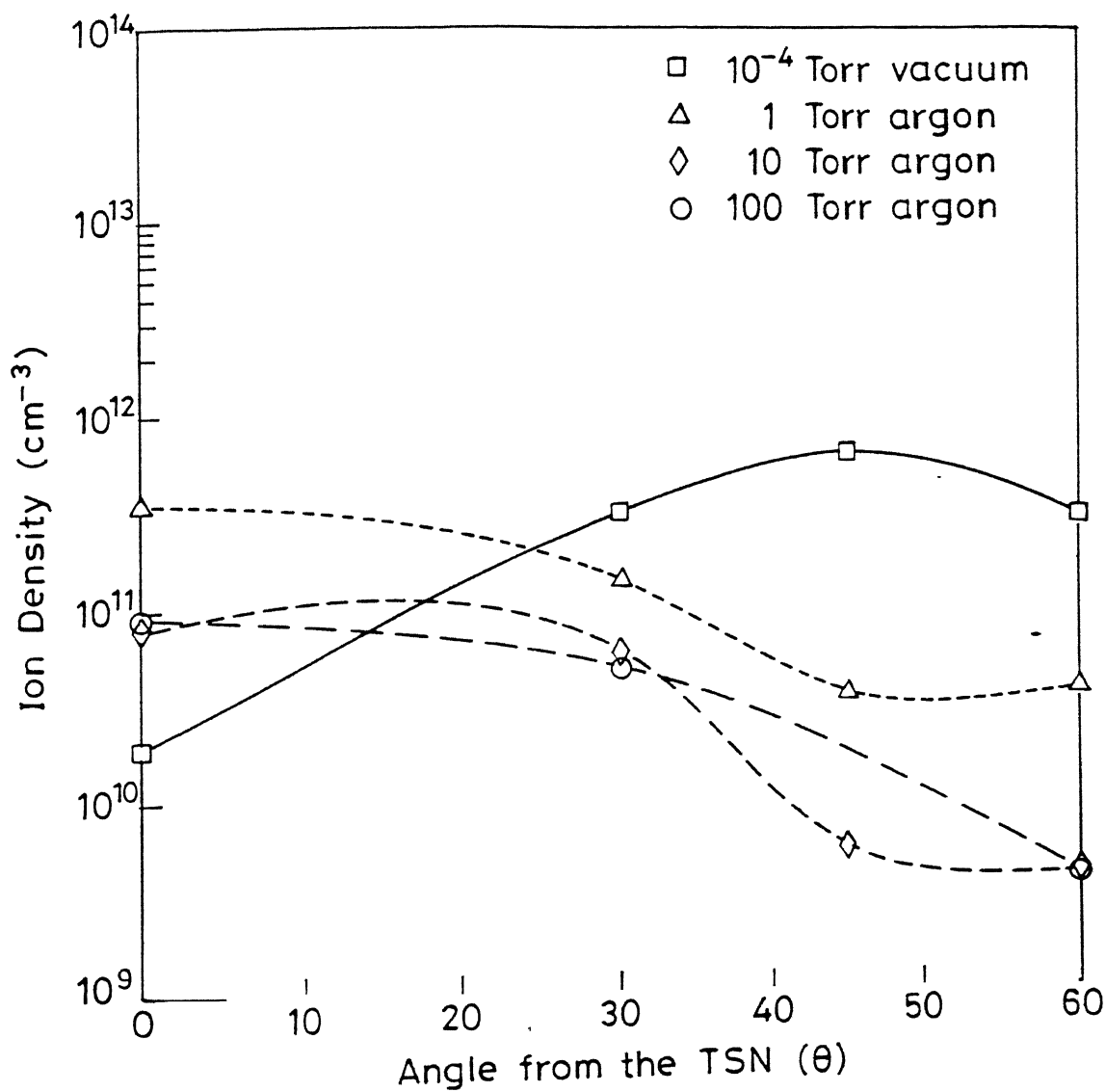


Fig. 46. Dependence of ion density on angle at various argon gas pressures.

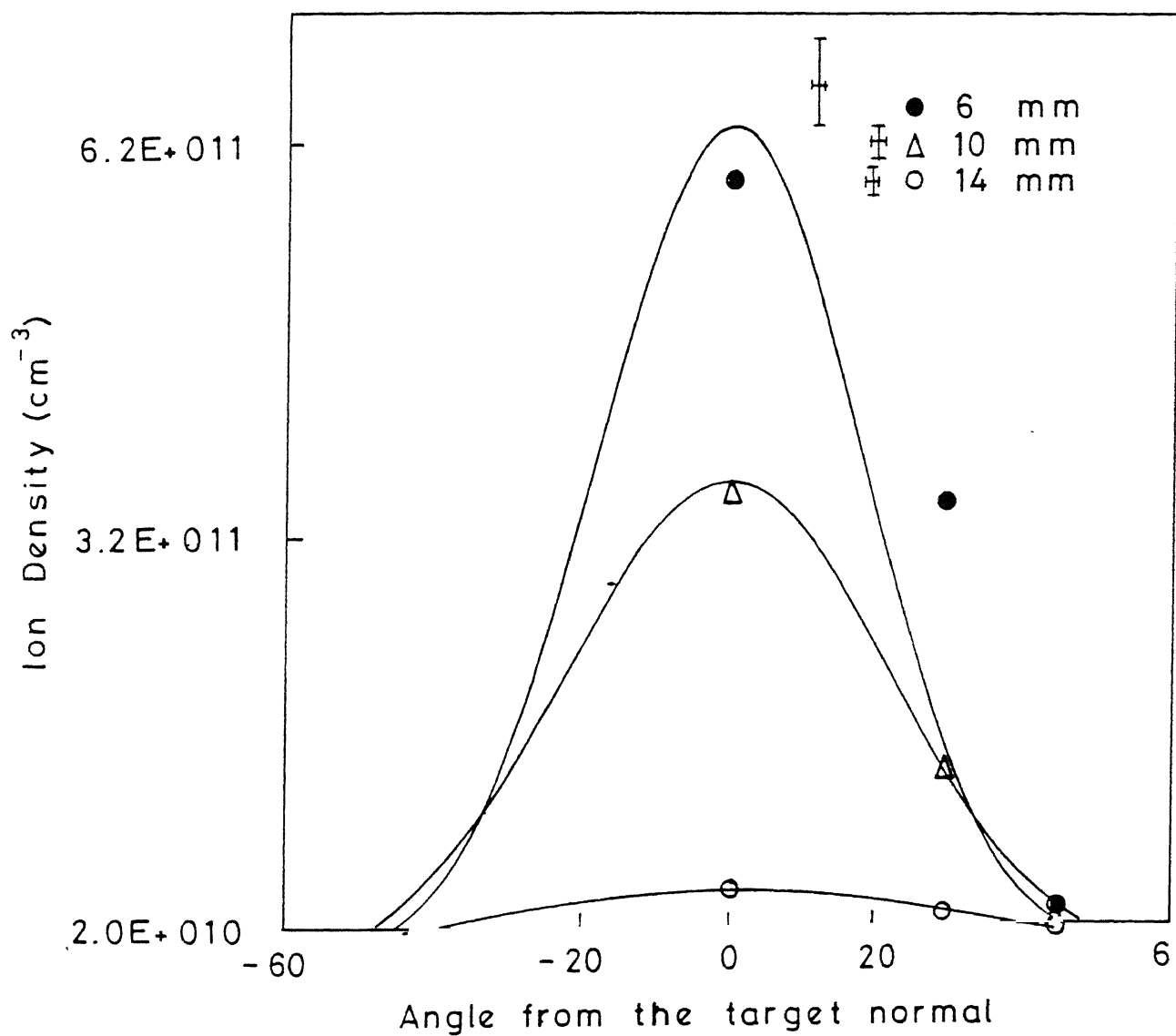


Fig. 47. Ion density angular profiles at 6, 10 and 14 mm along the target surface normal at 1 Torr of argon gas pressure.

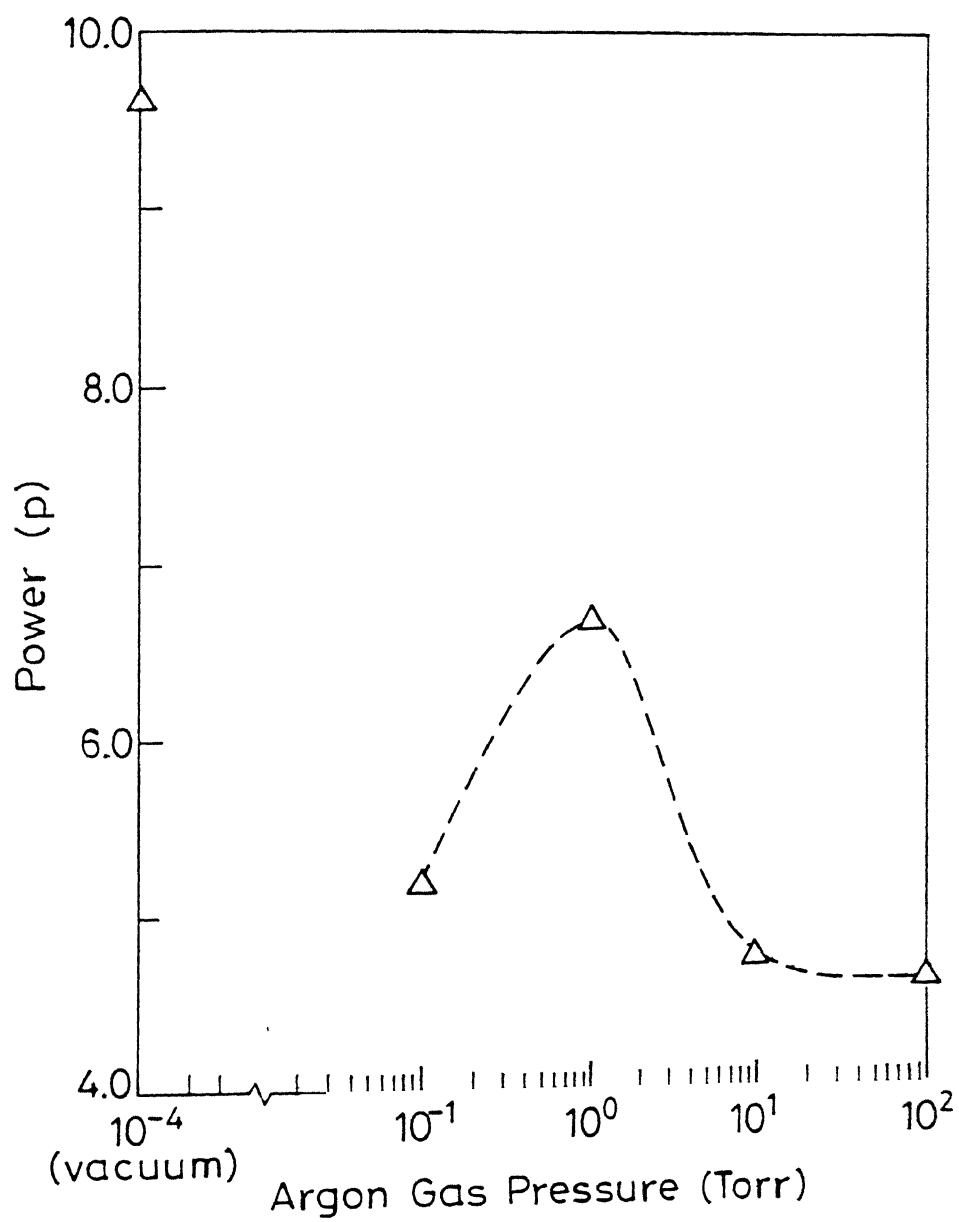


Fig. 48. Variation of the power of the fitted cosine-function with argon gas pressure.



plume particles with that of background gas. These collisions scatter the plume particles and broadens the angular distribution. The value of  $p$  observed in our case decreases in the presence of ambient gas and is more at 1 Torr of the argon gas as compared with other ambient pressures. It follows from our observations that plasma plume at 1 Torr of argon gas pressure is more directional and forward directed as compared to higher pressures. Also the value of  $p$  at various distances from the target surface at 1 Torr of argon gas pressure decreases with increase in distance. It indicates that the angular distribution of the ions becomes broader with increasing distance from the target surface. This is expected as the scattering effects increase with increasing distance, thereby reducing  $p$  with distance.

The velocity of the ions was evaluated using the delay timings of the ions obtained from ion probe signals. The velocity of the ion decreased in presence of the ambient gas. Figure 49 shows the variation of delay time with angle from the target surface normal. The delay increases with increase in angle. It indicates that the velocity of the ion is maximum along the target normal and decreases with increase in angle.

In conclusion, we studied optical emission from laser ablated carbon plume to estimate plasma parameters as a function of distance from the target surface at high and low laser irradiance. Electron temperature and density were calculated using emission lines intensity ratio and Stark broadening of the spectral line respectively. The velocity of the plasma front is found to decrease in presence of an ambient gas. At low laser irradiances, the molecular  $C_2$  emission was dominant. The vibrational temperatures calculated using  $C_2$  Swan band head intensity showed a maxima at some intermediate energy which decreased with decrease in laser wavelength. Vibrational temperatures decreased with increase in helium gas pressure, however, in presence of argon gas at  $0.355\ \mu\text{m}$  laser wavelength the temperature is found to be maximum at 1 Torr of argon gas pressure and decreased in change of pressure on either side. The temporal profiles of  $C_2$  showed the plume bifurcation into a fast and slow component in presence of the ambient gas beyond a certain distance from the target surface. The slow component is shown to follow the blast wave model at higher helium pressure.

The plasma parameters estimated using ion probe measurements of the laser ablated carbon plume are strongly dependent on the distance from the target surface, angle from the target surface normal and ambient gas pressure. The electron temperature was found to be maximum along the target surface normal at 1 Torr of argon gas. The electron temperature at

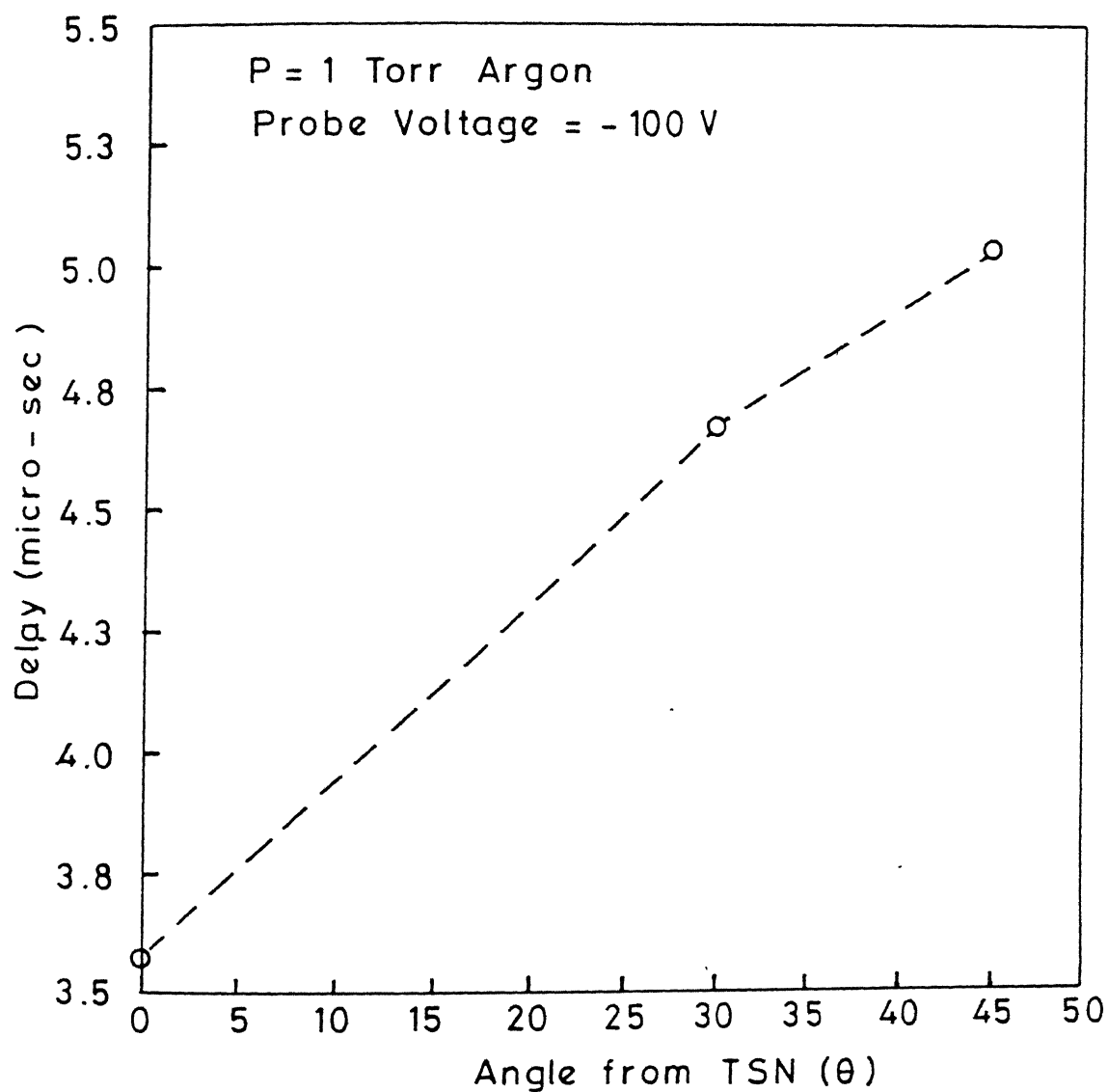


Fig. 49. Delay as a function of angle from the TSN. The dashed line is a guide to eye.

1 Torr argon gas was constant upto 10 mm and then decreased attaining a value close to that of vacuum at larger distances. The forward directed nature of the process is strongly influenced by the pressure of the ambient gas. The ion density profiles are strongly peaked in the direction normal to the target surface and the distribution broadens with increase in distance from the target surface.

## CHAPTER V

### CHARACTERIZATION OF LASER ABLATED THIN CARBON FILMS

#### INTRODUCTION

Since the initial report of Smith and Turner<sup>14</sup> in 1965, the laser ablation deposition (LAD) technique has become one of the forefront technique in thin film growth. Its emergence into the mainstream in the past several years has been due to its successful application for depositing variety of materials such as insulators, semiconductors, metals and superconductors etc.<sup>13</sup> The flux of the material to be deposited is generated by irradiating an appropriate target with high intensity beam of pulsed laser light and a film is grown by collecting this flux onto a suitably placed substrate. The deposited flux can be modified by changing the ambient conditions, e.g., background gas and/or plasma. Laser produced plasma is believed to play a key role in controlling the growth, structure and properties of the deposited films.

In the present chapter, the results on the characterization of pulsed laser deposited thin carbon films<sup>110</sup> using SEM, TEM, SAED, XRD, micro-Raman and resistivity measurements are presented. The correlation of the deposited films characteristics with the characteristics of the plasma is discussed.

#### Experimental Set up

The experimental set-up used for thin carbon film deposition is shown in figure 9. The ablated carbon was deposited on silicon and glass substrates placed 10 mm from and parallel to the target surface. The substrates were ultrasonically cleaned in methanol several times and finally rinsed in dilute HF before being used for deposition. The films were deposited in the presence of helium and argon gas pressures at room temperature. The deposition time (20 min) was kept constant for all the deposited films. Specimen for transmission electron microscopy analysis were prepared by depositing the films on small copper grids under similar conditions.

## RESULTS AND DISCUSSION

Various techniques used for characterizing the deposited films are listed in Table 2. We used the SEM, TEM, XRD, micro-Raman and resistivity measurements to characterize the deposited thin carbon films. The films were deposited in helium and argon atmosphere at various pressures using different irradiance and wavelength.

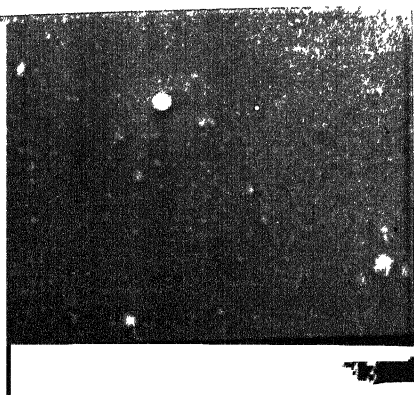
### Scanning Electron Microscopy

Scanning electron microscopy (SEM) was used to investigate the surface morphology and nucleation density of the deposited films. Figure 50 shows SEM images of the carbon films deposited on silicon substrates using  $3.8 \times 10^8 \text{ W/cm}^2$  laser irradiance of  $0.355 \mu\text{m}$  radiation. The figure shows the effect of the argon gas pressure on the surface morphology. The surface morphology of the films changes dramatically with increasing argon gas pressure, with densely packed spherical features dominating the films. Large spherical protrusions of different diameters are observed on the silicon surface. The nucleation density of the clusters on the substrate surface was found to be at a maximum at 1 Torr of argon gas pressure, while it decreased on either side with change of argon gas pressure. The typical growth rate of the deposited films using SEM was found to be approximately 25 nm/sec.

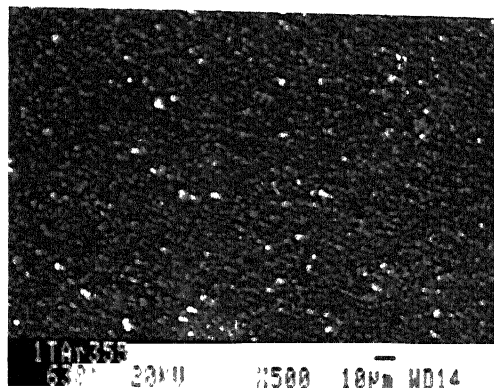
The films deposited at various helium gas pressures<sup>132</sup> using  $7.8 \times 10^8 \text{ W/cm}^2$  of  $0.532 \mu\text{m}$  laser radiation showed altogether different behavior than that obtained in presence of argon. The nucleation density of the carbon clusters increased with increase in helium gas pressure up to 100 Torr. However, beyond 100 Torr carbon films started peeling off and showed "cauliflower" morphology with no systematic pattern. This variation in the morphology of the films has been attributed to the temperature variations in the laser ablated carbon plumes at various helium gas pressures.

### Transmission Electron Microscopy and Selected Area Electron Diffraction

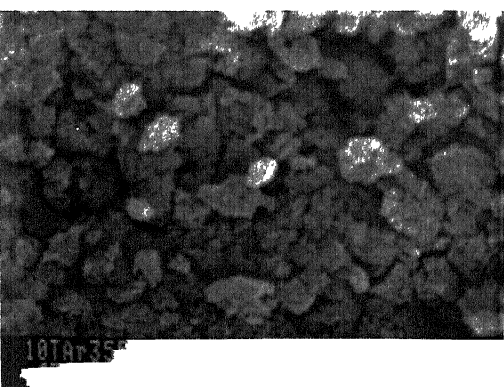
Cross sectional TEM was used to extract the information on the structure of the deposited films. The TEM micrograph and the corresponding selected area electron



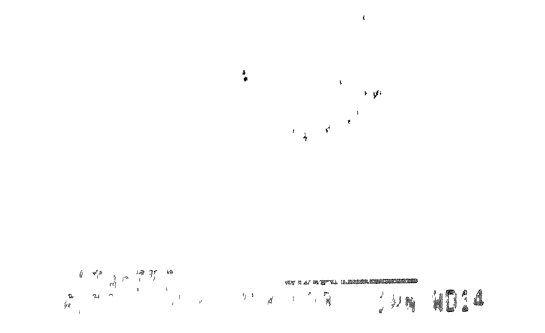
(a)



(b)



(c)



(d)

Fig. 50. SEM micrographs of laser ablated carbon films at (a)  $10^{-1}$ , (b) 1 and (c) 10 Torr (d) single microcrystal at 1 Torr of Ar gas pressures.

diffraction pattern of the film at 1 Torr argon gas pressure is shown in figure 51. The diffuse intensity of the rings suggests quasi-crystalline nature of the film. The ring patterns represent typically poly-crystalline face centered cubic material. Although diffraction rings are not clearly visible in figure 51(b) due to contrast limitations in the image, three rings are clearly visible in the negative. The  $d_{\text{lattice}}$  - spacing of the rings were determined using original negative. The measured  $d_{\text{lattice}}$  - spacings of the rings 2.057 and 1.241 Å matches well with the (111) and (220) planes of cubic diamond respectively.<sup>226</sup> Also, the relatively strong intensity graphitic rings, especially the basal plane (002) at 3.357 Å which is strongest expected graphite reflection in polycrystalline sample does not seem to appear in the diffraction pattern. It indicates the presence of diamond for the film deposited at 1 Torr of argon.

## X-ray Diffraction

Since the electron diffraction patterns for the carbon allotropes often are inconclusive due to small  $d_{\text{lattice}}$ - spacing difference between the diamond and graphite, the structural properties of the deposited carbon films obtained at various argon gas pressures ranging from  $10^{-2}$  to 100 Torr were further investigated by XRD using a standard  $\theta/2\theta$  diffractometer (Cu-K $\alpha$  radiation). Figure 52 shows the XRD pattern of the film deposited at 1 Torr of argon gas pressure at  $3.8 \times 10^8$  W/cm<sup>2</sup> irradiance. The peaks at  $43.5^\circ$ ,  $76^\circ$ ,  $91.5^\circ$  and  $120^\circ$  indicate the presence of (111), (220), (311) and (400) crystalline planes of cubic diamond. It confirms the presence of some diamond particles in the film deposited at 1 Torr argon pressure.

The x-ray diffraction of the carbon films<sup>175</sup> deposited at 100 Torr helium gas pressure using  $7.8 \times 10^8$  W/cm<sup>2</sup> irradiance of 0.532  $\mu\text{m}$  laser radiation showed peaks at  $10.3^\circ$ ,  $11^\circ$ ,  $17.9^\circ$  and  $21^\circ$  showed the presence of (100), (002), (110) and (112) crystalline planes of C<sub>60</sub>. XRD was done for the carbon films at various helium gas pressures ranging from  $10^{-2}$  to 100 Torr and it was found that these peaks are prominent at 100 Torr only. To further confirm the formation of C<sub>60</sub> clusters, the carbon soot collected from the deposition chamber at various helium gas pressures at  $7.8 \times 10^8$  W/cm<sup>2</sup> fluence of 0.532  $\mu\text{m}$  laser radiation was analyzed using UV-visible and infrared spectroscopy.<sup>132</sup> Figure 53 shows the optical absorption spectrum recorded at room temperature from n-hexane solvable carbon soot in

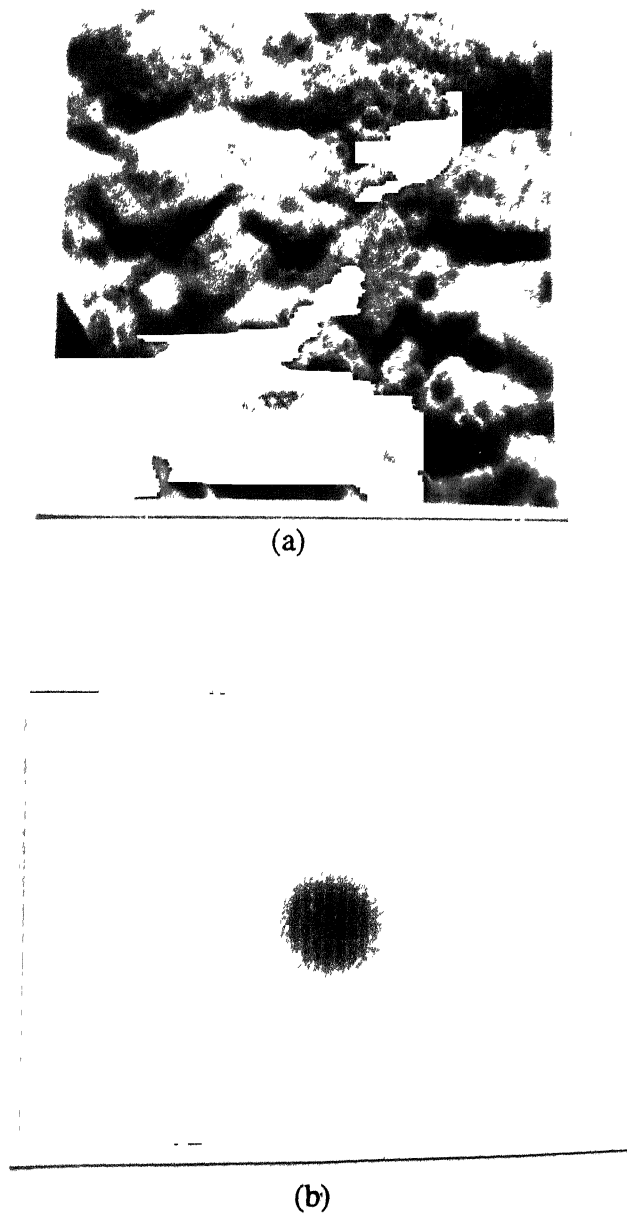


Fig. 51. (a) TEM micrograph and (b) SAED pattern of the film deposited at 1 Torr argon using  $3.8 \times 10^8 \text{ W/cm}^2$  irradiance of  $0.355 \mu\text{m}$  laser wavelength.



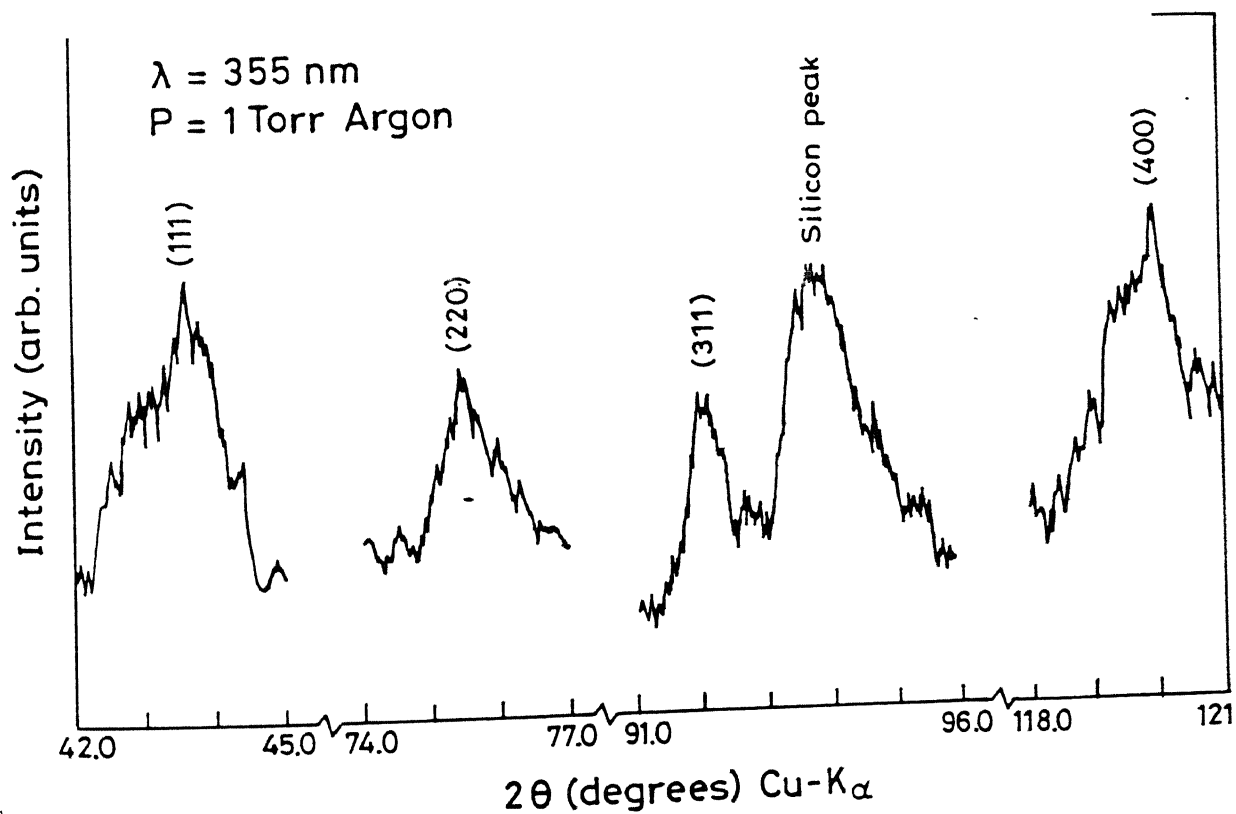


Fig. 52. X-ray diffraction pattern of the carbon film deposited at 1 Torr argon gas pressure at  $3.8 \times 10^8 \text{ W/cm}^2$  irradiance of  $0.355 \mu\text{m}$  laser wavelength. Peaks at  $43.5^\circ$ ,  $76^\circ$ ,  $91.5^\circ$  and  $120^\circ$  show the presence of (111), (220), (311) and (400) crystalline planes of cubic diamond.

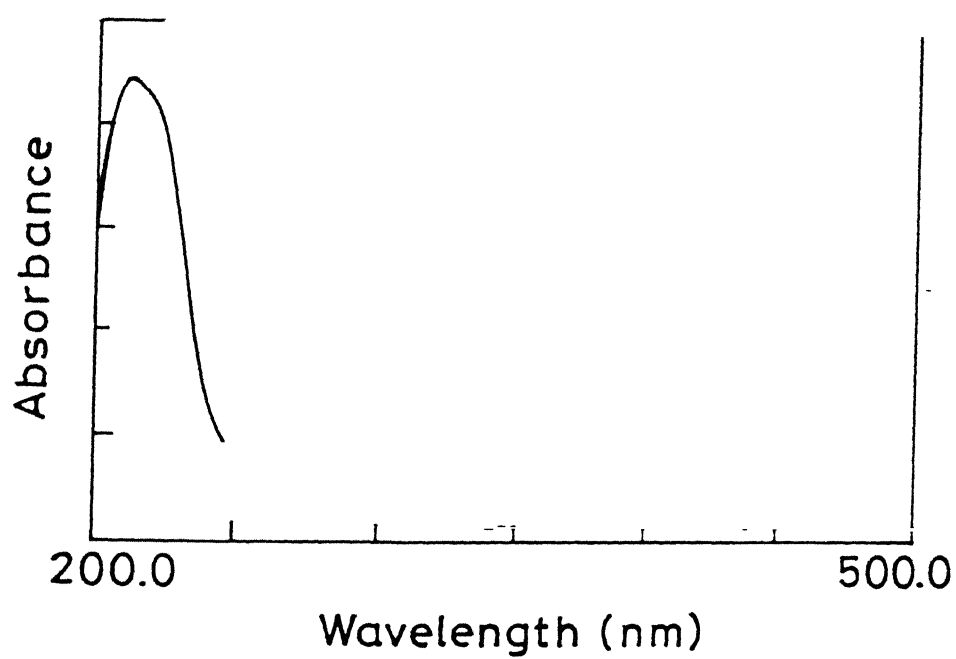


Fig. 53. Optical absorption spectrum in the range 200 - 500 nm.

the range 200-500 nm. The spectra showed peaks around 211, 231, 273, 299, and a broad band at 325 nm. These peaks are characteristic of  $C_{60}$  and  $C_{70}$  clusters.<sup>275</sup> The peak at 231 nm appears as a shoulder to 211 nm. The benzene dissolvable fullerenes were further characterized using vibrational spectroscopy. Since the Raman spectral studies showed very few crystalline domains, we resorted to the method of extracting fullerenes by dissolving the 'soot' in benzene and depositing the aliquots of the benzene extract onto KBr pellets for IR spectroscopy. We did not make any attempt to separate out the clusters as the yield of the benzene soluble clusters was very low, thus an overlapping of many bands in the IR spectra is expected. Figure 54 shows the IR spectra recorded for the soot collected at different helium gas pressures using 0.532  $\mu\text{m}$  laser irradiation. The spectra showed that the modes became more prominent as the helium gas pressure is increased from  $10^{-2}$  to 100 Torr. The modes were observed at 1462, 1126, 739, 701, 670, 651, 575 and 525  $\text{cm}^{-1}$  which could be due to  $C_{60}$  and  $C_{70}$ . The observed bands were identified by comparison with earlier work.<sup>126</sup> In addition, a strong mode at 1720  $\text{cm}^{-1}$  was observed in the IR spectrum, showing the presence of higher fullerenes greater than  $C_{70}$ .

### Micro-Raman Scattering Measurements

Raman spectra is a powerful tool for the analysis of carbon films due to its ability to distinguish different bonding types, domain size and its insensitivity to internal stress. The Raman peak shift, the shape, half width and intensity are the parameters that provide information about the structure of the deposited films. Figure 55 shows the micro-Raman spectra of the deposited films at various argon gas pressures. We observed the presence of two well defined characteristic peaks in the spectrum at 1580  $\text{cm}^{-1}$  (G-line) and 1350  $\text{cm}^{-1}$  (D-line). These peaks have been attributed to polycrystalline graphite and amorphous carbon with graphitic bonding respectively in the literature.<sup>277</sup> However, the characteristic diamond peak at 1332  $\text{cm}^{-1}$  was not seen in Raman spectra. It has been shown by several investigators<sup>215,216</sup> that the large width of 1350  $\text{cm}^{-1}$  band can obscure the peak at 1332  $\text{cm}^{-1}$ . It is important to note that the Raman cross section from non-diamond carbon is approximately 60 times larger than for diamond.<sup>277</sup> Therefore, due to large sensitivity difference nanocrystalline diamond nuclei present in the film may be obscured by the broad non-diamond peak at 1350  $\text{cm}^{-1}$ .

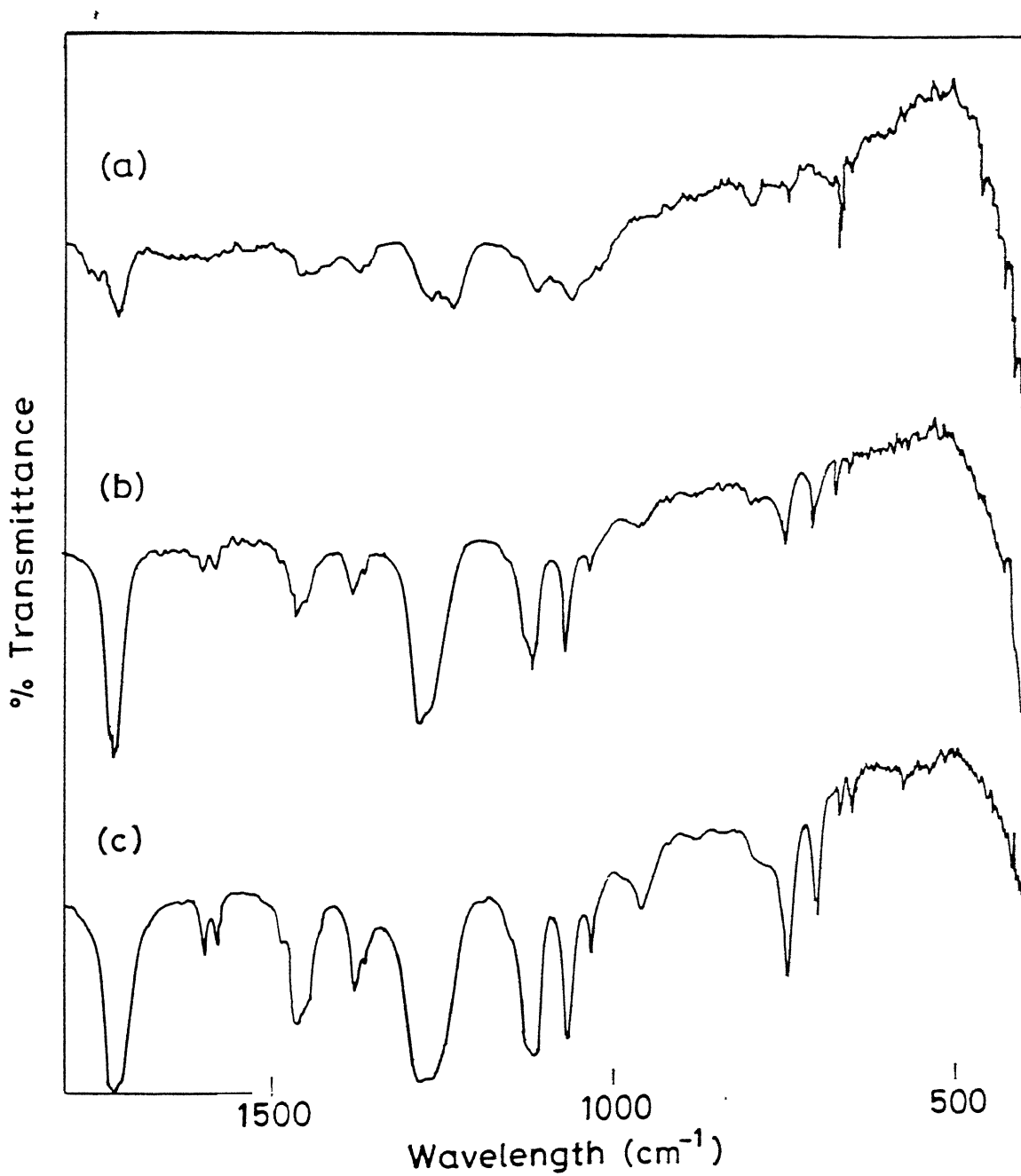


Fig. 54. Infrared spectra of carbon clusters extracted from benzene solvable soot collected at (a)  $10^{-2}$ , (b) 1 and (c) 100 Torr helium pressure.

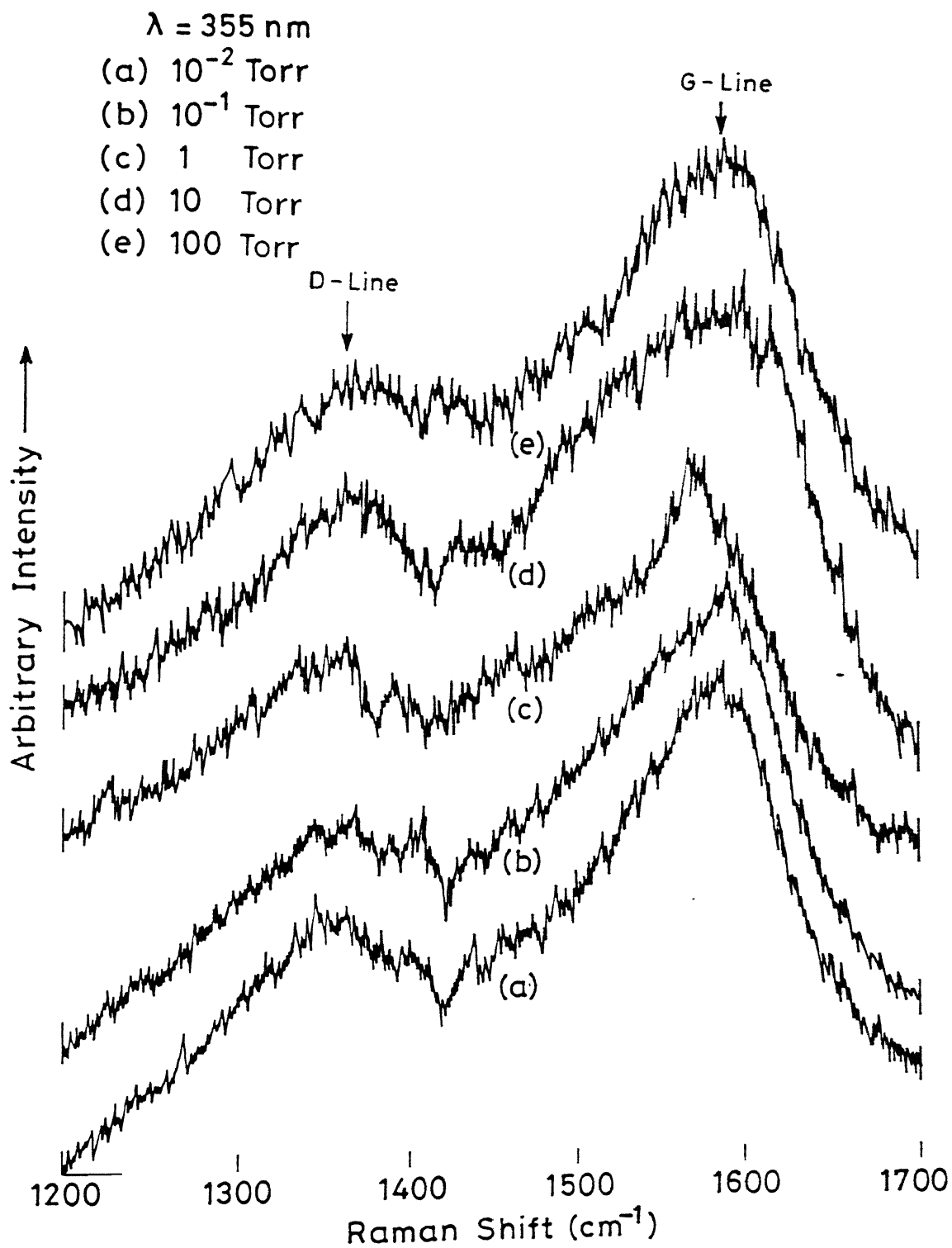


Fig. 55. Micro Raman spectra for carbon films at various argon gas pressures.

Two important features observed in the Raman spectra are: (1) a decrease of D-line to G-line intensity ratio  $I(D)/I(G)$  with the pressure of the argon gas upto 1 Torr but it increases with further increase in argon gas pressure; (2) a downward shift of the G-line for the films deposited at 1 Torr argon gas pressure. Figure 56 shows the  $I(D)/I(G)$  intensity ratio as a function of argon gas pressure. The ratio is found to be at a minimum at 1 Torr of argon gas pressure. It has been shown that the ratio  $I(D)/I(G)$  varies inversely with the size of the graphite crystallites.<sup>278</sup>  $I(D)/I(G)$  being at a minimum at 1 Torr indicates the presence of larger crystallites formed at 1 Torr compared to that formed at other pressures agreeing well with SEM results. The broad G-line shifted to  $1550\text{ cm}^{-1}$  for the film deposited at 1 Torr is a characteristic feature of diamond-like carbon. The width of the Raman lines were also seen to be least for the film deposited at 1 Torr of argon gas pressure. Thus the deposited film has dominance of DLC character at 1 Torr of argon gas.

## Resistivity Measurements

An attempt was made to measure the electrical resistivity of the films deposited on silicon substrates at various argon gas pressures. The resistivity of the film at room temperature was found to be maximum at 1 Torr and decreased at all other pressures. The increase of argon gas pressure to 100 Torr caused a large decrease in resistivity. The relatively larger resistivity of the film at 1 Torr may be the indication of the increase of  $sp^3$  diamond bonds and decrease in the number of  $sp^2$  graphitic bonds in the film.

In order to get some insight into the conduction mechanism, the temperature dependence of the electrical resistivity was studied. Figure 57 shows the temperature dependence of the resistivity of the deposited films at various argon gas pressures. The resistivity of the films did not change at the temperatures below  $0^\circ\text{C}$  irrespective of the argon gas pressure. However, the resistivity decreased with further increase in temperature. The change in the electrical resistivity was strongly dependent on the pressure of the argon gas. The larger resistivity at 1 Torr indicates more dense films at this pressure as compared to other pressure.

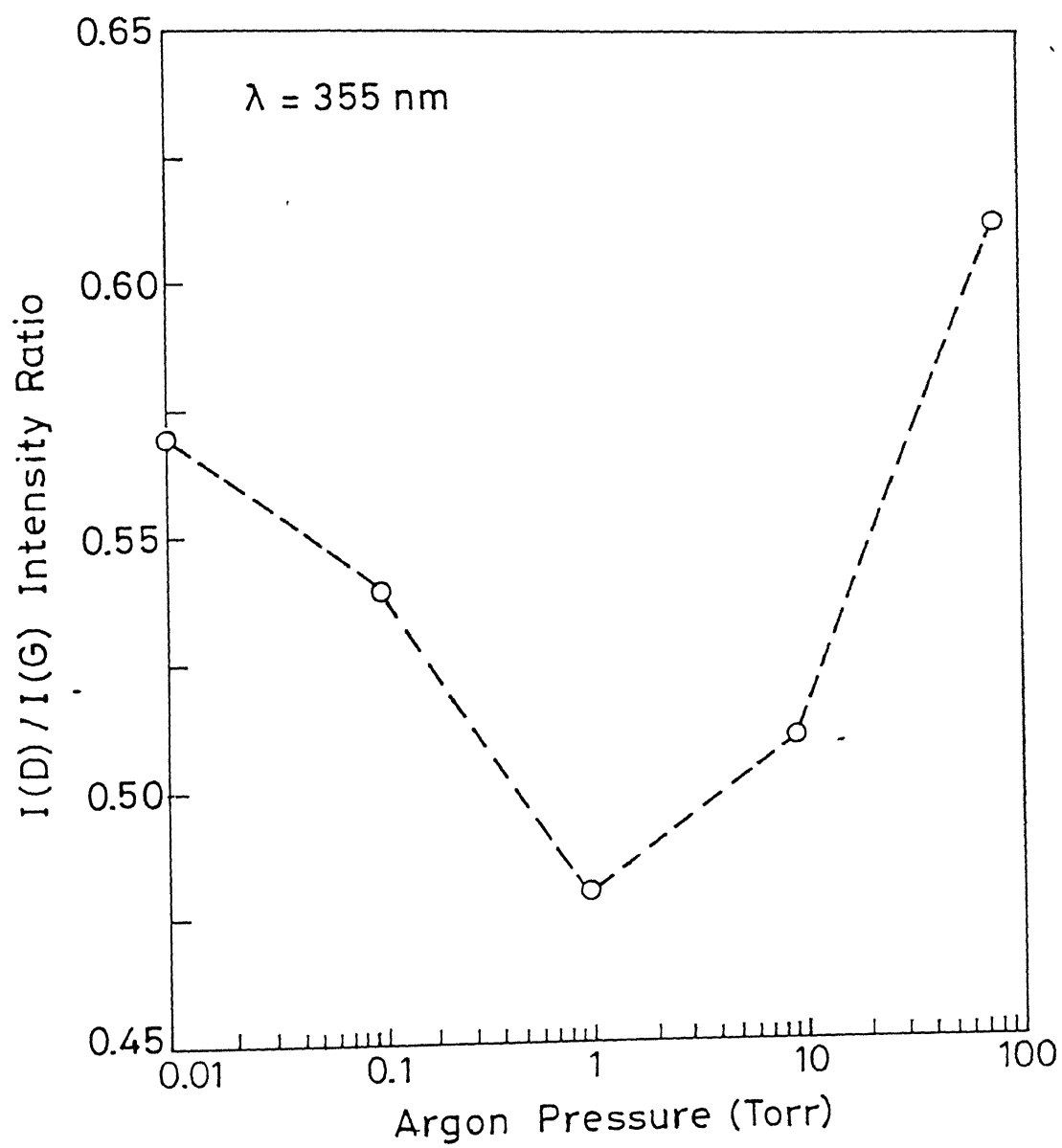


Fig. 56. Intensity ratio  $I(D)/I(G)$  vs argon gas pressure for carbon films. The dotted line is only a guide to the eye.

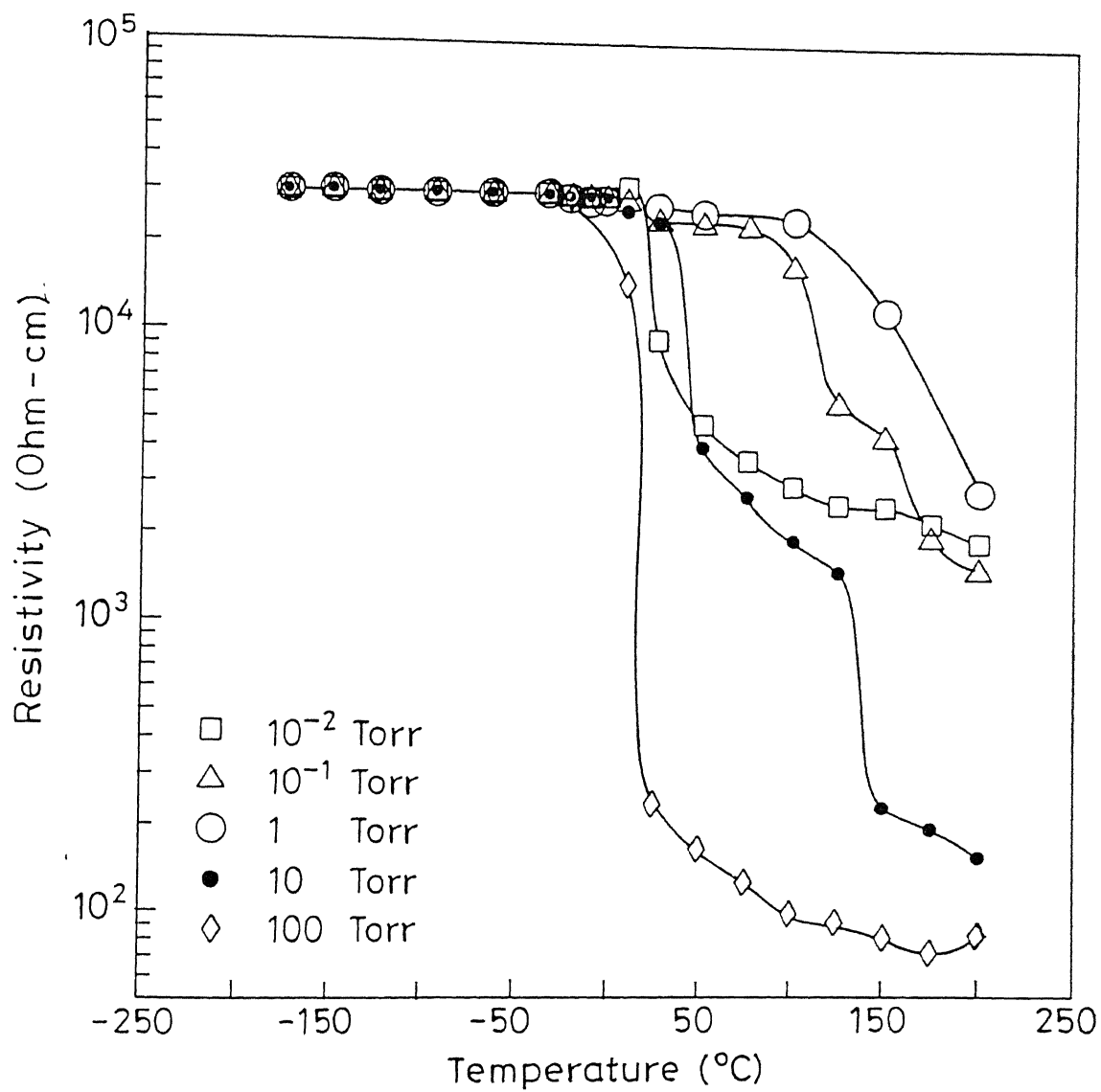


Fig. 57. Temperature dependence of the resistivity of films deposited at various argon gas pressures.



## DISCUSSION

The properties of the film produced by laser ablation deposition depends on the details of the ablation process and nature of the ejected material. Our results on optical emission diagnostics<sup>174,175</sup> and ion probe measurements<sup>85</sup> can be used to understand the characteristics of the deposited film. To correlate we sum up the results, at the cost of being repeated. The optical emission data shows the plasma emission to be dominated by various atomic/ionic species from triply ionized carbon (C IV) to neutral carbon (C I), which recombine through atomic carbon away from the target. The presence of a background gas has a strong influence on plasma expansion process. In general, the interaction between laser plasma and the ambient gas influences the parameters such as velocities of different species in the plume, density and temperature of species which in turn control the characteristics of the deposited film. However, at the low irradiance level used for thin film deposition the optical emission from the plasma plume consists of molecular carbon predominantly. Molecular  $C_2$  which is the critical species for DLC varies with the choice of and pressure of the ambient gas, in addition to various laser parameters such as laser irradiance, laser wavelength etc. The intensity of  $C_2$  Swan bands was found more in presence of argon gas than of helium. It is known that the characteristics of the deposited films are effected by the energy of the species being deposited which in turn is defined by the temperature of the species. Thus the temperature of the dominating species is a crucial parameter defining the characteristics of the film. In order to optimize the film characteristics, the temperature of the dominant  $C_2$  species in the plume was optimized. The vibrational temperature for  $C_2$  species in the presence of helium gas shows that the vibrational temperature decreases with increasing helium gas pressure (Fig. 34). This indicates that the presence of helium gas helps in cooling and clustering of species and in turn increases the dominance of  $C_2$  and higher carbon clusters (fullerenes) with increasing helium gas pressures. The presence of argon gas increased the vibrational temperature of the  $C_2$  species. The vibrational temperature also increased with decrease in laser wavelength. The dependence of vibrational temperature with argon gas pressure showed that the vibrational temperature attains a maximum value at 1 Torr of argon gas then decreases with change of pressure on either side (Fig. 35). It follows that the higher vibrational temperature at 1 Torr argon gas pressure may lead to the fragmentation and ionization of larger clusters formed in the plasma. The fragmentation and

ionization may be attributed to a large number of different processes which include collisional activation, charge exchange, electron collision and multiphoton absorption etc. Although the exact mechanism of the fragmentation and ionization is not known, one or more of these processes may lead to the formation of large number of stable molecular carbon clusters. The increase in the density of molecular carbon clusters in particular  $C_2$  results in the formation of more dense film showing DLC character at 1 Torr of argon gas pressure. Hence it looks from our observation that the vibrational temperature calculated from molecular  $C_2$  emission intensity may be one of the controlling parameters defining the film characteristics. Our conclusions are in agreement with work on the LIF and Langmuir probe diagnostics of the plasma used for diamond film deposition<sup>120</sup> which has shown that  $C_2$  yield essentially defines the diamond like character.

Our ion probe diagnostics results on electron temperature and plasma species density can also be used to understand the deposited films. The growth of the deposited films depend on the cumulative number of plasma species striking the substrate which in turn depends on the density. To examine the angular extent of the ions in the plume, the ion density calculated at various angles with respect to target surface normal at various argon gas pressures were fitted to cosine-function. The reduction in the value of cosine exponent  $p$  with distance at 1 Torr argon suggests that the film deposited at larger distance must be more uniform. However, the variation of electron temperature with distance (Fig. 42) shows that the temperature falls very rapidly beyond 10 mm. Hence the location of the substrate beyond 10 mm would affect the quality of the deposited film due to the fact that the species that reach the substrate will have low energy. The electron temperature at 10 mm from the target surface is found to be maximum at around 1 Torr. Also the electron temperature is found to be maximum along the target surface normal and decreased at other angular positions with respect to target normal. Hence 1 Torr argon gas and 10 mm target-substrate distance along the target surface normal seem to be optimum for depositing DLC films. This implies that the temperature of the plasma is a critical factor for depositing DLC films. The conclusion is further supported by the Raman analysis.

Although the vibrational temperatures of  $C_2$  species obtained using optical emission data and the electron temperatures calculated from ion probe measurements cannot be correlated with each other, however, the enhanced diamond-like character at 1 Torr may be attributed to the higher temperature of the plasma. To understand diamond like carbon,

Tamor and Wu<sup>279</sup> constructed a 'defected graphite' model in which the presence of a small amount of disorder is able to induce localization of  $\pi$  electrons. The disorder consists of randomly distributed defects which can be a carbon vacancy or interplanar links through  $sp^3$  bonding. Recently proposed Cuomo's model<sup>157</sup> have shown that the transition from graphite to diamond requires a reduction in the average atomic distance. Since a large activation barrier exists in going from graphite to diamond, the higher temperature of the plasma may increase the probability of surmounting the barrier giving DLC at 1 Torr argon. Our irradiance used for film deposition also lies in the region where most of the DLC films are produced (Fig. 2,  $\delta$ ).

In conclusion, thin carbon films were deposited on silicon and glass substrates in the presence of helium and argon gas. The deposited film's characteristics are correlated with the properties of the ablated plumes, a source of thin films. The films were characterized using SEM, XRD, TEM, Raman spectroscopy and resistivity measurements. The film deposited in presence of helium gas showed the increasing dominance of  $C_{60}$  with increase in helium gas pressure. However, the films deposited in presence of argon gave the formation of diamond at 1 Torr of the argon gas pressure. The formation of diamond at 1 Torr of argon gas is attributed to the higher temperature of the plasma.

## CHAPTER VI

### CONCLUSIONS

The laser ablated carbon plumes for thin film deposition were studied in vacuum and in presence of helium and argon gas at low and high irradiances. A Q-switched Nd:YAG laser and its harmonics ( $\lambda = 1.064, 0.532, 0.355$  and  $0.266 \mu\text{m}$ ) were used to generate the carbon plume. Optical emission diagnostics of the plasma plume used for carbon film deposition was carried out as a function of distance from the target surface, laser energy, laser wavelength and ambient gas pressure. Ion probe diagnostics was performed at various distances from the target surface, angle with respect to the target surface normal and argon gas pressure using  $0.355 \mu\text{m}$  laser radiation. A hydrodynamic model for LAD of carbon in an ambient atmosphere is discussed. Thin carbon films were deposited on silicon and glass substrates in helium and argon gas atmosphere. Various diagnostics such as SEM, XRD, TEM, SAED, micro-Raman spectroscopy and resistivity measurements were employed to characterize the deposited films.

Using the hydrodynamic model for laser ablation deposition various plasma parameters as plasma temperature, plasma density and velocity are estimated. It is shown that the plasma dimensions give larger elongation along the target normal as compared to other directions with increase in time. The expansion velocity in vacuum increases with time and becomes constant. In presence of an ambient gas the velocity after becoming constant decreases beyond some distance from the target surface. The distance after which the expansion velocity of the plasma decreases is dependent on ambient pressure. The thickness of the film calculated decreases with increase in distance from the target surface.

The optical emission diagnostics of the plasma plume used for thin carbon films deposition showed the plasma emission to be dominated by various atomic/ionic species from C I to C IV at higher laser intensities. Electron temperature of the plasma estimated using emission lines intensity ratio of C II species assuming the plasma to be in local thermodynamic equilibrium was found to be in the range 1-9 eV. The electron density calculated using Stark width of C II transition  $3p^2P^0 - 4s^2S$  at 392.0 nm in ambient atmosphere at various distances from the target surface lies between  $10^{16} - 10^{18} \text{ cm}^{-3}$ . The expansion velocity of the plasma was estimated using temporal profiles of C II transition.

The velocity of the plasma decreases in the presence of ambient gas. At low laser intensities the plasma emission was dominated by molecular carbon in  $\Delta v = -2, -1, 0, +1, +2$  sequence of Swan ( $d^1\pi_g - d^1\pi_u$ ) bands and  $\Delta v = 0$  and 1 sequence of Deslandres-d'Azambuja ( $C^1\pi_g - A^1\pi_g$ ) bands. A detailed study of optical emission spectra of  $C_2$  was carried out as  $C_2$  plays a major role in the formation of diamond like carbon film deposition and generation of stable carbon clusters (fullerenes).  $C_2$  emission studies were performed at various laser energies, wavelengths and various helium and argon gas pressures ranging from  $10^{-3}$  to 100 Torr.  $C_2$  band head intensity was found to be optimum at an intermediate energy. The intensity of  $C_2$  band heads increased in the presence of ambient gas, however, the enhancement was seen to be larger in presence of argon than that of helium. It is shown that the temperature of the dominant species is a critical parameter in determining the diamond like carbon character.  $C_2$  Swan band head intensities were used to calculate the vibrational temperatures at various laser energies, wavelengths and helium and argon gas pressures. Vibrational temperature increases with decrease in laser wavelengths and it was found to be optimum at an intermediate energy. The presence of helium gas helps in cooling and clustering of molecular species. In presence of argon gas background the vibrational temperature was seen to be maximum at 1 Torr pressure and decreased with change of pressure on either side. The vibrational temperature was also found to be more in presence of argon than that of helium. The temporal profiles of  $C_2$  at 516.5 nm showed a two component character in presence of helium gas beyond a certain distance from the target surface. The fast component travelled at nearly vacuum speed and the delayed component is seen to follow blast wave model which shows a shock wave disturbance through the gas.

Ion probe measurements of the carbon plume were carried out at various distances from the target surface, various angles with respect to target surface normal at various argon gas pressures from  $10^{-3}$  - 100 Torr using 0.355  $\mu m$  laser wavelength. At 1 Torr of argon gas pressure the electron temperature was found to be larger than that in vacuum upto 10 mm but became close to that in vacuum at larger distances. The electron temperature was found to be maximum along the target surface normal and decreases with increase in angle. The electron temperature was found to be maximum at 1 Torr of argon gas. The ion density was found maximum along target surface normal for the argon gas pressures  $\geq 1$  Torr. The exponent of the fitted cosine function to the density and temperature showed strong dependence on the ambient gas pressure. The value of the exponent decreased in presence of argon gas and was

at its maximum at 1 Torr of argon gas pressure. The velocity of the ions calculated using ion probe signals decreased with increase in argon gas pressure.

Carbon thin films were deposited on silicon and glass substrates in presence of helium and argon gas pressures. SEM micrographs of the film deposited in presence of helium gas showed that the density of the microcrystalline clusters increases with increase in helium pressure. XRD pattern of the film at 100 Torr helium gas pressure showed peaks at  $10.3^{\circ}$ ,  $11^{\circ}$ ,  $17.9^{\circ}$  and  $20^{\circ}$  confirming the presence of (100), (002), (110) and (112) crystalline planes of  $C_{60}$ . The ablated carbon powder "soot" collected from the deposition chamber at various helium gas pressures was investigated using IR and UV-visible spectroscopy to confirm the presence of  $C_{60}$ . The optical absorption spectra showed peaks around 211, 231, 273, 299 and a broad peak at 325 nm which are the characteristic of  $C_{60}$  and  $C_{70}$ . Prominent IR modes at 1462, 1126, 739, 701, 670, 651, 575 and  $525\text{ cm}^{-1}$  in the infrared spectrum showed the presence of  $C_{60}$  and  $C_{70}$ . The SEM images for the deposited films in presence of argon gas showed the density of microcrystalline clusters on the surface of the films to be maximum at 1 Torr pressure. The XRD pattern of the film deposited at 1 Torr of argon gas pressure showed peaks at  $43.5^{\circ}$ ,  $76^{\circ}$ ,  $91.5^{\circ}$  and  $120^{\circ}$  corresponding to (111), (220), (311) and (400) crystalline planes of cubic diamond. The  $d_{\text{lattice}}$  - spacing calculated from the SAED pattern of the film deposited at 1 Torr matched with that of diamond. The micro-Raman spectra of the deposited films in argon atmosphere showed the presence of G-peak ( $1580\text{ cm}^{-1}$ ) and D-peak ( $1350\text{ cm}^{-1}$ ). The broad G-line shifted to  $1550\text{ cm}^{-1}$  for the film deposited at 1 Torr, a characteristic feature of diamond-like carbon. The D-line to G-line intensity ratio  $I(D)/I(G)$  was strongly dependent on argon gas pressure and found to be least for the film deposited at 1 Torr. The temperature dependence of the resistivity of the films was also investigated. The resistivity of the film deposited at 1 Torr of argon was larger than that for the film deposited at other pressures. The larger resistivity at 1 Torr is attributed to the increase of diamond  $sp^3$  bonds and decrease of graphitic  $sp^2$  bonds at that pressure.

## Future Scope of the Work

We measured the vibrational temperature using  $C_2$  Swan band head intensities. Laser induced fluorescence and absorption spectroscopy can be utilized using a tunable dye laser as a probe beam to estimate the density and temperature.

We deposited the films in helium and argon atmospheres at room temperature. No attempt was made to deposit the films on heated or biased substrates. The deposition of the films on heated / biased substrates at various ambient pressures may help to optimize the parameters for diamond like carbon film deposition. Specific applications of the deposited films require different substrate materials. The deposition can be tried on various substrates to study their possible role in thin film growth.

We characterized the deposited films using SEM, XRD, TEM, micro-Raman and resistivity measurements. Surface morphology of the deposited films can also be studied using Scanning Tunneling Microscopy (STM), Atomic Force Microscopy (AFM) etc. to determine their role for device applications. Further diagnostics for characterizing the films such as hardness, IR transparency,  $sp^3/sp^2$  ratio, band gap, frictional coefficients etc., can be tried to have a better understanding of the films for various technological applications.

A detailed investigation of the evolution of shock waves while propagation of laser ablated carbon plume in ambient atmosphere may be carried out. For laser ablation deposition ambient pressure must be kept such that some of the ablated species reach the substrate irrespective of background shock wave. The formation of shock waves may be studied using fast photography and imaging. These studies will help in optimizing the target substrate distance and ambient pressure for getting good quality films.

## REFERENCES

1. F. Lopez and E. Bernabeu, *Thin Solid Films* **191**, 13 (1990).
2. D. K. Lathrop, S. E. Russek and R. A. Buhrman, *Appl. Phys. Lett.* **51**, 1554 (1987).
3. G. Wagner, E. G. Gonzales, K. Numssen and H. -U. Habermeier, *Physica C* **235**, 637 (1994).
4. C. Wyon, R. Gillet and L. Lombard, *Thin Solid Films* **122**, 203 (1984).
5. J. C. Angus, J. E. Schultz, P. J. Shiller, J. R. MacDonald, M. J. Mirtich and S. Dowitz, *Thin Solid Films* **118**, 311 (1984).
6. W. M. Lau, I. Bello, X. Feng, L. J. Huang, Q. Fuguang, Y. Zhenyu, R. Zhizhang and S. -T. Lee, *J. Appl. Phys.* **70**, 5623 (1991).
7. E. Grossman, G. D. Lempert, J. Kulik, D. Marton, J. W. Rabalais and Y. Lifshitz, *Appl. Phys. Lett.* **68**, 1214 (1996).
8. X. Queralt, C. Ferrater, F. Sanchez, R. Aguiar, J. Palau and M. Varela, *Appl. Surf. Sci.* **86**, 95 (1995).
9. I. P. Llewellyn, N. Rimmer, G. A. Scarsbrook and R. A. Heinecke, *Thin solid films* **191**, 135 (1990).
10. J. Narayan, A. R. Srivatsa, M. Peters, S. Yokota and K. V. Ravi, *Appl. Phys. Lett.* **53**, 1823 (1988).
11. K. Kitahama, *Appl. Phys. Lett.* **53**, 1812 (1988).
12. J. Kwo, M. Hong, D. J. Trevor, R. M. Fleming, A. E. White, R. C. Garrow, A. R. Kortan and K. T. Short, *Appl. Phys. Lett.* **53**, 2683 (1988).
13. D. B. Chrisey and G. K. Hubler, *Pulsed Laser Deposition of Thin Films*, (John Wiley, New York, 1994).
14. H. M. Smith and A. F. Turner, *Appl. Opt.* **4**, 147 (1965).
15. J. F. Ready, *Effects of High Power Laser Radiation* (Academic, New York, 1971).
16. R. E. Muenchausen, K. M. Hubbard, S. Foltyn, R. C. Estler, N. S. Nogar and C. Jenkins, *Appl. Phys. Lett.* **56**, 578 (1990).
17. H. Kidoh, A. Morimoto and T. Shimizu, *Appl. Phys. Lett.* **59**, 237 (1991).
18. R. P. van Ingen, R. H. J. Fastenau and E. J. Mittemeijer, *J. Appl. Phys.* **76**, 1871 (1994).



19. I. N. Mihailescu, N. Chitica, L. C. Nistor, M. Popescu, V. S. Teodorescu, I. Ursu, A. Andrei, A. Barborica, A. Luches, M. Luisa De Giorgi, A. Perrone, B. Dubreuil and J. Hermann, *J. Appl. Phys.* **74**, 5781 (1993).
20. G. Koren, R. J. Baseman, A. Gupta, M. I. Lutwyche and R. B. Laibwitz, *Appl. Phys. Lett.* **56**, 2144 (1990).
21. V. Berardi, S. Amoroso, N. Spinelli, M. Armenante, R. Velotta, F. Fuso, M. Allegrini and E. Arimondo, *J. Appl. Phys.* **76**, 8077 (1994).
22. E. W. Kreutz, A. Voss, M. Alunovic, J. Funken and H. Sung, *Surf. Coat. Technol.* **59**, 26 (1993).
23. T. P. Huges, *Plasmas and Laser Light* (Wiley, New York, 1975).
24. J. C. Miller and R. F. Haglund, Jr., *Laser Ablation* (Springer Verlag, Berlin, 1991).
25. R. K. Singh and J. Narayan, *Phys. Rev. B* **41**, 8843 (1990).
26. A. A. Voevodin, S. D. Walck, J. S. Solomon, P. J. John, D. C. Ingram, M. S. Donley and J. S. Zabinsky, *J. Vac. Sci. Technol. A* **14**, 1927 (1996).
27. S. Leppävuori, J. Levoska, J. Vaara and O. Kusmartseva, *Mat. Res. Soc. Symp. Proc.* **285**, 557 (1993).
28. C. Champeaux, P. Marchet, J. Aubreton, J.-P. Mercurio and A. Catherinot, *Appl. Surf. Sci.* **69**, 335 (1993).
29. O. Auciello, *Materials and Manufacturing Process* **6**, 33 (1991).
30. H.-U. Krebs and O. Bremert, *Appl. Phys. Lett.* **62**, 2341 (1993).
31. A. M. Widdowson, T. J. Jackson, R. Allott, I. C. E. Turcu, S. B. Palmer and C. McCoard, *RAL Report # TR - 96-066*, 172 (1995-96).
32. J. G. Lunney, *Appl. Surf. Sci.* **86**, 79 (1995).
33. E. Dyer and R.-J. Farlay, *J. Appl. Phys.* **74**, 1442 (1993).
34. G. B. Blanchet, *Appl. Phys. Lett.* **62**, 479 (1993).
35. L. J. Radziemski and D. A. Cremers, *Laser-induced Plasmas and Applications* (Marcel Dekker, Inc., New York, 1989).
36. E. A. Rohlfing, D. M. Cox and A. Kaldor, *J. Chem. Phys.* **81**, 3322 (1984).
37. U. Naher, H. Göhlich, T. Lange and T. P. Martin, *Phys. Rev. Lett.* **68**, 3416 (1992).
38. R. E. Leuchtner, A. C. Harms and A. W. Castleman, Jr., *J. Chem. Phys.* **94**, 1093 (1991).

39. D. E. Powers, S. G. Hansen, M. E. Geusic, D. L. Michalopoulos and R. E. Smalley, *J. Chem. Phys.* **78**, 2866 (1983).
40. T. Yoshida, S. Takeyama, Y. Yamada and K. Mutoh, *Appl. Phys. Lett.* **68**, 1772 (1996).
41. R. W. Dreyfus, R. Kelly and R. E. Walkup and R. Srinivasan, *SPIE* **710**, 46 (1986).
42. B. Soom, H. Chen, Y. Fisher and D. D. Meyerhofer, *J. Appl. Phys.* **74**, 5372 (1993).
43. G. Mehlman, D. B. Chrisey, P. G. Burkhalter, J. S. Horwitz and D. A. Newman, *J. Appl. Phys.* **74**, 53 (1993).
44. N. G. Utterback, S. P. Tang and J. F. Friichtenicht, *Phys. Fluids* **19**, 900 (1976).
45. B. C. Boland, F. E. Irons and R. W. P. McWhirter, *J. Phys.* **B 1**, 1180 (1968).
46. F. E. Irons, R. W. P. McWhirter and N. J. Peacock, *J. Phys. B: Atom. Molec. Phys.* **5**, 1975 (1972).
47. C. Steden and H. -J. Kunze, *Phys. Lett. A* **151**, 534 (1990).
48. R. Tambay and R. K. Thareja, *IEEE J. Quant. Electron.* **31**, 743 (1995).
49. F. E. Irons and N. J. Peacock, *J. Phys.* **B 7**, 2084 (1974).
50. P. E. Dyer, P. H. Key, D. Sands, H. V. Snelling and F. X. Wagner, *Appl. Surf. Sci.* **86**, 18 (1995).
51. L. Z. Barabash, Yu. A. Bykovskii, A. A. Golubev, D. G. Kosyrev, K. I. Krechet, Yu. I. Lapitskii, S. V. Latyshev, R. T. Haydarov, B. U. Sharkov and A. V. Shumshirov, *Laser and Part. Beams* **2**, 49 (1984).
52. R. H. Dixon and R. C. Elton, *Phys. Rev. Lett.* **38**, 1072 (1977).
53. D. B. Geohegan, A. A. Puretzky, R. L. Hettich, X. -Y. Zheng, R. E. Haufter and R. N. Compton, *Trans. Mat. Res. Soc. Jpn.* **17**, 349 (1994).
54. R. K. Thareja, Abhilasha and R. K. Dwivedi, *Laser and Part. Beams* **13**, 481 (1995).
55. D. B. Geohegan and A. A. Puretzsky, *Mat. Res. Soc. Symp. Proc.* **388**, 21 (1995).
56. J. Farny, S. Nagraba and E. Woryna, *J. Tech. Phys.* **28**, 185 (1987).
57. R. R. Goforth and D. W. Koopman, *Phys. Fluids* **17**, 698 (1974).
58. Abhilasha, P. S. R. Prasad and R. K. Thareja, *Phys. Rev. E* **48**, 2929 (1993).
59. T. Kerdja, S. Abdelli, D. Ghobrini and S. Malek, *J. Appl. Phys.* **80**, 5365 (1996).

60. V. Yu. Baranov, O. N. Derkach, V. G. Grishina, M. F. Kanevskii and A. Yu. Sebrant, *Phys. Rev. E* **48**, 1324 (1993).
61. J. N. Broughton and R. Fedosejevs, *J. Appl. Phys.* **74**, 3712 (1993).
62. K. Mann and K. Rohr, *Laser and Particle Beams* **10**, 435 (1992).
63. J. C. S. Kools and J. Dieleman, *J. Appl. Phys.* **74**, 4163 (1993).
64. D. K. Zerkle and A. D. Sappey, *IEEE Trans. Plasma Sci.* **24**, 37 (1996).
65. H. F. Sakeek, T. Morrow, W. G. Graham and D. G. Walmsley, *J. Appl. Phys.* **75**, 1138 (1994).
66. C. Cali, F. La Rosa, G. Targia and D. Robba, *J. Appl. Phys.* **78**, 6265 (1995).
67. A. H. El-Astal and T. Morrow, *J. Appl. Phys.* **80**, 1156 (1996).
68. N. H. Cheung, Q. Y. Ying, J. P. Zheng and H. S. Kwok, *J. Appl. Phys.* **69**, 6349 (1991).
69. R. Tambay, R. Singh and R. K. Thareja, *J. Appl. Phys.* **72**, 1197 (1992).
70. I. Olivares and H. J. Kunze, *Phys. Rev. E* **47**, 2006 (1993).
71. F. Fuso, L. N. Vyacheslavov, G. Masciarelli and E. Arimondo, *J. Appl. Phys.* **76**, 8088 (1994).
72. R. A. Al-Wazzan, C. L. S. Lewis and T. Morrow, *Rev. Sci. Instrum.* **67**, 85 (1996).
73. P. A. Naik, P. D. Gupta and S. P. Kumbhare, *Phys. Rev. A* **43**, 4540 (1991).
74. C. Timmer, S. K. Srivastava, T. E. Hall and A. F. Fucaloro, *J. Appl. Phys.* **70**, 1888 (1991).
75. H. P. Gu, Q. H. Lou, N. H. Cheung, S. C. Chen, Z. Y. Wang and P. K. Lin, *Appl. Phys. B* **58**, 143 (1994).
76. Abhilasha and R. K. Thareja, *Appl. Phys. B* **60**, 63 (1995).
77. S. Witanachchi and P. Mukherjee, *J. Appl. Phys.* **78**, 4099 (1995).
78. O. B. Anan'in, Yu. A. Bykovskii, Yu. V. Eremin, E. L. Stupitskii, I. K. Novikov and S. P. Frolov, *Sov. J. Quant. Electron.* **21**, 787 (1991).
79. D. B. Geohegan and A. A. Puretzsky, *Appl. Phys. Lett.* **67**, 197 (1995).
80. Y. Nakata, H. Kaibara, T. Okada and M. Maeda, *J. Appl. Phys.* **80**, 2458 (1996).
81. A. Neogi, A. Mishra and R. K. Thareja, *J. Appl. Phys.*, Submitted (1997).
82. A. A. Voevodin, S. J. P. Laube, S. D. Walck, J. S. Solomon, M. S. Donley and J. S. Zabinsky, *J. Appl. Phys.* **78**, 4123 (1995).

83. D. Luben, S. A. Barnett, K. Suzuki, S. Gorbatkin and J. E. Greene, *J. Vac. Sci. Technol.* **B3**, 968 (1985).
84. D. Miu, C. Grigoriu, D. Dragulinescu and I. Chis, *Opt. Eng.* **35**, 1325 (1996).
85. R. K. Dwivedi, S. P. Singh and R. K. Thareja, *J. Appl. Phys.*, Submitted (1997).
86. R. K. Singh, O. W. Holland and J. Narayan, *J. Appl. Phys.* **68**, 233 (1990).
87. J. J. McFarlane, G. A. Moses and R. R. Peterson, *Phys. Fluids* **B 1**, 635 (1989).
88. J. Grun, J. Stamper, C. Manka, J. Resnick, R. Burris, J. Crawford and B. H. Ripin, *Phys. Rev. Lett.* **66**, 2738 (1991).
89. R. G. Tuckfield and F. Schwirzke, *Plasma Phys.* **11**, 11 (1969).
90. G. Dimonte and L. G. Wiley, *Phys. Rev. Lett.* **67**, 1755 (1991).
91. A. Neogi and R. K. Thareja, Private Communication (1997).
92. L. Dirnberger, P. E. Dyer, S. R. Farrar and P. H. Key, in *AIP Conference Proceedings* 288, edited J. C. Miller and D. B. Geohegan (AIP, New York, 1994) pp 349.
93. A. Namiki, T. Kawai and K. Ichige, *Surf. Sci.* **166**, 129 (1986).
94. R. A. Neifeld, S. Gunapala, C. Liang, S. A. Shaheen, M. Croft, J. Price, D. Simons and W. T. Hill, III, *Appl. Phys. Lett.* **53**, 703 (1988).
95. H. -J. Scheibe, A. A. Gorbunov, G. K. Baranova, N. V. Klassen, V. I. Konov, M. P. Kulakov, W. Pompe, A. M. Prokhorov and H. -J. Weiss, *Thin Solid films* **189**, 283 (1990).
96. M. C. Foote, B. B. Jones, B. D. Hunt, J. B. Barner, R. P. Vasquez and L. J. Bajuk, *Physica C* **201**, 176 (1992).
97. S. G. Hansen and T. E. Robitaille, *Appl. Phys. Lett.* **50**, 359 (1987).
98. K. L. Saenger, in *Pulsed Laser Deposition of Thin Films* edited by D. B. Chrisey and G. K. Hubler, (John Wiley, New York, 1994), pp 199.
99. C. Z. Wang and K. M. Ho, *Phys. Rev. Lett.* **71**, 1184 (1993).
100. Z. F. Li, Z. Y. Yang and R. F. Xiao, *J. Appl. Phys.* **80**, 5398 (1996).
101. M. Hanabusa and K. Tsujihara, *J. Appl. Phys.* **78**, 4267 (1995).
102. P. R. Chalker in *Diamond and Diamond-Like films and Coatings* edited by R. E. Clausing, L. L. Horton, J. C. Angus and P. Koidi (Plenum Press, New York, 1991) pp 127.
103. H. Tsai and D. B. Bogy, *J. Vac. Sci. Technol.* **A 5**, 3287 (1987).

104. H. Park, Y. -K. Hong, J. S. Kim, C. Park and J. K. Kim, *Appl. Phys. Lett.* **69**, 779 (1996).
105. M. E. Kozlov, P. Fons, H. -A. Durand, K. Nozaki, M. Tokumoto, K. Yase and N. Minami, *J. Appl. Phys.* **80**, 1182 (1996).
106. E. B. D. Bourdon, W. W. Duley, A. P. Jones and R. H. Prince, in *Diamond and Diamond-Like films and Coatings*, edited by R. E. Clausing et al, (Plenum Press, New York, 1991) pp 297.
107. D. L. Pappas, K. L. Saenger, J. Bruley, W. Krakow, J. J. Cuomo, T. Gu, and R. W. Collins, *J. Appl. Phys.* **71**, 5675 (1992).
108. Y. A. Bukovsky, Ye. V. Charyshkin, V. P. Korlenkov and I. N. Nikolaev, *Spectrochimica Acta* **46A**, 517 (1990).
109. F. Xiang and R. P. H. Chang, in *Novel Forms of Carbon*, edited by C. L. Renschler, J. J. Pouch and D. M. Cox, *Mat. Res. Soc. Symp. Proc.* **270**, 451 (1992).
110. R. K. Thareja and R. K. Dwivedi, *Phys. Lett. A* **222**, 199 (1996).
111. Abhilasha and R. K. Thareja, *Phys. Lett. A* **184**, 99 (1993).
112. R. K. Thareja and Abhilasha, *J. Chem. Phys.* **100**, 4019 (1994).
113. Abhilasha, R. K. Dwivedi and R. K. Thareja, *J. Appl. Phys.* **75**, 8237 (1994).
114. X. Chen, J. Mazumdar and A. Purohit, *Appl. Phys. A* **52**, 328 (1991).
115. D. M. Gruen, S. Liu, A. R. Krauss and X. Pan, *J. Appl. Phys.* **75**, 1758 (1994).
116. J. Seth, R. Padiyath and S. V. Babu, *Appl. Phys. Lett.* **63**, 126 (1993).
117. J. T. McKinley, A. Ueda, R. G. Albridge, A. V. Barnes, N. H. Tolk, J. L. Davidson and M. L. Languell, in *AIP Conference Proceedings* 288, edited by J. C. Miller and D. B. Geohegan (AIP, New York, 1994) pp 70.
118. G. Herzberg, A. Langerquist and C. Malberg, *Can. J. Phys.* **47**, 2734 (1969).
119. M. I. Savadatti and K. S. Kini, *Ind. J. Pure Appl. Phys.* **10**, 890 (1972).
120. D. L. Pappas, K. L. Saenger, J. J. Cuomo and R. W. Dreyfus, *J. Appl. Phys.* **72**, 3966 (1992).
121. E. A. Rohlfing, *J. Chem. Phys.* **89**, 6103 (1988).
122. A. A. Puretzsky, D. B. Geohegan, R. E. Haufler, R. L. Hettich, X. -Y. Zheng and R. N. Compton, in *Laser Ablation : Mechanisms and Applications-II*, edited by J. C. Miller and D. B. Geohegan (AIP Press, New York, 1994), pp 365.
123. G. Koren and J. T. C. Yeh, *J. Appl. Phys.* **56**, 2120 (1984).

124. R. W. Dreyfus, *J. Appl. Phys.* **69**, 1721 (1991).
125. H. W. Kroto, J. R. Heath, S. C. O'Brien, R. F. Curl and R. E. Smalley, *Nature* **318**, 162 (1985).
126. W. Krätschmer, L. D. Lamb, K. Fostiropoulos and D. R. Huffman, *Nature* **347**, 354 (1990).
127. A. F. Hebard, M. J. Rosseinsky, R. C. Haddon, D. W. Murphy, S. H. Glarum, T. T. M. Palstra, A. P. Ramirez and A. R. Kortan, *Nature* **350**, 600 (1991).
128. H. Yonehara and C. Pac, *Appl. Phys. Lett.* **61**, 575 (1992).
129. W. R. Creasy and J. T. Brenna, *J. Chem. Phys.* **92**, 2269 (1990).
130. P. S. R. Prasad, Abhilasha and R. K. Thareja, *Phys. Status Solidi A* **139**, K1 (1993).
131. G. Meijer and D. S. Bethune, *J. Chem. Phys.* **93**, 7800 (1990).
132. R. K. Thareja, R. K. Dwivedi and Abhilasha, *Phys. Rev. B* **55**, 2600 (1997).
133. D. M. Gruen, S. Liu, A. R. Krauss, J. Luo and X. Pan, *Appl. Phys. Lett.* **64**, 1502 (1994).
134. H. Koinuma, M. -S. Kim and M. Y. Yoshimoto, *Jpn. J. Appl. Phys.* **34**, 3720 (1995).
135. A. McKellar, *Astron. J.* **65**, 350 (1960).
136. P. P. Radi, T. L. Bunn, P. R. Kemper, M. E. Molchan and M. T. Bowers, *J. Chem. Phys.* **88**, 2809 (1988).
137. J. M. L. Martin, J. P. Francois and R. Gijbels, *J. Chem. Phys.* **93**, 8850 (1990).
138. F. Diederich and R. L. Whetten, *Acc. Chem. Res.* **25**, 119 (1992).
139. M. Manfredini, C. E. Bottani and P. Milani, *J. Appl. Phys.* **78**, 5945 (1995).
140. A. A. Kolomenskii, M. Szabadi and P. Hess, *Appl. Surf. Sci.* **86**, 591 (1995).
141. T. Wakabayashi and Y. Achiba, *Chem. Phys. Lett.* **190**, 465 (1992).
142. T. Weiske, D. K. Böhme, J. Hrusak, W. Kratschmer and H. Schwarz, *Angew. Chem. Int. Ed. Engl.* **30**, 884 (1991).
143. T. Weiske, J. Hrusak, D. K. Böhme and H. Schwarz, *Chem. Phys. Lett.* **186**, 459 (1991).
144. A. Kühle, J. L. Skov, S. Hjorth, I. Rasmussen and J. B. Hansen, *Appl. Phys. Lett.* **64**, 3178 (1994).
145. H. S. Kim and H. S. Kwok, *Appl. Phys. Lett.* **61**, 2234 (1992).

146. E. J. Tarsa, E. A. Hachfeld, F. T. Quinlan, J. S. Speck and M. Eddy, *Appl. Phys. Lett.* **68**, 490 (1996).
147. J. W. McCamy and D. H. Lowndes, in *Laser Ablation: Mechanisms and Applications*, edited by J. C. Miller and D. B. Geohegan (AIP Press, New York, 1994), pp 215.
148. G. Koren, A. Gupta, R. J. Baseman, M. I. Lutwyche and R. B. Laibowitz, *Appl. Phys. Lett.* **55**, 2450 (1989).
149. W. Kautek, B. Roas and L. Schultz, *Thin Solid Films* **191**, 317 (1990).
150. P. T. Murray and D. T. Peeler, in *AIP Conference Proceedings* 288, edited J. C. Miller and D. B. Geohegan (AIP, New York, 1994) pp 359.
151. J. Krishnaswamy, A. Rengan, J. Narayan, K. Vedam and C. J. McHargue, *Appl. Phys. Lett.* **54**, 2455 (1989).
152. S. Fujimori, T. Kasai and T. Inamura, *Thin Solid Films* **92**, 71 (1982).
153. A. P. Malshe, S. M. Chaudhari, S. M. Kanetkar, S. B. Oagle, S. V. Rajarshi and S. T. Kshirsagar, *J. Mater. Res.* **4**, 1238 (1989).
154. F. Qian, R. K. Singh, S. K. Dutta and P. P. Pronko, *Appl. Phys. Lett.* **67**, 3120 (1995).
155. T. Sato, S. Furuno, S. Iguchi and M. Hanabusa, *Jpn. J. Appl. Phys.* **26**, L1487 (1987).
156. S. S. Wagal, E. M. Juengerman and C. B. Collins, *Appl. Phys. Lett.* **53**, 187 (1988).
157. J. J. Cuomo, D. L. Pappas, J. Bruley, J. P. Doyle and K. L. Saenger, *J. Appl. Phys.* **70**, 1706 (1991).
158. S. R. Foltyn in *Pulsed Laser Deposition of Thin Films* edited by D. B. Chrisey and G. K. Hubler (Wiley, New York, 1994), pp 89.
159. C. L. Marquardt, R. T. Williams and D. J. Nagel, *Mater. Res. Soc. Symp. Proc.* **38**, 325 (1985).
160. T. Sato, S. Furuno, S. Iguchi and M. Hanabusa, *Appl. Phys. A* **45**, 355 (1988).
161. F. Davanloo, E. M. Juengerman, D. R. Jander, T. J. Lee and C. B. Collins, *J. Mater. Res.* **5**, 2398 (1990).
162. F. Davanloo, E. M. Juengerman, D. R. Jander, T. J. Lee and C. B. Collins, *J. Appl. Phys.* **67**, 2081(1990).

163. C. B. Collins, F. Davanloo, D. R. Jander, T. J. Lee, H. Park, and J. H. You, *J. Appl. Phys.* **69**, 7862 (1991).
164. C. B. Collins, F. Davanloo, T. J. Lee, J. H. You and H. Park, *Mater. Res. Soc. Symp. Proc.* **285**, 547 (1993).
165. C. B. Collins, F. Davanloo, T. J. Lee, H. Park and J. H. You, *J. Vac. Sci. Technol.* **B 11**, 1936 (1993).
166. J. A. Martin-Cago, L. Vazquez, P. Bernard, F. Comin and S. Ferrer, *Appl. Phys. Lett.* **57**, 1742 (1990).
167. J. A. Martin-Cago, L. Vazquez, P. Bernard, S. Ferrer and F. Comin, *Mater. Sci. Eng.* **B 11**, 337 (1992).
168. J. Diaz, J. A. Martin-Cago, S. Ferrer and F. Comin, *Diamond Relat. Mater.* **1**, 824 (1992).
169. L. Ganapathi, S. Giles and Rama Rao, *Appl. Phys. Lett.* **63**, 993 (1993).
170. M. A. Capano, F. Qian, R. K. Singh and N. T. McDevit, *Mater. Res. Soc. Symp. Proc.* **285**, 569 (1993).
171. F. Müller and K. Mann, *Diamond Relat. Mater.* **2**, 233 (1993).
172. Y. Huai, M. Chaker, J. N. Broughton, E. Gat, H. Pepin, T. Gu, X. Bian and M. Sutton, *Appl. Phys. Lett.* **65**, 830 (1994).
173. C. Germain, C. Girault, R. Gisbert, J. Aubreton and A. Catherinot, *Diamond Relat. Mater.* **3**, 598 (1994).
174. R. K. Dwivedi and R. K. Thareja, *Surf. and Coat. Technol.* **73**, 170 (1995).
175. R. K. Dwivedi and R. K. Thareja, *Phys. Rev.* **B 51**, 7160 (1995).
176. F. Vega, C. N. Afonso and J. Solis, *J. Appl. Phys.* **73**, 2472 (1993).
177. Z. Andreic, V. Henc-Bartolic and H. -J. Kunze, *Physica Scripta* **47**, 405 (1993).
178. A. H. El-Astal, S. Ikram, T. Morrow, W. G. Graham and D. G. Walmsley, *J. Appl. Phys.* **77**, 6572 (1995).
179. J. Gonzalo, F. Vega and C. N. Afonso, *J. Appl. Phys.* **77**, 6588 (1995).
180. P. Lecoeur, A. Gupta, P. R. Duncombe, G. Q. Gong and G. Xia, *J. Appl. Phys.* **80**, 513 (1996).
181. I. Apostol and R. Stopian, *Opt. Eng.* **35**, 1334 (1996).
182. T. F. Tseng, M. H. Yeh, K. S. Liu and I. N. Lin, *J. Appl. Phys.* **80**, 4984 (1996).
183. D. W. Koopman, *Phys. Fluids* **14**, 1707 (1971).



184. J. Brcka, E. W. Kreutz and A. Voss, *Elektrotechn. Cas.* **43**, 118 (1992).
185. C. T. Chang, M. Hashmi, and H. C. Pant, *Plasma Phys.* **19**, 1129 (1977).
186. R. J. von Gutfeld and R. W. Dreyfus, *Appl. Phys. Lett.* **54**, 1212 (1989).
187. J. M. Hendron, R. A. Al-Wazzan, C. Mahony, T. Morrow and W. G. Graham, *Appl. Surf. Sci.* **96**, 112 (1996).
188. R. W. Dreyfus, R. Kelly and R. E. Walkup, *Nucl. Instr. and Meth. B* **23**, 557 (1987).
189. M. A. Cappelli, P. H. Paul and R. K. Hanson, *Appl. Phys. Lett.* **56**, 1715 (1990).
190. C. E. Otis and R. W. Dreyfus, *Phys. Rev. Lett.* **67**, 2102 (1991).
191. T. Okada, Y. Nakayama, W. K. A. Kumuduni and M. Maeda, *Appl. Phys. Lett.* **61**, 2368 (1992).
192. R. P. van Ingen, *J. Appl. Phys.* **76**, 8055 (1994).
193. K. Tanaka, T. Miyajima, N. Shirai, Q. Zhuang and R. Nakata, *J. Appl. Phys.* **77**, 6581 (1995).
194. M. A. Capano, *J. Appl. Phys.* **78**, 4790 (1995).
195. D. B. Geohegan and D. N. Mashburn, *Appl. Phys. Lett.* **55**, 2345 (1989).
196. T. D. Kunz, R. F. Menefee, B. D. Krenek, L. G. Fredin and M. J. Berry, *High Temp. Sci.* **27**, 459 (1990).
197. M. Harnafi and B. Dubreuil, *J. Appl. Phys.* **69**, 7565 (1991).
198. R. M. Gilenbach and P. L. G. Ventzek, *Appl. Phys. Lett.* **58**, 1597 (1991).
199. T. Morrow, H. F. Sakeek, A. El Astal, W. G. Graham and D. G. Walmsley, *J. Supercond.* **7**, 823 (1994).
200. A. Gupta, B. Braren, K. G. Casey, B. W. Hussey and R. Kelly, *Appl. Phys. Lett.* **59**, 1302 (1991).
201. M. Ohkoshi, T. Yoshitake and K. Tsushima, *Appl. Phys. Lett.* **64**, 3340 (1994).
202. V. Kumar and R. K. Thareja, *Phys. Edu.* **9**, 271 (1992).
203. H. R. Griem, *Plasma Spectroscopy* (McGraw-Hill, New York, 1964).
204. G. Bekefi, *Principles of Laser Plasmas* (Wiley, New York, 1976).
205. A. Khare, V. Kumar and R. K. Thareja, *Z. Phys. D - Atoms, Molecules and Clusters* **6**, 67 (1987).
206. A. R. Striganov and N. S. Sventitskii, in *Tables of Spectral Lines of Neutral and Ionized Atoms* (Plenum, New York, 1968).

- W. L. Wiese, M. W. Smith and B. M. Glennon, *Atomic Transition Probabilities Vol I* (National Standard Reference Data System - NBS 4, US Government Printing Office, 1966).
207. P. J. Wolf, *J. Appl. Phys.* **76**, 1480 (1994).
  208. L. L. Danylewych and R. W. Nicholls, *Proc. R. Soc. Lond. A* **339**, 197 (1974).
  209. R. J. Spindler, *J. Quant. Spectrosc. Radiat. Transfer.* **5**, 165 (1965).
  210. F. F. Chen, in *Plasma Diagnostic Techniques* edited by R. H. Huddleston and S. L. Leonard (Academic, New York, 1965).
  211. F. G. Celii, D. White, Jr. and A. J. Purdes, *J. Appl. Phys.* **70**, 5636 (1991).
  212. Y. Rajakarunanayake, Y. Luo, B. T. Adkins, X. Dai and A. Compaan, in *Laser Ablation : Mechanisms and Applications-II* edited by J. C. Miller and D. B. Geohegan (AIP Press, New York, 1994) pp 577.
  213. X. J. Gu, *Appl. Phys. Lett.* **62**, 1568 (1993).
  214. R. O. Dillon, J. A. Woollam and V. Katkanant, *Phys. Rev.* **B 29**, 3482 (1984).
  215. R. J. Nemanich, J. T. Glass, G. Lucovsky and R. E. Shroder, *J. Vac. Sci. Technol.* **A 6**, 1783 (1988).
  216. D. J. Vitkavage, R. A. Rudder, G. G. Fountain and R. J. Markunas, *J. Vac. Sci. Technol.* **A 6**, 1812 (1988).
  217. V. A. Yakovlev, G. Mattei, A. Lembo, F. Fuso, E. Armino, M. Allegrini, F. Laccabue and B. E. Watts, *J. Appl. Phys.* **78**, 6321 (1995).
  218. P. J. Wolf, T. M. Christensen, N. G. Coit and R. W. Swinford, *J. Vac. Sci. Technol.* **A 11**, 2725 (1993).
  219. F. Qian, V. Nagabushnam and R. K. Singh, *Appl. Phys. Lett.* **63**, 317 (1993).
  220. M. A. Capano, S. D. Walck, P. T. Murray, D. Dempsey and J. T. Grant, *Appl. Phys. Lett.* **64**, 3413 (1994).
  221. S. C. Sharma, M. Green, R. C. Hyer, C. A. Dark, T. D. Black, A. R. Chourasia, D. R. Chopra and K. K. Mishra, *J. Mater. Res.* **5**, 2424 (1990).
  222. E. van de Reit, J. C. S. Kools and J. Dieleman, *J. Appl. Phys.* **73**, 8290 (1993).
  223. J. Seth, R. Padiyath, D. H. Rasmussen and S. V. Babu, *Appl. Phys. Lett.* **63**, 473 (1993).
  224. S. P. McGinnis, M. A. Kelly, S. B. Hagström and R. L. Alvis, *J. Appl. Phys.* **79**, 170 (1996).

225. B. E. Williams, H. S. Kong and J. T. Glass, *J. Mater. Res.* **5**, 801 (1990).
226. J. Singh, M. Vellaikal and J. Narayan, *J. Appl. Phys.* **73**, 4351 (1993).
227. M. Yoshimoto, T. Arakane, T. Asakawa, K. Horiguchi, K. Hirai and H. Koinuma, *Jp. J. Appl. Phys.* **32**, L1081 (1993).
228. M. Balooch, D. R. Olander and R. E. Russo, *Appl. Phys. Lett.* **55**, 197 (1989).
229. P. Kovarik, E. B. D. Bourdon and R. H. Prince, *Phys. Rev. B* **48**, 12123 (1993).
230. C. S. Ma, S. K. Hau, K. H. Wong, P. W. Chan and C. L. Choy, *Appl. Phys. Lett.* **69**, 2030 (1996).
231. H. -U. Krebs, S. Fahler and O. Bremert, *Appl. Surf. Sci.* **86**, 86 (1995).
232. J. C. S. Kools, C. J. C. M. Nillesen, S. H. Brongersma, E. van de Riet and J. Dieleman, *J. Vac. Sci. Technol.* **A10**, 1809 (1992).
233. H. J. Wu, T. C. Chou, A. Mishra, D. R. Anderson, J. K. Lampert and S. C. Gujrathi, *Thin Solid Films* **191**, 55 (1990).
234. X. D. Wu, X. X. Xi, Q. Li, A. Inam, B. Dutta, L. DiDomenico, C. Weiss, J. A. Martinez, B. J. Wilkens, S. A. Schwarz, J. B. Barner, C. C. Chang, L. Nazar and T. Venkatesan, *Appl. Phys. Lett.* **56**, 400 (1990).
235. R. K. Singh, N. Biunno and J. Narayan, *Appl. Phys. Lett.* **53**, 1013 (1988).
236. C. B. Collins, F. Davanloo, T. J. Lee, D. R. Jander, J. H. You, H. Park and J. C. Pivin, *J. Appl. Phys.* **71**, 3260 (1992).
237. J. Levoska and S. Leppavuori, *Appl. Surf. Sci.* **86**, 180 (1995).
238. P. F. Kane and G. B. Larrabee, *Characterization of Semiconductor Materials*, (McGraw-Hill, New York, 1970).
239. K. Dittrich and R. Wennrich, *Prog. Analyt. Atom. Spectrosc.* **7**, 139 (1984).
240. Y. V. Afanas'ev and O. N. Krokhin, *Sov. Phys. JETP* **25**, 639 (1967).
241. R. A. Olstad and D. R. Olander, *J. Appl. Phys.* **46**, 1499 (1975).
242. C. L. Chan and J. Mazumder, *J. Appl. Phys.* **62**, 4579 (1987).
243. R. F. Wood and G. E. Giles, *Phys. Rev. B* **23**, 2923 (1981).
244. C. R. Phipps, Jr., T. P. Turner, R. F. Harrison, G. W. York, W. Z. Osborne, G. K. Anderson, X. F. Corlis, L. C. Haynes, H. S. Steele, K. C. Spicochi and T. R. King, *J. Appl. Phys.* **64**, 1083 (1988).
245. M. Aden, E. Beyer and G. Herziger, *J. Phys. D: Appl. Phys.* **23**, 655 (1990).

246. M. Aden, E. Beyer, G. Herziger and H. Kunze, J. Phys. D: Appl. Phys. **25**, 57 (1992).
247. J. C. S. Kools, T. S. Baller, S. T. De Zwart and J. Dieleman, J. Appl. Phys. **71**, 4547 (1992).
248. J. C. S. Kools, J. Appl. Phys. **74**, 6401 (1993).
249. R. Kelly, J. Chem. Phys. **92**, 5047 (1990).
250. R. Kelly, A. Miotello, B. Braren, A. Gupta and K. Casey, Nucl. Instrum. Methods Phys. Res. **B 65**, 187 (1992).
251. K. L. Saenger, J. Appl. Phys. **70**, 5629 (1991).
252. Ya. B. Zel'dovich and Yu. P. Raizer, *Physics of Shock Waves and High Temperature Hydrodynamics Phenomenon* Vol 1 (Academic, New York, 1966).
253. D. B. Geohegan, Appl. Phys. Lett. **60**, 2732 (1992).
254. P. E. Dyer, A. Issa and P. H. Key, Appl. Phys. Lett. **57**, 186 (1990).
255. W. K. A. Kumuduni, Y. Nakayama, Y. Nakata, T. Okada and M. Maeda, Jpn. J. Appl. Phys. **32**, L271 (1993).
256. A. F. Haught and D. H. Polk, Phys. Fluids **9**, 2047 (1966).
257. J. Dawson, P. Kaw and B. Green, Phys. Fluids **12**, 875 (1969).
258. N. G. Basov, V. A. Boiko, V. A. Dement'ev, O. N. Krokhin and G. V. Sklizkov, Sov. Phys. JETP **24**, 659 (1967).
259. W. J. Fader, Phys. Fluids **11**, 2200 (1968).
260. K. R. Chen, J. N. Leboeuf, R. F. Wood, D. B. Geohegan, J. M. Donato, C. L. Liu and A. A. Puretzky, Phys. Rev. Lett. **75**, 4706 (1995).
261. A. Caruso and R. Gratton, Plasma Phys. **10**, 867 (1968).
262. D. B. Geohegan, in *Laser Ablation of Electronic Materials : Basic Mechanisms and Applications* edited by E. Fogarassy and S. Lazare (North Holland, Amsterdam, 1992) pp 73.
263. P. E. Dyer and J. Sidhu, J. Appl. Phys. **64**, 4657 (1988).
264. R. W. Dreyfus, R. Kelly and R. E. Walkup, Appl. Phys. Lett. **49**, 1478 (1986).
265. R. Viswanathan and I. Hussla, J. Opt. Soc. Am. **B 3**, 796 (1986).
266. M. Berti, L. F. Dona dalle Rose, A. V. Drigo, C. Cohen, J. Siejka, G. G. Bentini and E. Jannitti, Phys. Rev. **B 34**, 2346 (1986).
267. J. T. C. Yeh, J. Vac. Sci. Technol. **A4**, 653 (1986).

269. Y. Iida, Appl. Spectrosc. **43**, 229 (1989).
270. B. H. Ripin, C. K. Manka, T. A. Payser, E. A. Mclean, J. A. Stamper, A. N. Mostovych, J. Grun, K. Kearney, J. R. Crawford and J. D. Huba, Laser and Part. Beams **8**, 183 (1990).
271. R. Kelly, B. Baren and K. G. Casey, Appl. Phys. **B 53**, 160 (1991).
272. P. E. Dyer, S. R. Farrar, A. Issa and P. H. Key, in *Laser Ablation of Electronic Materials : Basic Mechanisms and Applications* edited by E. Fogarassy and S. Lazare (North Holland, Amsterdam, 1992) pp 101.
273. P. T. Rumsby and J. W. M. Paul, Plasma Phys. **16**, 247 (1974).
274. K. Kagawa, M. Ohtani, S. Yokoi, and S. Nakajima, Spectrochim. Acta **39B**, 525 (1984).
275. R. Fabbro, E. Fabre, F. Amiranoff, C. Garban-Labaune, J. Virmont, M. Weinfeld, and C. E. Max, Phys. Rev. A **26**, 2289 (1982).
276. H. Ajie, M. M. Alvarez, S. J. Anz, R. D. Beck, F. Diederich, K. Fostiropoulos, D. R. Huffman, W. Krätschmer, Y. Rubin, K. Schriver, D. Sensharma and R. L. Whetten, J. Phys. Chem. **94**, 8630 (1990).
277. D. S. Knight and W. B. White, J. Mat. Res. **4**, 385 (1989).
278. F. Tuinstra and J. L. Koenig, J. Chem. Phys. **53**, 1126 (1970).
279. M. A. Tamor and C. H. Wu, J. Appl. Phys. **67**, 1007 (1990).

125663

## Date Slip

This book is to be returned on the  
date last stamped. **125663**

125663

[illegible]

**A125663**

1950年10月1日